

CERIUM-ZIRCONIUM OXIDE NANOCATALYSTS AS FREE RADICAL SCAVENGERS
FOR BIOMEDICAL APPLICATIONS

By

YI-YANG TSAI

A DISSERTATION PRESENTED TO THE GRADUATE SCHOOL
OF THE UNIVERSITY OF FLORIDA IN PARTIAL FULFILLMENT
OF THE REQUIREMENTS FOR THE DEGREE OF
DOCTOR OF PHILOSOPHY

UNIVERSITY OF FLORIDA

2008

© 2008 Yi-Yang Tsai

To my parents, fiancée, and advisors who had been highly encouraging and supportive

ACKNOWLEDGMENTS

There are many teachers and friends to thank for. Without your guidance, inspiration, and consideration, this work would never be accomplished.

First of all, I would like to thank Dr. Wolfgang Sigmund for his inputs and scientific advises to this work. On top of the advisory guidance, he also delivered his enthusiasm, generosity, and philosophy to students. Without his mentoring and broad research interests, this project would have been plain and lack of innovation. I would also like to thank my committee members, Drs. Holloway, Moudgil, Batich, and Atkinson for their constructive comments. They have excellent reputation and are highly knowledgeable in academia. They are prominent scholars and are great examples in my future career development. I would like to dedicate this work to the memory of Dr. Ioannis Constantinidis, who was an advisor, cheerleader, and sincere friend of mine.

I would like to thank current and previous colleagues in Sigmund Group. Without them I would never learn my broad interests and insights in this emerging research project, especially Drs. Georgios Pyrgiotakis and Amit Daga for setting up great examples for young group members. I would like to thank those people who have helped me in this project. Many assistances from them start from my accidental requests, but they had big heart assisting me into the situation. Jose Oca-Cossio, Kelly Siebein, and Gill Brubaker are especially acknowledged in this project.

Finally I would like to thank my parents for being supportive through my study in the United States. I also like to thank my fiancée, Ju-Hsuan Cheng PharmD. She accompanied me through the tough time, and has created wonderful time as well as memories in my life.

TABLE OF CONTENTS

	<u>page</u>
ACKNOWLEDGMENTS	4
LIST OF TABLES	8
LIST OF FIGURES	9
LIST OF ABBREVIATIONS.....	11
CHAPTER	
1 INTRODUCTION	15
1.1 Motivation.....	17
1.2 Objectives	18
1.3 Specific Aims and Expected Outcomes.....	19
2 BACKGROUND	22
2.1 Free Radicals in Biology and Medicine.....	22
2.1.1 Free Radical Theory of Aging.....	22
2.1.2 Modern Free Radical Theory in Biology.....	24
2.2 Antioxidant Defense in Biology and Medicine	26
2.2.1 Antioxidant Defense System	26
2.2.2 Alternative Antioxidant Defense Other Than Direct Free Radical Scavenging.....	28
2.3 CeO_2 in Catalysis, Biology, and Medicine	28
2.3.1 CeO_2 as Catalysts	29
2.3.2 CeO_2 Nanoparticles in Biomedical Applications	29
2.3.3 Free Radicals in CeO_2	31
2.3.4 Hypothesis of CeO_2 Nanoparticles in Free Radical Scavenging.....	32
2.3.5 Promote Catalytic Activity by Doping Zirconium into CeO_2	33
2.3.6 Introduction of $Ce_xZr_{1-x}O_2$	35
3 TEST HYPOTHESIS WITH CELL CULTURES	39
3.1 Methodology.....	39
3.2 Results and Discussion	44
3.3 Summary.....	54
4 SYNTHESIS OF CERIUM-ZIRCONIUM OXIDE NANOPARTICLES.....	55
4.1 Nanoparticle Synthesis	56
4.1.1 Reverse Micelle Synthesis.....	56
4.1.2 Experimental Methods.....	57
4.2 Nanoparticle Stabilization	59

4.2.1	Stabilization Using Buffer	59
4.3	Particle Size Analysis	60
4.3.1	Dynamic Light Scattering Technique	60
4.3.2	Agglomerate Size Distribution	60
4.4	Chemical Analysis	62
4.4.1	Inductively Coupled Plasma Spectroscopy	62
4.4.2	Compositions of Final Products	63
4.5	Summary	63
5	STRUCTURAL PROPERTIES AND NONSTOICHIOMETRIC BEHAVIOR OF CERIUM-ZIRCONIUM Oxide Nanoparticles	65
5.1	Characterization Techniques and Experimental Methods	65
5.1.1	Structural Characterization Using TEM	65
5.1.2	Structural Characterization Using XRD	66
5.1.3	Structural Characterization Using Raman	67
5.2	TEM Results and Discussion	68
5.3	XRD Results and Discussion	76
5.4	Raman Results and Discussion	78
5.5	Summary of TEM, XRD, Raman Results	82
5.5.1	Crystalline $Ce_xZr_{1-x}O_2$ Nanoparticles with Homogeneous Particle Size	82
5.5.2	Phase Transition Detected by XRD and Raman Spectroscopy	82
6	FREE RADICAL SCAVENGING BY CERIUM-ZIRCONIUM OXIDE NANOPARTICLES	84
6.1	Prospective Scavenging Activities in $Ce_xZr_{1-x}O_2$ Nanoparticles	84
6.2	Activities against Hydrogen Peroxide	86
6.2.1	Experimental Methods	86
6.2.2	Results and Discussion	88
6.3	Activities against Superoxide Radicals	93
6.3.1	Experimental Methods	94
6.3.2	Results and Discussion	98
6.4	Electron Conduction in Catalysis	115
6.4.1	Experimental Methods	116
6.4.2	Results and Discussion	118
6.5	Summary	118
7	IMPLICATIONS	121
7.1	Distinct Antioxidant Defense Pathway	121
7.2	Implications in Catalysis	124
7.2.1	Alternative Technique to Inspect ionic Conductivity at Room Temperature	124
7.2.2	Alternative Technique to Inspect Localized Electron Conductivity	125
8	CONCLUSIONS	127

APPENDIX

A GLOSSARY	129
LIST OF REFERENCES	132
BIOGRAPHICAL SKETCH	140

LIST OF TABLES

<u>Table</u>	<u>page</u>
2-1 Genetic changes and the responded free radical scavengers that affect oxidative damage in living systems.	27
2-2 Classification of the phases in the CeO_2 - ZrO_2 binary system.....	36
3-1 Intracellular amount of CeO_2 in β TC-tet cells following 48 hrs of incubation with media containing CeO_2 nanoparticles.	49
4-1 Chemicals and the amounts used to prepare $Ce_xZr_{1-x}O_2$ nanoparticles in reverse micelle synthesis.	58
4-1 Synthesis procedures.....	58
4-2 Mean agglomeration size (M_n), D_{50} , and D_{95} of $Ce_xZr_{1-x}O_2$ suspensions obtained using NanoTrac.....	61
4-3 Chemical compositions of final products determined.	63
5-1 Particle sizes of $Ce_xZr_{1-x}O_2$ nanoparticles averaged from 50 arbitrary selected particles in TEM micrographs.	76
5-2 Crystal structures and their sub-phases in $Ce_xZr_{1-x}O_2$, and the classification using Raman spectroscopy.	79
6-1 Concentrations for enzyme SOD and $Ce_xZr_{1-x}O_2$ nanoparticles to achieve 50% of inhibition rate in activity test.	110
6-2 Reaction rate constants of $Ce_xZr_{1-x}O_2$ nanoparticles against superoxide radicals.	111

LIST OF FIGURES

<u>Figure</u>	<u>page</u>
2-1 Metabolism in a mitochondrion.....	26
2-2 Hypothetic mechanism of free radical scavenging in the vicinity of CeO_2 surface.	33
2-3 Schematic diagrams showing cubic fluorite (left) and pyrochlore (right) structures for CeO_2/ZrO_2 and $Ce_xZr_{1-x}O_2$, respectively.....	34
2-4 Phase diagram of the CeO_2 - ZrO_2 binary system.....	36
2-5 Phase transition of CeO_2 - ZrO_2 binary system..	37
2-6 XRD and Raman spectra of $(1-x)CeO_2-xZrO_2$	38
3-1 TEM micrographs of CeO_2 nanoparticles.....	45
3-2 XRD pattern of CeO_2 nanoparticles.....	46
3-3 Chemical compositions of the tri-sodium citrate buffer.	47
3-4 Zeta potentials of CeO_2 suspensions as a function of pH.	48
3-5 TEM micrographs of CeO_2 nanoparticles in β TC-tet cells.	50
3-6 Free radical concentration in β TC-tet cells.....	52
3-7 The amount of insulin secreted by non-labeled and CeO_2 labeled β TC-tet cells.	53
4-2 Optical images of CeO_2 nanoparticles dispersed in DI water (left), and in sodium citrate buffer solution solution (right).....	59
4-3 Agglomerate size distribution in $Ce_xZr_{1-x}O_2$ suspensions at pH 7.4.....	61
5-1 TEM micrographs of CeO_2 nanoparticles.....	69
5- 2 TEM micrographs of $Ce_{0.8}Zr_{0.2}O_2$ nanoparticles.	70
5-3 TEM micrographs of $Ce_{0.7}Zr_{0.3}O_2$ nanoparticles.	71
5-4 TEM micrographs of $Ce_{0.6}Zr_{0.4}O_2$ nanoparticles.	72
5-5 TEM micrographs of $Ce_{0.4}Zr_{0.6}O_2$ nanoparticles.	73
5-6 TEM micrographs of $Ce_{0.2}Zr_{0.8}O_2$ nanoparticles.	74
5-7 TEM micrographs of ZrO_2 nanoparticles.	75

5-8	XRD spectra of a series of $Ce_xZr_{1-x}O_2$ nanoparticles.....	77
5-9	Raman spectra of $Ce_xZr_{1-x}O_2$ nanoparticles.....	81
6-1	Hypothesized scheme of free radical scavenging by $Ce_xZr_{1-x}O_2$ nanoparticles.....	85
6-2	OSC of $Ce_xZr_{1-x}O_2$ measured a pulse chromatographic system at 400 °C.....	86
6-3	Detection scheme used to determine the peroxide concentration in activity tests.....	87
6-4	A) shows the peroxide concentration in the presence of 7 nm commercial CeO_2 and synthesized $Ce_xZr_{1-x}O_2$ nanoparticles over time. B) shows the natural logarithmic values of the peroxide concentration divided by initial peroxide concentration.	89
6-5	The effective scavenging efficiency K of $Ce_xZr_{1-x}O_2$ nanoparticles vs. OSC and the amount of superoxide radicals.	91
6-6	Superoxide radicals produced by hypoxanthine and xanthine oxidase.	94
6-7	Principle of WST-1 assay to detect superoxide radicals.....	95
6-8	Experimental arrangement of stock solution concentrations, total concentrations, and experimental procedures.	97
6-9	The setup of stock solutions and their concentrations in a 96-wells microplate.	98
6-10	The results of activity test obtained using UV-Vis.....	101
6-11	The results of activity tests obtained using UV-Vis.	102
6-12	The results of activity tests measured by microplate reader.....	103
6-13	The results of activity tests measured by microplate reader.....	105
6-14	The results of activity tests measured by microplate reader.....	107
6-15	Inhibition curves of enzyme SOD with different incubation time.....	110
6-16	Ce^{3+} contents and OSC in $Ce_xZr_{1-x}O_2$ nanoparticles.....	113
6-17	Principle of the biochemistry based assay to inspect the capability for $Ce_xZr_{1-x}O_2$ nanoparticles to conduct electrons in catalysis.	115
6-18	Experimental arrangements of stock solution concentrations and experimental procedures to inspect electron conduction on $Ce_xZr_{1-x}O_2$ nanoparticles.....	117
6-19	Redox states of cytochrome c detected using UV-Vis.....	117
7-1	Redox states of cytochrome c in the presence or absence of superoxide radicals.....	123

LIST OF ABBREVIATIONS

AD	Alzheimer's diseases
CAT	Catalase
CeO_2	Cerium oxide, cerium dioxide, or sometimes listed as ceria
$Ce_xZr_{1-x}O_2$	Zirconium-doped CeO_2 solid solutions
COX	Cytochrome c Oxidase
DLS	Dynamic light scattering
DMEM	Dulbecco's Modified Eagle's Medium
DNA	Deoxyribonucleic acid
DCF	Reactive oxygen species probe, 2',7'-dichlorofluorescein diacetate.
EDS	Energy dispersive spectrum
ELISA	Enzyme-Linked Immuno Sorbent Assay
ER	Endoplasmic reticulum
GSH	Glutathione
GPx	Glutathione peroxidase
HD	Huntington diseases
HO	Heme oxygenase
HQ	Hydroquinone
HRP	Horse radish peroxidase
HX	Hypoxanthine
ICP	Inductively coupled plasma
IEP	Isoelectric point
MAIC	Major Analytical Instrumentation Center at University of Florida
MCP	Monocyte chemoattractant protein
NADH	Nicotinamide adenine dinucleotide

NADP	Nicotinamide adenine dinucleotide phosphate
OSC:	Oxygen storage capacity
PBS	Phosphate buffered saline
PD	Parkinson's disease
PERC	Particle Engineering Research Center at University of Florida
PHGPx	Phospholipid hydroperoxide glutathione peroxidase
ROS	Reactive oxygen species
SAD	Selective area diffraction
SOD	Superoxide dismutase
TEM	Transmission electron microscopy
XO	Xanthine oxidase
XRD	X-ray diffraction

Abstract of Dissertation Presented to the Graduate School
of the University of Florida in Partial Fulfillment of the
Requirements for the Degree of Doctor of Philosophy

CERIUM-ZIRCONIUM OXIDE NANOCATALYSTS AS FREE RADICAL SCAVENGERS
FOR BIOMEDICAL APPLICATIONS

By

Yi-Yang Tsai

August 2008

Chair: Wolfgang M. Sigmund
Major: Materials Science and Engineering

Administering CeO_2 nanoparticles into cell cultures was found to improve cell culture's viability both *in vitro* and *in vivo*. In this dissertation, an *in vitro* study conducted in our laboratory has observed the reduction of endogenous free radical concentration in CeO_2 treated cell cultures. Furthermore, it is found that CeO_2 nanoparticles scavenge free radicals through catalysis. Based on the findings, a series of CeO_2 -based nanocrystallites of greater catalytic activities was developed, aiming to achieve the same therapeutic efficacy to cell cultures with lower nanoparticle doses.

In this dissertation, zirconium-doped CeO_2 ($Ce_xZr_{1-x}O_2$) nanoparticles were synthesized and characterized. Their free radical scavenging activities were tested against harmful endogenous oxygen species, including hydrogen peroxide and superoxide radicals. It is found that the scavenging activity of $Ce_xZr_{1-x}O_2$ nanoparticles was promoted up to four times when scavenging hydrogen peroxide. The scavenging activity of $Ce_xZr_{1-x}O_2$ nanoparticles was promoted up to nine times when scavenging superoxide radicals. Importantly, their free radical scavenging activities to hydrogen peroxide correlate to the reported oxygen vacancy concentrations in the same materials. Their free radical scavenging activities to superoxide

radicals correlate to the reported reducibility in the same materials. The results suggest that oxygen vacancies, lattice oxygen, electrons, and holes are involved in free radical scavenging.

In addition, it is found that $Ce_xZr_{1-x}O_2$ nanoparticles regulate antioxidant protein's redox states upon catalysis. This might be a distinct antioxidant defense pathway that reactivates antioxidant protein's function, and to explain the superior protection of CeO_2 nanoparticles.

CHAPTER 1 INTRODUCTION

In the last decade, many disorders and diseases in mammals were found to correlate with the damages caused by endogenous oxidative stress [1,2]. The oxidative stress in living system is a result of accumulating free radicals, where lipids, proteins, DNA, and other molecules receive or donate mobile electrons from free radicals [1,3]. The long-term accumulative damages caused by free radicals finally cause mutation of cells or apoptosis (programmed cell death) [1,4]. The damages further contribute to tissue injury or dysfunction, and finally progress to human disorders. For example, (1) neurodegenerative diseases including Parkinson's disease (PD), Alzheimer's disease (AD), Huntington's disease (Juvenile HD) [1,5,6,7]; (2) certain cardiovascular diseases including strokes, heart attacks, ischemia, and atherosclerosis [1,8,9]; (3) genetic and metabolic diseases including Down's syndrome and diabetes [1,10,11]; (4) cancers including liver, prostate, lung, breast, and many other cancers [1,12]; (5) symptoms of aging including osteoporosis [1], were found to be the result of overproduced endogenous free radicals. Meanwhile, the excess amounts of free radicals were also a consequence of some human disorders, such as inflammatory disorders [1,13], allergies [1,14], and infectious diseases including pneumonia [1,15] and HIV [1]. Therefore, the research on the role of free radicals in pathophysiologic processes and the potential therapies to oxidative stress related disorders are drawing more and more attention over time.

Mammalian cells fight against detrimental free radicals through antioxidant defense systems by scavenging the redundant oxidative stress. Scientists have demonstrated that administering effective means of free radical scavengers protects biological systems from oxidative damage of lipids, proteins, DNA, and other molecules [1,16,17]. The protection in cell cultures can prevent apoptosis, mutation, and enhance the viability of cell cultures [1,18]. In

living animals, the therapeutic efficacy has been demonstrated to inhibit the symptoms of AD, PD [1,19], diabetes [1], cancers [1,20], other diseases, and even prolong laboratory animal's lifespan [21,22,23,24].

The antioxidants or free radical scavengers that carry out antioxidant defenses in mammals are listed in the following [1].

- Enzymes that catalytically remove free radicals, such as superoxide dismutase (SOD), glutathione peroxidase (GPx), catalase (CAT), and other peroxidase enzymes.
- Enzymes that catalytically synthesize compounds that can remove free radicals, such as heme oxygenase (HO).
- Compounds that physically quench free radicals, such as carotenoids.
- Compounds that act as sacrificial agents to protect more valuable biomolecules, such as cytochrome c (cyt c), ascorbic acid (vitamin C), α -tocopherol (vitamin E), glutathione (GSH).
- Enzymes that catalytically recover the sacrificed compounds back into the original state, such as cytochrome c oxidase (COX).
- Proteins that protect molecules against damage caused by other mechanisms, such as chaperones.
- Compounds, proteins, or enzymes that regulate redox states of mitochondria, such as GSH and protein *bcl-2*.

The free radical scavenging cooperates with complicated chemical and catalytic reactions. Usually the scavenging processes carried out through redox reactions of a compound/agent, and the particular compound/agent is activated by the second or more agents. The sequent reactions cascade reactive free radicals and are terminated with the formation of stable species, such as oxygen, water, nitric oxides, and carbon dioxide. However, the scavenging mechanisms *in vivo* are even more complicated, and many of them remain mystical even after years of research in this field.

However, the protection from free radical scavengers is not 100% effective. The protection from free radical scavengers is restricted by their turnover numbers, the uptake rates, and their distributions *in vivo*. In general, high doses, routine administration of antioxidants are inevitable to achieve effective means to living animals. The demands for effective free radical scavengers are soaring since more and more human diseases, including aging, were found to connect to oxidative stress. A broad variety of free radical scavengers have been explored, synthesized, and tested in order to achieve the therapeutic intervention to living systems. More effective, lipophilic, and even organelle-targeting antioxidants have been developed in order to satisfy the needs of life sciences.

Most free radical scavengers used for therapy are organic compounds or chelations with transition metal ions. However, a new platform has been demonstrated to perform similar antioxidant protection to biological systems. CeO_2 nanoparticles were accidentally found to improve brain cell culture's viability and organism longevity up to six fold [25,26]. Although how these ceramic nanoparticles improve cell's viability remains controversial, we found that CeO_2 nanoparticles reduce endogenous free radical concentrations in cells and may protect cells as free radical scavengers [27]. Indeed, recent studies, including works published by our group [27], have demonstrated that CeO_2 nanoparticles are able to scavenge hydroxyl radicals [28], superoxide radicals [29], and peroxides in the absence of cell cultures.

1.1 Motivation

The motivation of this dissertation was originally to improve the transplanted islet's viability, in order to increase the off-insulin time when using transplanted islets to treat patients with type 1 diabetes. Type 1 diabetes is an autoimmune disorder, in which the body's own immune system attacks the beta cells in the pancreas, the damage causes islets to shut down insulin production. This fatal disorder causes blindness, kidney and heart failure, limb

amputation, and other diseases associated complications [30]. Recently, pancreatic islet cell transplantation has been proposed as an ideal treatment to type 1 diabetes; however, damages caused by mechanical trauma and anti-rejection drugs dramatically decrease the amounts of preserved islets [31,32,33]. Thus, one of the major challenges is to increase the preserved islets mass during isolation and post transplantation [34,35]. To improve the preservation, using CeO_2 nanoparticles to improve transplanted islet's viability was proposed.

The motivations of this dissertation are as follow.

- To improve preservation of transplanted islets using CeO_2 nanoparticles.
- To identify the mechanism of beneficial efficacy that carried out by CeO_2 nanoparticles.
- To develop a new platform according to the concept in materials science. Aim to achieve the same therapeutic efficacy to biological systems by lowering the applied nanoparticle dosages.

1.2 Objectives

CeO_2 is an excellent catalyst that carries out non-selective catalytic reactions through exchange of electrons, holes, lattice oxygen, and oxygen ions. In many discussions related to its surface chemistry, it has been demonstrated that ROS, such as superoxide, peroxide, singlet oxygen ions, act as intermediates and are involved in the catalytic reactions [36]. Interestingly, viability enhancement of cell cultures has been broadly achieved by using ROS scavengers. Therefore, the key hypothesis in this dissertation relies on the fact that CeO_2 is a remarkable catalyst and it may act as ROS scavengers in the viability enhancement. With the hypothesis aforementioned, there are several objectives in this dissertation.

- Test free radical concentrations in CeO_2 nanoparticles treated cells, and the relationship between free radical concentrations and cellular viability.
- Understand free radical chemistry in between biology/nanoparticles interfaces.
- Identify distinct antioxidant defenses performed by CeO_2 nanoparticles beyond current knowledge.

- Promote the beneficial efficacy of CeO_2 nanoparticles.
- Achieve the same benefits to biological systems with lower dosages of CeO_2 -based nanoparticles.

1.3 Specific Aims and Expected Outcomes

To achieve the objectives, it is necessary to develop a series of nanoparticles that exhibits greater ROS scavenging activities. According to the aforementioned hypothesis, ROS scavenging properties of CeO_2 nanoparticles are a consequence of catalysis and the properties could be promoted by increasing oxygen vacancies in the materials. Here, it is proposed to dope zirconium into CeO_2 nanoparticles in order to promoting CeO_2 nanoparticle's ROS scavenging activities. There are two reasons choosing zirconium as dopants. First, the oxidation form of zirconium, zirconia (ZrO_2), is a very biocompatible material, and it has been broadly used as biomaterials, such as dental materials. Second, zirconium doped CeO_2 ($Ce_xZr_{1-x}O_2$) materials have been used to improve the catalytic activity carried out by CeO_2 . With zirconium ions substituting cerium ions in the lattice, it is found that $Ce_xZr_{1-x}O_2$ has four times more oxygen vacancies than CeO_2 . The catalytic activities of $Ce_xZr_{1-x}O_2$ correlated with the amount of oxygen vacancies, so it can be expected to improve up to four times compared to CeO_2 .

The activities of these $Ce_xZr_{1-x}O_2$ nanoparticles will be tested in response to crucial free radicals in biological systems, and their activities will be compared with the enzymes that specifically scavenge these popular free radicals. The free radical scavenging activity will be evaluated using biochemical assays that have long been used to test enzyme activities.

There are several specific aims in this dissertation.

- Synthesize CeO_2 nanoparticles, and test their beneficial efficacy to β TC-tet cells, including free radical concentrations in the treated cultures.
- Synthesize $Ce_xZr_{1-x}O_2$ nanoparticles with monodispersed particle diameters, where $x = 0-1.0$.

- Characterize $Ce_xZr_{1-x}O_2$ nanoparticles' structures, and demonstrate the zirconium dopants incorporated in the CeO_2 lattice, and form a solid solution.
- Evaluate the scavenging activities of the synthesized nanoparticles in response to free radicals that are influential in living systems, i.e. superoxide radicals ($O_2^{\bullet-}$) and peroxide (O_2^{2-}), and compare their activities in respect to particular enzymes that scavenge superoxide radicals and peroxide, i.e. enzyme SOD and CAT.

To attain the objectives of this dissertation, $Ce_xZr_{1-x}O_2$ nanoparticles will be prepared using reverse micelle synthesis. The structures of the synthesized nanoparticles will be investigated using transmission electron microscopy (TEM), x-ray diffraction (XRD), and Raman spectroscopy. The scavenging activities of $Ce_xZr_{1-x}O_2$ nanoparticles will be evaluated with commercial assays based on biochemical reactions. The following results are expected in this dissertation.

- Free radical concentrations inhibited in the CeO_2 nanoparticle treated cultures.
- $Ce_xZr_{1-x}O_2$ nanoparticles with narrow particle size distribution and with diameters of 3-7 nm, whereas $x = 0, 0.2, 0.4, 0.6, 0.7, 0.8, 1.0$. The synthesized $Ce_xZr_{1-x}O_2$ nanoparticles are solid solutions with defined structures.
- $Ce_xZr_{1-x}O_2$ nanoparticles exhibit greater free radical scavenging activity in response to superoxide radicals and peroxide. Their scavenging activities vary with different amounts of zirconium doping.
- The free radical scavenging activities of $Ce_xZr_{1-x}O_2$ nanoparticles correlate to the concentration of oxygen vacancy in their lattice. Free radical scavenging activities of $Ce_xZr_{1-x}O_2$ nanoparticles could be improved up to four times in $Ce_xZr_{1-x}O_2$ nanoparticles with 20-40 % zirconium dopants.

In general, this dissertation covers the synthesis, characterization of nanoparticles, and investigations to the free radical chemistry in between bio/nano interfaces. The focus of this dissertation is especially on the investigations of free radical chemistry in between bio/nano interfaces, which is accomplished by testing the free radical scavenging activity of vacancy engineered nanoparticles. After all, the contribution in this dissertation gives a comprehensive understanding to, first, the therapeutic efficacy of CeO_2 nanoparticles in biological systems;

second, the mechanism of free radical scavenging by CeO_2 -based nanoparticles. Based on the advancement in knowledge, this work may help preparing more effective free radical scavenging nanoparticles for biomedical applications. In summary, we are aiming to achieve the same therapeutic efficacy to biological systems by treating lower nanoparticle dosages.

CHAPTER 2 BACKGROUND

In this chapter, the background of free radicals in biology and medicine will be introduced. After it, the antioxidant defense systems and alternative defense pathways that are used to protect biological systems from free radical's attack will be introduced. Finally, current research based on CeO_2 nanoparticle's therapeutic efficacy will be listed and described in detail. Most importantly, the hypothetical mechanism to describe the benefits that CeO_2 nanoparticles brought to biological systems as well as a model that can be used to improve CeO_2 nanoparticle's activity are also covered in this chapter.

2.1 Free Radicals in Biology and Medicine

2.1.1 Free Radical Theory of Aging

Free radicals are species capable of independent existence that contain one or more unpaired electrons. Because of the unpaired electrons, free radicals tend to be reactive and easily undergo chemistry with other molecules. There are a broad variety of free radical species in living systems. This occurs because electrons generated in the metabolic chain react with other molecules (such as oxygen, proteins, lipids, and DNA, RNA), forming free radicals. The metabolic chain in mammalian cells for energy generation mostly occurs in mitochondria. By consuming glucose and oxygen, mitochondria transfer nutrition into energy and yield as byproducts oxygen radicals (shown in Figure 2-1). In mitochondria, electrons leaked out as failures occur in the electron transportation chain (shown in Figure 2-1 (a)). The leaked electrons then react with oxygen or other species, forming oxygen radicals and other free radicals. Therefore, more than 90% of free radicals are produced by mitochondria, and the oxidative damage usually initiated from mitochondria.

In biochemistry, the free radicals of interest are often referred to as reactive oxygen species (ROS), i.e. superoxide radicals ($O_2^{\bullet -}$), peroxides (O_2^{2-}), and hydroxyl radicals (OH^{\bullet}), because the most biologically significant free radicals are oxygen-centered. ROS are involved in the cell growth, differentiation, progression, and death. Low concentrations of ROS may be beneficial or even indispensable in processes such as intracellular signaling and defense against micro-organisms. However, high amounts of reactive ROS participate in cell cycles resulting in cumulative damages to lipids and cell DNA. The expression of damages results in inflammation, cancers, age related diseases, and aging to mammals. In the last decades, Alzheimer's, Parkinson's diseases, diabetes, cardiovascular diseases, eye disease, cancers, obesity, aging, and many other diseases are found to relate to oxidative stresses caused by ROS [5,37,38]. However, not all free radicals are ROS and not all ROS are free radicals. For example, the free radicals superoxide and hydroxyl radical are ROS, but the ROS hydrogen peroxide (H_2O_2) is not a free radical species, however the term free radicals usually refer to these compounds in biology.

The free-radical theory of aging is that organisms age because cells accumulate free radical damage with the passage of time. The theory has some immediately attractive features, and is rational to explain human disorders and aging.

- Free radicals are produced during metabolism, sometimes these free radicals are detrimental and sometimes are for useful purposes. Once antioxidant defenses do not scavenge them completely, the ongoing oxidative damage to DNA, lipids, and proteins causes programmed cell death, cell mutation, or dysfunction of the cell.
- Production of free radicals can be envisaged as the consequence of genes selected because they confer benefits in early life. For example, facilitating signal transduction in early stage, diminishes infectious agents.
- The theory can explain the relation between metabolic rate, oxygen consumption and lifespan. The more oxygen consumed forms higher level of free radicals, thus cause more oxidative damages or reduce lifespan in mammals. However, higher metabolic rate does not cause shorter lifespan directly, since the activities of enzymes or proteins maybe greater so to reduce the damages by free radicals.

- Mitochondria are the energy plant in cells. The electron transport chain involved in metabolism, however the leakage of electrons in the transportation generate free radicals. The leakage of electrons is related to aging of mitochondria or insufficient enzymes and proteins in the chain reaction.
- The accumulation of free radicals causes lipid peroxidation and reduced proteins in mitochondria. It results in the release of cytochrome c and further lead to cell programmed death.
- Caloric restriction in mammals often decreases levels of oxidative damage to DNA, lipids, proteins, and attenuates age-related declines in repair systems.
- Long lived species usually have better antioxidant protection in regulation to rates of oxygen uptake than shorter-lived species.

In conclusion, free radicals cause oxidative damage to important molecules, further promote apoptosis or senescence that impair tissue renewal. Free radicals also generate inappropriate cellular signaling, and contribute to age-related diseases.

2.1.2 Modern Free Radical Theory in Biology

After the free radical theory in biology was proposed, the influences of ROS have been controversial since some studies found partially promote ROS level may be beneficial to lifespan of mammals [1]. On one hand, ROS are detrimental to cells and tissues. On the other hand, higher ROS level may stimulate enzyme activities and increase animal's lifespan [1]. Above all, it was found the redox states of mitochondrial protein, cytochrome c, are also crucial in apoptosis. It is because the reduced cytochrome c exhibits lower affinity to inner mitochondrial membrane. Once the inner mitochondrial membranes are peroxidized, the reduced cytochrome c can be released to inner mitochondrial membrane space. After all, the accumulated cytochrome c is released to cytoplasm and reacts with hydrogen peroxide, forming caspase proteins (precursors of apoptosis signaling). As cytochrome c is released from the inner mitochondria membrane, electron transportation in metabolic chain becomes short, so more electrons can be

released from the transport chain. This results in dramatic increases of free radical generation, and finally accelerates the progression of apoptosis (shown in Figure 2-1 (b)).

Free radicals play extremely important roles in the cytochrome c releasing processes. Free radicals cause lipid peroxidation in inner mitochondrial membranes; superoxide radicals reduce cytochrome c and peroxide oxidize cytochrome c before they were released to inner mitochondrial membrane space; peroxide oxidized the reduced cytochrome c in cytoplasm, forming caspase proteins. Although the redox states of cytochrome c are crucial in apoptosis, it is not proper to discuss whether the reduced state or oxidized state of cytochrome c is beneficial to cells. In conclusion, the oxidized cytochrome c is preferable in inner mitochondrial membrane, while the reduced cytochrome c can't form caspase proteins when cytochrome c is released [40,41,42,43].

In the modern free radical theory in biology, free radicals are no longer always detrimental to cells and tissues, but often adequate oxidative stress maybe beneficial to mammals. First of all, proper oxidative stress stimulates the generation of antioxidant enzymes, proteins, and assists to defend oxidative stress of detrimental levels. Second, proper oxidative stress adjusts the redox states of cytochrome c in mitochondria, forming oxidized cytochrome c, which has higher affinity to bond to mitochondrial membrane. Third, proper oxidative stress reduces cytochrome c when released, avoiding them from binding with other proteins to form caspase proteins. Instead of the cumulative damages caused by free radicals, the redox states of cytochrome c that altered by free radicals play a more influential role in modern free radical theory.

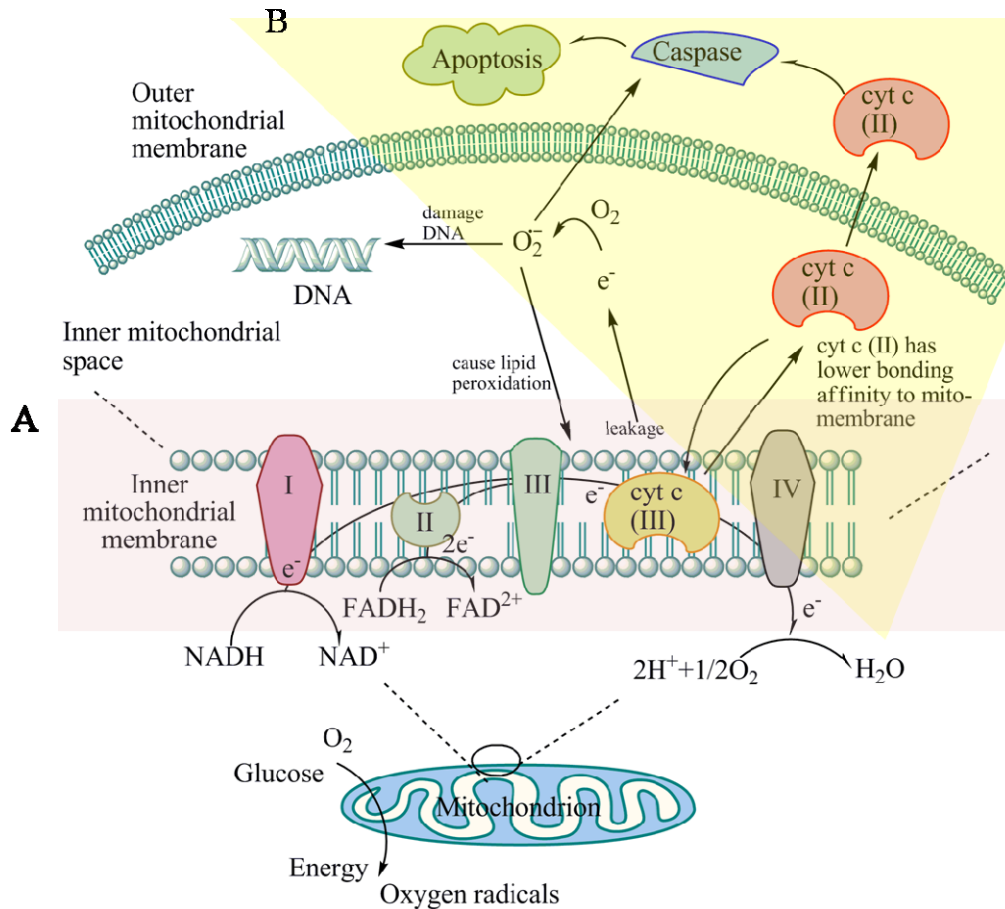


Figure 2-1. Metabolism in a mitochondrion. A) electron transport chain. B) modern free radical theory causing apoptosis. Figures made according to [1,2,40,41,42,43].

2.2 Antioxidant Defense in Biology and Medicine

2.2.1 Antioxidant Defense System

It has been demonstrated that administering free radical scavengers into biological systems allows improving cell's viability, cell's survival rates, and mammal's lifespan. Some free radical scavengers benefit cultures through removing free radicals catalytically, some through quenching free radicals, some through regulating mitochondrial redox potential, and the others protect cultures through stimulating the generation of antioxidants. They can be artificial or natural chemical compounds, proteins, or enzymes that execute electrochemical reactions with free radicals or regulate the redox states of mitochondria.

There have been broad categories of free radical scavengers reported. In this section, several major free radical scavengers and their functions are listed in Table 2-1.

Table 2-1. Genetic changes and the responded free radical scavengers that affect oxidative damage in living systems [1].

System/ factor affected by genetic change	Examples
Antioxidant defense enzymes	SOD, CAT, HO, peroxiredoxins
Low molecular mass antioxidant	Enzymes synthesizing and catabolizing GSH, ascorbate, urate, carnosine, bilirubin, biliverdin, etc.
Repair systems	Proteasome, Lon proteinase, other proteinase, DNA repair, PHGPx, enzymes that metabolize cytotoxic aldehydes, chaperones
Availability of transition metal ions “catalytic” for free radical reactions	Transferrin, ferritin, caeruloplasmin, metallothionein, haemopexin, haptoglobin, iron ion transporters, copper ion transporters, lactoferrin, haem oxygenases
Targets of oxidative damage	Alterations in conformation of proteins, DNA, chromatin, membranes, lipoproteins, etc.
Uptake or processing of dietary antioxidants	Vitamin C, E, carotenoids in guts, flavonoid
Regulate reactive species production	Cytochrome P450, NOX, oxidases producing superoxide and peroxide, other peroxidases
Rate at which oxidatively damaged cells die	P53, <i>bcl-2</i> , <i>bax</i> , genes affecting cell cycles and apoptosis/necrosis

Many studies have shown that these disorders or diseases caused by oxidative stress could be soothed or inhibited by administering adequate amounts of free radical scavengers, such as the most discussed enzymes heme oxygenase-1 (HO-1), enzyme SOD and CAT, into laboratory animals. Specifically, by exposing pancreatic tissues to SOD mimic compound, cell survival rates can be improved to three or four times comparing to untreated pancreas during isolation [44]. Such technical approach has been adopted in islet transplantation nowadays, in order to increase the preservation mass of transplanted islets. In addition, exposing pancreatic tissues to HO-1 can improve islet’s function in vivo after transplantation [45]. Specifically, exposing SOD and CAT-mimic compounds to wild type worms, flies, fungi, can increase their mean lifespan by

44%, 30%, and 600%, respectively [22,23]. Specifically, transgenic mice with over-expressed CAT in mitochondria can live 20% longer than wild type mice [24]. Overall, introducing sufficient amounts of free radical scavengers into biological systems allows to elevate cell culture's viability and survival rates under stress *in vitro*. Furthermore, *in vivo* studies show that the administration of free radical scavengers attenuates oxidative stress and inhibits the progression of disorders in animal models [13,19].

2.2.2 Alternative Antioxidant Defense Other Than Direct Free Radical Scavenging

Most antioxidant defense pathways are to scavenge free radicals endogenously. However, there are particular enzymes that actually are not scavengers, but to oxidize the reduced cytochrome c back into their functionalities in mitochondria. Peroxidases, which are also antioxidant defense enzymes, use peroxides to oxidize another substrate. This particular antioxidant defense pathway can be used to elucidate why the adequate amounts of hydrogen peroxide can benefit a biological system [1,46]. Furthermore, this antioxidant defense pathway also inhibits cytochrome c released through regulating its redox states, in which the peroxidase oxidize cytochrome c and so to create its bonding strength with inner mitochondrial membranes.

Amongst the enzyme peroxidases, cytochrome c peroxidase and NADH oxidase are the most important enzymes in the mitochondrial inner membrane space [47]. In the mitochondrial electron transportation chain cytochrome c peroxidase plays as complex IV, and it takes electrons away from the reduced cytochrome c (see Figure 2-1(a)). Lack of cytochrome c peroxidase, cytochrome c would be reduced by electrons and be released from mitochondria to trigger apoptosis [41,43]. The same protection is also true by enzyme NADH oxidase [37].

2.3 CeO_2 in Catalysis, Biology, and Medicine

CeO_2 and other CeO_2 -related materials are excellent catalysts that carry out catalytic reactions through the exchanging the electrons, holes, lattice oxygen, and oxygen ions with

ligands. Recently, CeO_2 was found to protect cultures in the stressed circumstances, and has been proven to improve cell culture's viability.

In this section, the background of CeO_2 will be introduced based on its catalytic properties. The hypothesis of free radical scavenging as well as the specific scenario related to catalysis of CeO_2 will be discussed. Following the discussion, the studies that used CeO_2 nanoparticles to benefit biological systems will be introduced in details. Finally the free radical scavenging mechanism that carried out by CeO_2 will be discussed according to the knowledge learned in references and the understanding of free radical theory in biology.

2.3.1 CeO_2 as Catalysts

Based on its extraordinary catalytic properties, CeO_2 and its related materials have been widely applied for the use in various catalytic systems, such as three-way catalysts (catalytic converters), solid electrolytes in solid oxide fuel cells, gas sensors, catalysts in water-gas shift reaction, and as oxygen storage materials [48,49,50,51,52,53]. The versatility of CeO_2 nanoparticles relies upon its behavior of nonstoichiometric lattice oxygen. In other words, the catalysis carried out by the concentration of mobile intrinsic defects, undoped CeO_2 , i.e. oxygen vacancies, dominates the designated chemical reactions occur via the exchange of oxygen species in the vicinity of CeO_2 surfaces [36].

2.3.2 CeO_2 Nanoparticles in Biomedical Applications

The therapeutic efficacy of CeO_2 nanoparticles was first discovered by Rzigalinski et al. [25,26]. In the incidence, the lifespan of CeO_2 nanoparticles treated to neuron primary cells was found to be improved up to six fold. Since then, the benefits of introducing CeO_2 nanoparticles into biological systems were confirmed in other cell lines and tissues both *in vitro* [27,54,55,56] and *in vivo* [57,58]. Among all the studies including this dissertation, it was found that the intracellular free radical concentration of those treated cultures remained at ordinary level, even

though the cultures were under serious stress. Thus, it is now convincing that CeO_2 nanoparticles are free radical scavengers, and protect cultures from apoptosis through antioxidant defense.

The benefits of introducing CeO_2 nanoparticles into biological systems were confirmed in different cultures and tissues both *in vitro* and *in vivo**. Specifically, the introduction of CeO_2 nanoparticles with size smaller than 20 nm into primary cultures [25,26], HT22 rodent neuronal cells [55], or into CRL8798 breast epithelial cells [56], led to improved cellular survival with survival rates approaching three to four times higher than control cells, when exposed to stressed environments. The efficacy of CeO_2 nanoparticles to scavenge reactive oxygen species has also been demonstrated *in vivo*. Specifically, in studies involving peroxide induced retinal degradation, delivery of CeO_2 nanoparticles directly into the vitreous of the mouse eye prevented against vision loss by protecting the retina from intracellular peroxides [58]. Another study investigating spinal cord repair demonstrated that the administration of a single dose of CeO_2 nanoparticles provided significant neuron-protection to adult rat spinal cord neurons [54]. Finally, intravenous administration of CeO_2 nanoparticles protected MCP-mice (monocyte chemoattractant protein (MCP)-1 transgenic mice) against the progression of cardiac dysfunction by attenuating myocardial oxidative stress, endoplasmic reticulum (ER) stress, and inflammatory processes [57].

In these studies and the results that obtained in our works, the benefits of administrating CeO_2 nanoparticles are consistent with the reduced oxidative stress in cell cultures. The reduction of oxidative stress supports the hypothesis that CeO_2 nanoparticles protect cultures by

* The dosages of CeO_2 nanoparticles used in the references are different from the molar concentrations that used in the following experiments. The concentrations used in the references are based on the assumption of 1,500 cerium atoms in a single CeO_2 nanoparticle, so the molecular weight of the particular CeO_2 nanoparticle is estimated as $172.12 \times 1,500 = 258,180$ g/mole. The molar concentration used in our studies are based on ionic concentration of CeO_2 , where the molecular weight is 172.12 g/mole.

scavenging excess amounts of intracellular free radicals. Although the researches that studying free radical scavenging properties of CeO_2 is absent, it has long been demonstrated that oxygen radicals act as intermediates in the catalysis carried out by CeO_2 .

2.3.3 Free Radicals in CeO_2

The mechanisms of free radical scavenging afforded by CeO_2 nanoparticles have been investigated in a variety of non-biological systems including fuel cells [59], catalytic converters [36,60], and gas sensors [6]. The applications of CeO_2 nanoparticles rely on the properties to exchange their lattice oxygen ions, electrons, holes, with reagent molecules. In the exchange processes, CeO_2 provides electrons to the reagent molecules, forming bonds in its vicinity, and finally react with second reagent molecules or lattice oxygen to generate the designated products. For example, in the oxygen storage process, oxygen molecules first adsorb on CeO_2 surface, transform into superoxide radicals ($O_2^{\bullet-}$), peroxide (O_2^{2-}), then oxygen ions (O^- , O^{2-}), and finally migrate into oxygen vacancies ($V_O^{\bullet\bullet}$) in the lattice [60,62,63]. The oxygen ions captured in CeO_2 lattice or the lattice oxygen in CeO_2 can be released, forming gaseous oxygen or becoming involved in other chemical reactions. The widely accepted mechanism to explain the surface oxygen exchange on CeO_2 nanoparticles is shown in Equation (2-1). Based on these and other efforts it is now believed that oxygen exchange on CeO_2 surface is triggered by the adsorption of oxygen molecules, followed by a transformation into superoxide radicals and peroxides, dissociation into oxygen ions, and finally migration into oxygen vacancies in the lattice. Such reaction has been observed at room temperature [64]. Using spectroscopic techniques, superoxide and peroxide radicals have been identified as intermediates of surface oxygen exchange on ceria surface, and the exchange of environmental oxygen and lattice oxygen has been observed at room temperature [62,64]. In addition, using atomic force microscopy and

scanning tunneling microscopy, both Namai et al. [65] and Esch et al. [63] have observed the migration of oxygen species into CeO_2 's surface oxygen vacancies at room temperature, with the mobility of oxygen species promoted as temperature increases. The widely accepted formula of oxygen exchange on CeO_2 surface is as follows:



Free radicals are involved in chemical reactions catalyzed by CeO_2 and oxygen deficient materials. For example, superoxide radicals on CeO_2 behave as active oxygen species in CO oxidation; N_2O , NO_2 , and NO radicals are detected on CeO_2 in NO reduction; hydroxyl radicals OH^\bullet on CeO_2 are found to participate in the water-gas shift reaction; and peroxide species on CeO_2 are found to oxidize hydrocarbon species CH_4 , C_2H_4 , C_3H_6 even at room temperature. In general, it has been demonstrated that active free radicals adsorbed on CeO_2 surface behave as triggers in various chemical reactions, and as a measure of active free radicals determined by the oxygen vacancy concentration in the lattice [66,67].

2.3.4 Hypothesis of CeO_2 Nanoparticles in Free Radical Scavenging

Although the exact process by which CeO_2 nanoparticles scavenge free radicals in biological systems is not known, one could hypothesize that it resembles the mechanism observed in non-biological systems. The ROS generated in biological systems are reactive. When CeO_2 nanoparticles are close to ROS, the electrons of free radicals may form bonds with mobile electronic carriers that provided by oxygen vacancies. These oxygen species then dissociated into oxygen ions and finally diffuse into the lattice. The total reaction becomes the exchange of environmental oxygen species and lattice oxygen. Thus, we hypothesize that intracellular free radicals, such as superoxide radicals and peroxides would act as intermediates in surface oxygen exchange. These oxygen species finally migrate into oxygen vacancies in

CeO_2 nanoparticles, and lattice oxygen may be emitted to form oxygen molecules in biological systems. The hypothesis that describes oxygen radical scavenging by CeO_2 nanoparticles is illustrated in Figure 2-2.

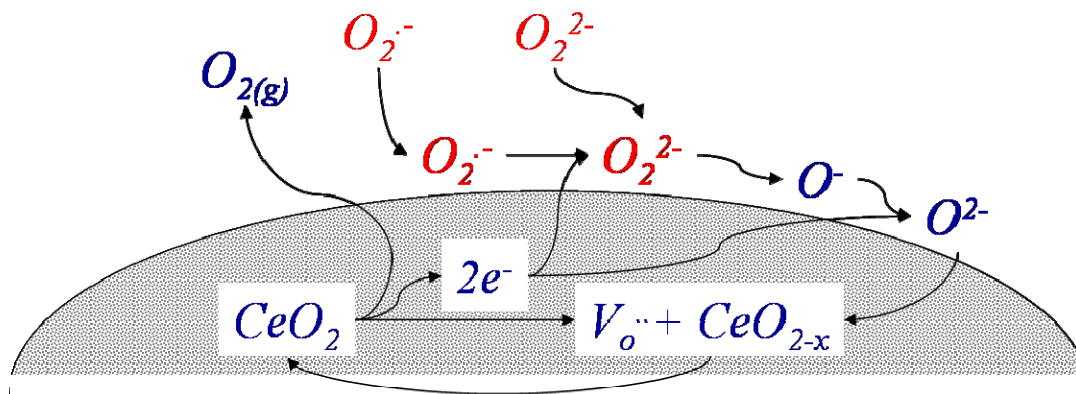


Figure 2-2. Hypothetic mechanism of free radical scavenging in the vicinity of CeO_2 surface. Oxygen vacancies ($V_o^{\cdot\cdot}$) provide sites for adsorption of superoxide radicals ($O_2^{\cdot-}$) and peroxides (O_2^{2-}). These metastable vacancies also thermally activate the transition of radicals into oxygen ions and migration into CeO_2 lattice.

2.3.5 Promote Catalytic Activity by Doping Zirconium into CeO_2

The catalytic properties of CeO_2 nanoparticles can be improved according to three principles. It can be improved intrinsically through exciting the electrons and holes through band gap. It can be improved extrinsically through adding impurities in the lattice. Or, it can be improved stoichiometrically by increasing the oxygen vacancy concentration in the lattice. In general, the catalytic properties of CeO_2 can be improved by doping a broad variety of elements. In this dissertation, doping zirconium into CeO_2 is selected to achieve the improvement [36].

CeO_2 has a face-centered cubic unit cell with space group Fm3m. In this structure, each cerium cation coordinates eight equivalent nearest-neighbor oxygen anions at each corner of the cube, and each anion tetrahedrally coordinates four cations [36]. Both ZrO_2 and CeO_2 have cubic fluorite structures. Mixing the two materials in solid solutions will form a pyrochlore

structure (shown in Figure 2-3). The defect-rich pyrochlore structure is the result of misfit of zirconium and cerium ionic radii (0.084 nm and 0.097 nm, respectively) in the structure. In addition, the relatively stable quadricivalent zirconium cations sit on trivalent/quadrivalent cerium sites leading to the formation of extra oxygen vacancies in the solid solution, thus decreasing coordination numbers, and expanding their lattice parameters. Several studies have found that the concentration of trivalent cerium ions in $Ce_xZr_{1-x}O_2$ solid solutions is promoted as more quadricivalent zirconium doping in the lattice [68,69,70]. As the results, the improved catalytic properties in zirconium doped CeO_2 are contributed nonstoichiometrically (i.e. via increasing oxygen vacancies) and extrinsically (i.e. via other defects). Utilizing this concept, the concentration of charge carriers in $Ce_xZr_{1-x}O_2$ solid solutions is promoted and so their catalytic activities are improved.

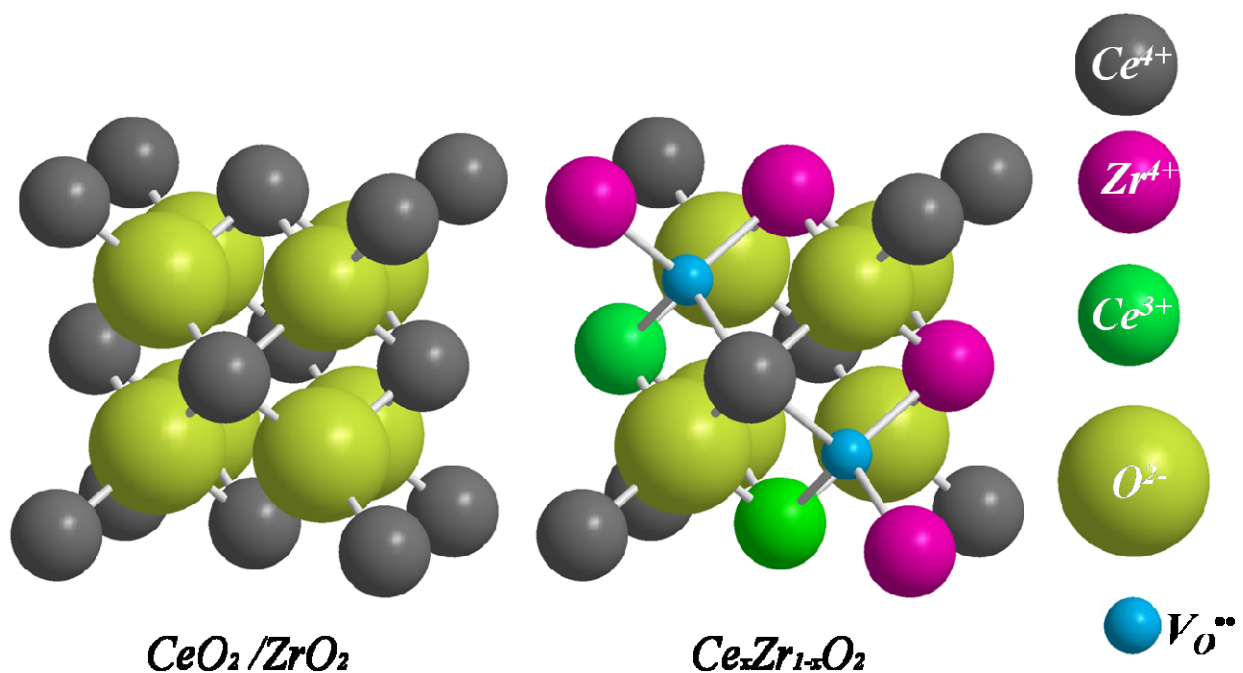


Figure 2-3. Schematic diagrams showing cubic fluorite (left) and pyrochlore (right) structures for CeO_2/ZrO_2 and $Ce_xZr_{1-x}O_2$, respectively. Figures made according to [36].

The catalytic activities of $Ce_xZr_{1-x}O_2$ nanoparticles are usually evaluated by measuring their oxygen storage capacity (OSC). OSC represents a measure of the oxygen vacancy concentration in metal oxides, and directly correlates to a catalyst's performance, such as in catalytic converters, catalytic combustions, water-gas shift reactions, and oxygen storage materials. It has been demonstrated that $Ce_xZr_{1-x}O_2$ nanoparticles exhibit up to four times higher OSC when 20-40% of cerium ions in the solid solutions were substituted by zirconium ions at low (400□) and high temperatures (1000□) [71,72]. As aforementioned, it is hypothesized that oxygen vacancies mediates free radical scavenging by $Ce_xZr_{1-x}O_2$ nanoparticles. Therefore, preparing $Ce_xZr_{1-x}O_2$ nanoparticles of variant amounts of lattice oxygen vacancy and test their activities against free radicals may provide clues to examine the hypothesis that free radical scavenging is mediated by lattice oxygen vacancies.

2.3.6 Introduction of $Ce_xZr_{1-x}O_2$

$Ce_xZr_{1-x}O_2$ undergoes three major phase transformations at ambient temperature with elevated zirconium concentrations (shown in Figure 2-4) [73,74]. At ambient temperature, $Ce_xZr_{1-x}O_2$ sustained in cubic fluorite structure (c) when 0 – 15% of zirconium containing in the crystal structure. The cubic fluorite phase undergoes to two metastable phases, t'' and t' , and then to tetragonal structure (t) in the intermediate zirconium containing range (15 – 90 %). The t' phase is a phase through a diffusionless transition from t phase, and the t'' phase is a intermediate phase between t' and c phases. The t'' phase shows no tetragonality of the sublattice and it exhibits an oxygen displacement from ideal cubic fluorite sites, so t'' phase is usually referred to as a cubic phase. Finally, at higher than 90 % of zirconium containing, $Ce_xZr_{1-x}O_2$ undergoes to monoclinic or the mixture of tetragonal and monoclinic (m) structures at ambient temperature. Table 2-2 shows the classification of phases in $Ce_xZr_{1-x}O_2$ with elevated zirconium concentration in the lattice.

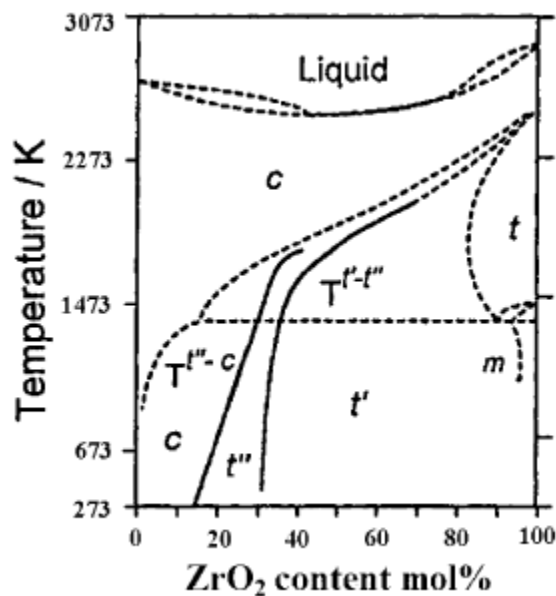


Figure 2-4. Phase diagram of the CeO_2 - ZrO_2 binary system [73].

Table 2-2. Classification of the phases in the CeO_2 - ZrO_2 binary system [36].

Phase	Composition range (%mol Ce)	Tetragonality (c/a)	Space group
Monoclinic (<i>m</i>)	0-10	N/A	$P2_1/c$
Tetragonal (<i>t</i>)	10-30	>1	$P4_2/nmc$
Tetragonal (<i>t'</i>)	30-65	>1	$P4_2/nmc$
Tetragonal (<i>t''</i>)	65-80	1	$P4_2/nmc$
Cubic (<i>c</i>)	80-100	1	$Fm\bar{3}m$

The phase transformation of $Ce_xZr_{1-x}O_2$, however, could be dependent on different synthesis methods, particle size, or tempering procedures. For instance, the phase transformation was found to postpone to higher zirconium containing range while the particle size was engineered as small as 10 nm (shown in Figure 2-5) [75]. Specifically, the targeted particle size

in this study is smaller than 10 nm, therefore the phase transformation could be expected in the nanoparticles containing higher zirconium, when prepared in reverse micelle synthesis.

The phase transformation of $Ce_xZr_{1-x}O_2$ can be distinguished by using XRD and Raman spectroscopy. Using XRD, the transition from cubic to tetragonal phase can be identified by the tetragonal features next to XRD peak (220). On the other hand, the transition of sub-structures, i.e. c , t'' , and t' phases, can be identified using Raman spectroscopy due to the phonon excitation which is induced by the symmetry of lattice structures. The methodology to distinguish the crystal structures as well as phase transition is shown in Figure 2-6.

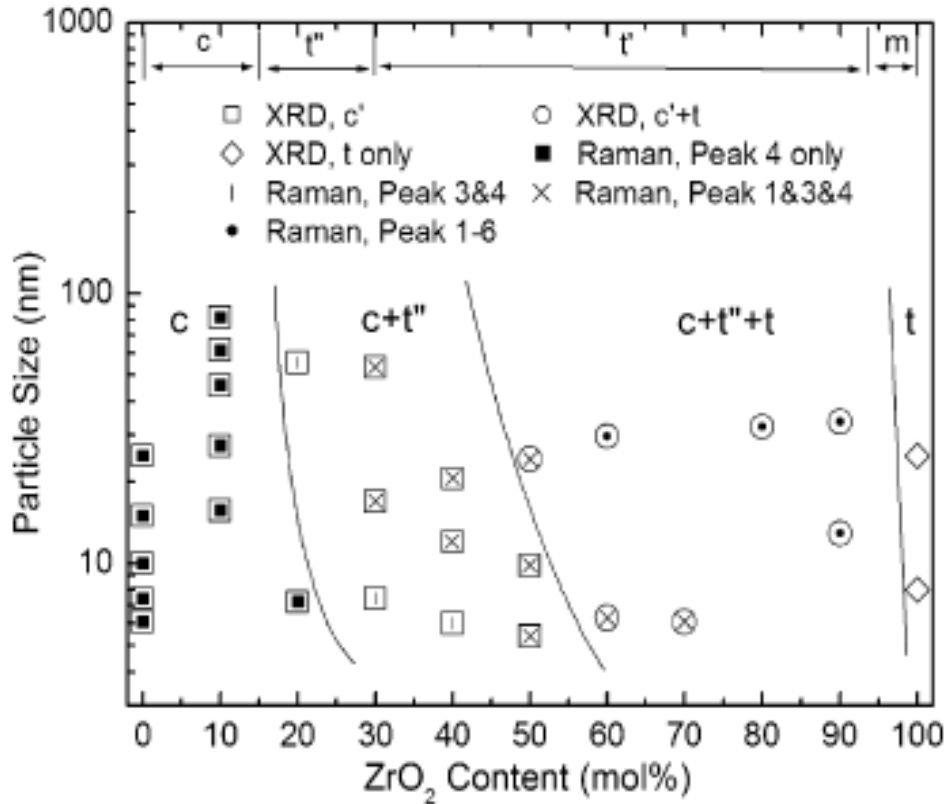


Figure 2-5. Phase transition of CeO_2 - ZrO_2 binary system. The transitions are particle size dependent [75]. The phase transitions were distinguished by XRD associated with Raman spectroscopy. Figure reproduced from [75].

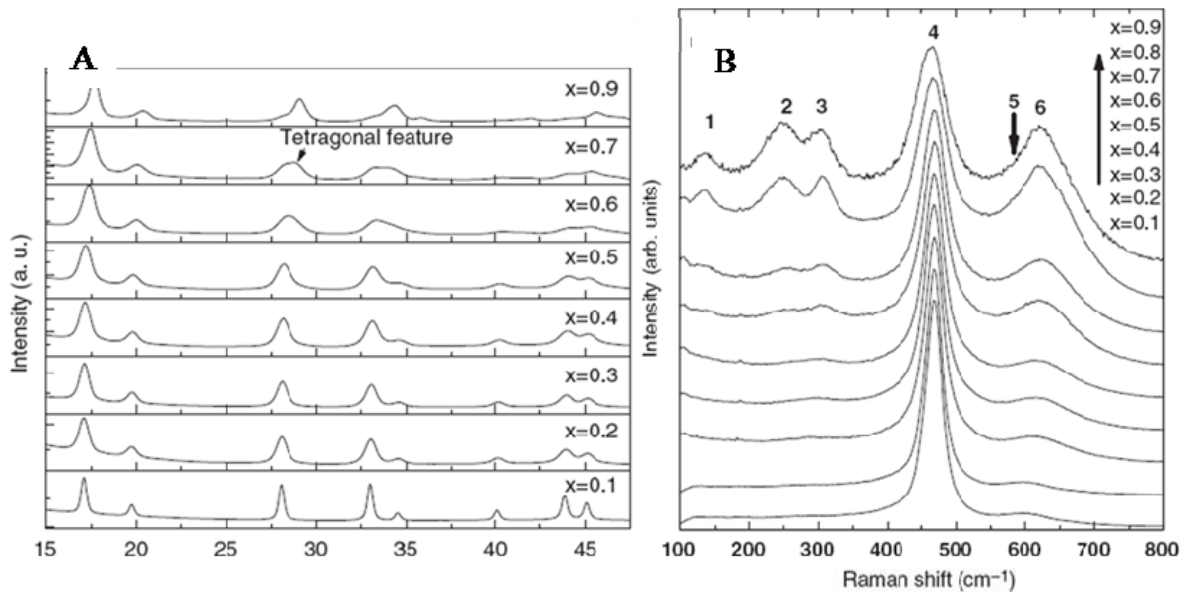


Figure 2-6. XRD and Raman spectra of $(1-x)\text{CeO}_2-x\text{ZrO}_2$. A) XRD of $(1-x)\text{CeO}_2-x\text{ZrO}_2$ show the phase transition from cubic fluorite to tetragonal phase. B) Raman shift of $(1-x)\text{CeO}_2-x\text{ZrO}_2$ show the phase transition of sub-structures. Figures reproduced from [75].

CHAPTER 3

TEST HYPOTHESIS WITH CELL CULTURES

The therapeutic efficacy of CeO_2 nanoparticles has been demonstrated in various cell cultures. The successful outcomes of viability improvements in the treated cultures have been demonstrated to be true both *in vitro* and *in vivo*. In this chapter, the experiments are designed to elucidate the mechanism of viability enhancement that contributed by CeO_2 nanoparticles. For the experimental setups, CeO_2 nanoparticles were administered into β TC-tet cells, and the endogenous oxidative stress in cell cultures was evaluated. The results suggest that CeO_2 nanoparticles serve as free radical scavengers in biological systems, and their scavenging properties most likely are through catalysis. The evidence in this chapter supports the concept that enhancing the catalytic activities of CeO_2 nanoparticles may allow decreasing the dosages in biological systems for the same therapeutic efficacy. This chapter also serves as a demonstration of previous chapters, where the results implied the alternative platforms providing a novel therapy to human disorders. The contents in this chapter are based on the paper that the author published in *Nanomedicine* [27].

3.1 Methodology

To test the hypothesis and further establish the fundamental knowledge of this technique for islet transplantation *in vivo*, we tested β TC-tet cell lines that treated with CeO_2 nanoparticles in response to raised oxidative stress. The β TC-tet cell lines are murine insulinoma cells. They are modified from β cells in islet of Langerhans in the pancreas. The β TC-tet cell lines' function is similar to primary β cells, so they are optimum cell lines for preliminary studies in biochemistry.

The β TC-tet cells are treated with the CeO_2 nanoparticles synthesized in our lab. It is required to note that the preparation of CeO_2 nanoparticles in the sequent sections of this chapter

is different to the CeO_2 nanoparticles in the other chapters. Essentially, a different surfactant, lecithin was used to synthesize CeO_2 nanoparticles in this chapter, while $Ce_xZr_{1-x}O_2$ nanoparticles in the following chapters were prepared in a reverse micelle system formed by surfactant, bis(2-ethylhexyl) sulphosuccinate (AOT).

Delineating the *in vitro* and *in vivo* scavenging mechanism of CeO_2 nanoparticles is important in furthering our understanding of these particles and extending their potential biological and medical applications. To do so, it is necessary that CeO_2 nanoparticles are colloidally stable in solution for extended periods of time because biological systems may require prolonged incubations to achieve optimum efficacy. In the previous works, CeO_2 nanoparticles were synthesized and then stabilized in a solution of multivalent dispersants. A solution of tri-sodium citrate was applied to stabilize CeO_2 nanoparticles by shifting CeO_2 nanoparticles' isoelectric point (IEP).

The intracellular concentration of CeO_2 nanoparticles in murine insulinoma β TC-tet cells, a well accepted surrogate for *in vitro* studies of islet cell viability, was quantified and their ability to scavenge free radicals *in vitro* was assessed by exposure to hydroquinone.

Synthesis of CeO_2 nanoparticles

Phosphatidylcholine (laboratory grade), toluene (laboratory grade), cerium (III) nitrate hexahydrate (99.5%, M.W. = 434.22 g/mole), and ammonium hydroxide (NH₃ content 28~30%) were purchased from Fisher Scientific and used without further purification. 2.285 gram of phosphatidylcholine was dissolved in 100 ml of toluene to form reverse micelles. Five mini-liter of 0.1 M cerium nitrate aqueous solution was pipetted into the colloidal micelle system, and the mixture was strongly stirred for 30 min until the system appeared homogeneous. Ten mini-liter of 1.5 M ammonium hydroxide solution was titrated into the system to initiate electrochemical

reaction. After 45 min of stirring, CeO_2 nanoparticles gradually formed in the reverse micelles. The nanoparticles were collected by centrifugation with a force field of 18 G and then sequentially rinsed with 50 ml of methanol, 50 ml of ethanol, and 50 ml of water in order to remove the redundant surfactants. Between each rinse the nanoparticles were collected by centrifugation at 18 G.

Colloidal stabilization of CeO_2 nanoparticles

The CeO_2 nanoparticles were dispersed in 100 ml of 0.05 M (13.17g/l) saline/sodium citrate buffer (Cat. # 821840, MP Biomedical) and ultrasonicated until the appearance of the suspension changed from turbid to transparent. The pH value of suspension was adjusted to 7.4 using 0.1N citric acid and sodium hydroxide solutions. The suspension was sterilized by filtration with a 0.2 μ m filter. The average yields from such preparation were approximately 50 mg of CeO_2 nanoparticles stabilized in 100 ml of sodium citrate solution.

Concentration analysis

The yields and concentration of CeO_2 suspensions were determined by Perkin-Elmer Plasma 3200 inductively coupled plasma spectrometer (ICP). The ICP sample was prepared by dissolving 1 ml of the suspension in 1 ml of 95% sulfuric acid (Acros Organics). After heating to 90°C for 24 hrs, the sample was diluted to 5ml with deionized water for ICP measurement.

Structural characterization

The crystal structure and crystallite size of CeO_2 nanoparticles were characterized by X-ray diffraction (XRD) using $CuK\alpha$ radiation (XRD Philips APD 3720). For the preparation of the XRD sample, CeO_2 nanoparticles were extracted before stabilization and dried in air for 24 hrs.

Micrographs and electron diffraction pattern were determined using a JEOL 2010F transmission electron microscope (TEM) equipped with selected area diffraction (SAD). For the

preparation of TEM samples, CeO_2 nanoparticles were extracted before stabilization and dried on carbon formvar-coated grids (Electron Microscopy Sciences).

Stability tests

The stability of CeO_2 suspensions was determined by measuring the zeta potential of the suspension using a Brookhaven ZetaPlus. One tenth mini molar of citrate-adsorbed CeO_2 nanoparticles and citrate-free CeO_2 nanoparticles were prepared, and 0.1 vol% of potassium chloride was added to define the background electrolyte. The pH of the sample was adjusted by titrating a trace amounts of 0.1 N hydrochloric acid and 0.1 N sodium hydroxide into the suspensions.

Cell culture

Murine insulinoma β TC-tet cells were provided by the laboratory of Shimon Efrat (Albert Einstein College of Medicine, Bronx, NY) and cultivated as monolayers in Dulbecco's Modified Eagle's Medium (DMEM) (Mediatech, Herndon, VA). This medium contains 20 mM glucose and is supplemented with 10% (v/v) fetal bovine serum (Hyclone, Logan, UT), antibiotics (100 U/ml penicillin and 100 ng/ml streptomycin), and L-glutamine to a final concentration of 6 mM (Sigma, St. Louis, MO). Cultures were maintained at 37 °C under humidified (5% CO_2 /95% air) conditions, and appropriate media were completely replaced every 2-3 days.

Quantification of intracellular CeO_2 nanoparticles

The intracellular amount of CeO_2 nanoparticles was determined by ICP. β TC-tet cells were incubated in media containing 0, 50, 100 and 200 μ M CeO_2 for 48 hrs. At the end of this incubation period, the cells were washed with PBS 2-3 times to remove all extracellular CeO_2 nanoparticles. A pellet of 20-40 millions cells was generated by centrifugation and digested in 1ml of either 95% sulfuric acid for 48 hrs at 60 °C. The sample was then diluted with 5ml with

deionized water before proceeding with the ICP measurements. Samples with 0 μM CeO_2 were actually prepared as “sham” controls, meaning that a volume of the vehicle solution (i.e., citrate) equal to the volume of the CeO_2 nanoparticle solution was added to the cells.

The same cultures used to determine the intracellular cerium concentration were also used to visualize the intracellular distribution of the nanoparticles with TEM microscopy. TEM images of CeO_2 exposed and sham treated control $\beta\text{TC-tet}$ cells were obtained with a JEOL 2010F microscope to visualize the intracellular compartmentation of the CeO_2 nanoparticles. Chemical analysis was performed by energy dispersive spectrum (EDS) built in the same TEM microscope.

Quantification of intracellular free radical concentration

The ability of citrate-coated CeO_2 nanoparticles to scavenge free radicals *in vivo* was assessed by the following protocol. $\beta\text{TC-tet}$ cells were cultured as monolayers in T-75 flasks and incubated overnight (~18 hrs) with DMEM media that contained 0, 100 or 200 μM CeO_2 nanoparticles. Each flask contained between 30-40 million cells. At the end of the labeling period, the cells were rinsed 2-3 times with PBS to remove extracellular CeO_2 nanoparticles, trypsinized, centrifuged, and the cell pellet re-suspended in 20 ml of fresh non- CeO_2 containing DMEM. Aliquots of 4 ml were placed in separate centrifuge tubes. The freely suspended cells were exposed for 15 min to media that were supplemented with an aliquot from a stock solution of hydroquinone (HQ) so that the final hydroquinone concentration in the media was 1 or 2 mM. Cells exposed to 0 mM HQ were in fact sham treated with a volume of PBS equal to that of the stock HQ solution that was added to reach 2 mM. The stock HQ solution was prepared by dissolving 8 mg HQ in 0.5 ml of dioxane and then diluted with 9.5 ml of PBS. At the end of the 15 min HQ treatment the cells were centrifuged, the media discarded and 200 μl of 2',7'-

dichlorofluorescein diacetate (DCF) (Molecular Probes, Eugene OR) were added to suspend the cells. Each 200 μl suspension was placed in a single well of a 96-well plate and the plate was placed in a Synergy HT reader (Bio-Tek, Winooski, VT) and allowed to incubate at 37 °C for 20 mins. Fluorescence was measured using an excitation filter centered at 480 nm and an emission filter centered at 520 nm. These experiments were repeated 3 times.

Analytical assays

For all experiments described above the viability of $\beta\text{TC-tet}$ cells following exposure to CeO_2 nanoparticles was assessed by a commercially available assay based on the detection of MTT (3-(4,5-dimethylthiazol-2-yl)-2,5-diphenyl-tetrazolium bromide) (Molecular Probes, Eugene, OR), while the amount of insulin secreted in the media was measured by using mouse insulin Elisa based immunoassay kit (ALPCO, Windham, NH).

3.2 Results and Discussion

To visualize the CeO_2 nanoparticles and measure their physical dimensions, TEM micrographs of the nanoparticles were obtained. Figure 3-1(a) shows the image and diffraction pattern (up right) of CeO_2 nanoparticles under such preparations. Based on this and similar images from other preparations, we deduce that the CeO_2 nanoparticles are equiaxed, of monodispersed particle size. The SAD pattern indicates that these CeO_2 nanoparticles were highly crystallized. The size of the CeO_2 nanoparticles range between 2 nm and 6 nm for all preparations synthesized in this study. We arbitrary selected 50 nanoparticles in TEM images and measured their Feret's diameter, and the size distribution upon such estimation has been shown in Figure 3-1(b). The average particle size is 3.7 nm, and the error is estimated as 0.5 nm due to the contrasts of TEM images.

Figure 3-2 shows an XRD spectrum of the synthesized CeO_2 nanoparticles, and the diffraction peaks indicate that these particles are crystalline CeO_2 with fluorite crystal structure. The diffraction peaks (111), (200), and (220) crystal planes are used to calculate these particles' crystallite size. Using Scherrer's equation, $D_{hkl} = 0.89\lambda / \beta_{hkl} \cos\theta$, the crystallite sizes are calculated as 3.7 ± 0.6 nm, 3.9 ± 0.7 nm, and 3.6 ± 0.6 nm from diffraction peaks (111), (200), (220), respectively. The average crystallite size is 3.7 ± 0.2 nm after calculation: this value corroborates the average particle size determined by TEM and implies that each of these CeO_2 nanoparticles is a single crystallite.

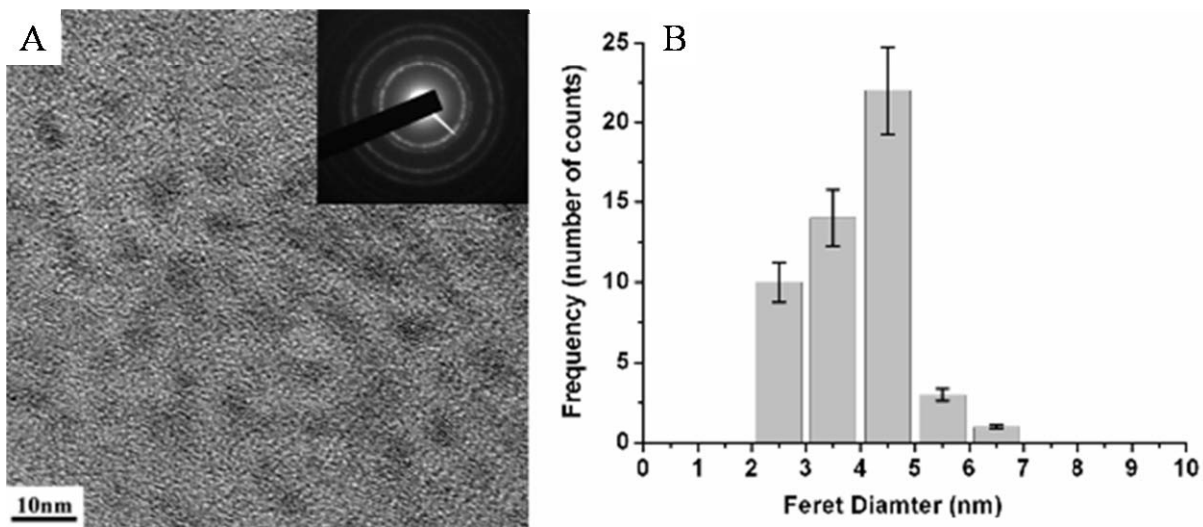


Figure 3-1. TEM micrographs of CeO_2 nanoparticles that were synthesized using surfactant lecithin. A) TEM image of CeO_2 nanoparticles (scale bar 10 nm). Diffraction pattern associated with TEM shows that the synthetic nanoparticles are highly crystallized. B) Particle size distribution calculated from 50 arbitrary selected particles in TEM images. The average Feret's diameter of synthetic nanoparticles is 3.7 nm.

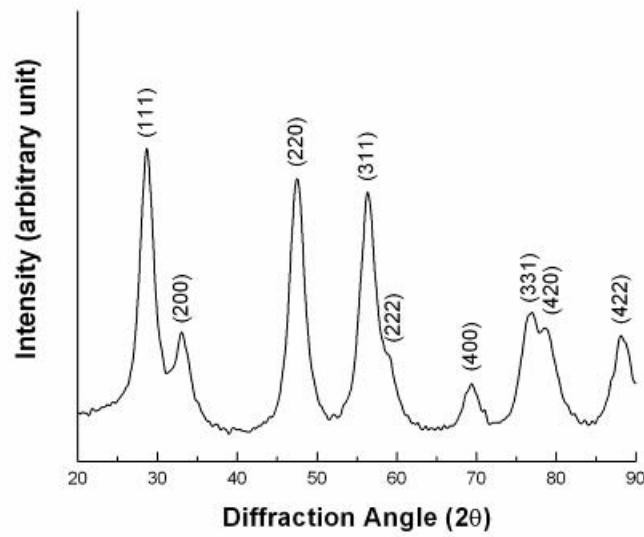
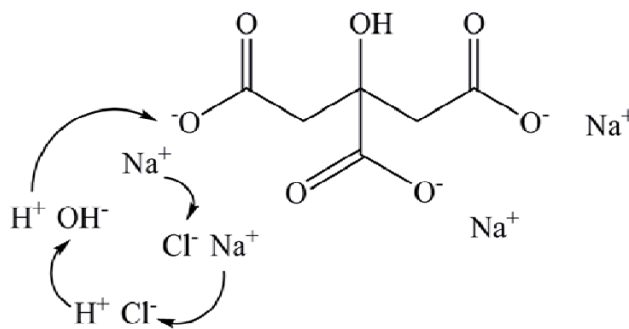


Figure 3-2. XRD pattern of CeO_2 nanoparticles. The mean crystallite size of these particles is calculated as 3.7 ± 0.2 nm using Scherrer's equation.

In order to minimize the influences from agglomerations and concentration gradients that may occur in the growth medium, it is necessary for CeO_2 nanoparticles to be well dispersed in the medium. Unfortunately, the isoelectric point (IEP) of CeO_2 nanoparticles is around 6.5 to 7.5, whereas the CeO_2 nanoparticles tend to agglomerate at the targeted pH value, 7.4. Here, we used tri-sodium citrate molecules as dispersants, since tri-sodium citrate has been used to disperse CeO_2 nanoparticles through shifting the isoelectric point of CeO_2 . Using tri-sodium citrate, the IEP of CeO_2 is shifted to lower pH values, therefore at pH 7.4 CeO_2 have strong negative electrostatic charges on their surface, resulting in stabilization effects. The other advantage of using tri-sodium citrate is due to its pH buffering properties. Tri-sodium citrate and its salts have been used to make pH buffers as well as anti-coagulation solutions at pH 7.4. Therefore, tri-sodium citrate buffer was used as dispersing solution as well as pH buffer in this study. Figure 3-3 shows the major chemical compositions in tri-sodium citrate buffer. Figure 3-4 presents the zeta potential of a citrate-adsorbed and a citrate-free CeO_2 suspension at various

pH values. Comparing both zeta potential profiles, we conclude that IEP of CeO_2 shifts from 8 to approximately 2 when the nanoparticles are stabilized in citrate solution. The shift of IEP is a result of surface charge modification due to the adsorbed citrate on CeO_2 nanoparticles. The zeta potential of citrate treated nanoparticles shifts from +10 mV to -38 mV at pH 7.4, which indicates the promotion of surface charges on the CeO_2 particle surface, and provides CeO_2 nanoparticles sufficient electrostatic repulsion to avoid flocculation. The citrate treated suspension is able to retain transparency without visible deposition of particles for at least 60 days.



Chemical Compositions of Saline/Tri-sodium Citrate Buffer:

1. Sodium citrate
2. Sodium chloride
3. Hydrochloric acid
4. Sodium hydroxide

Figure 3-3. Chemical compositions of the tri-sodium citrate buffer.

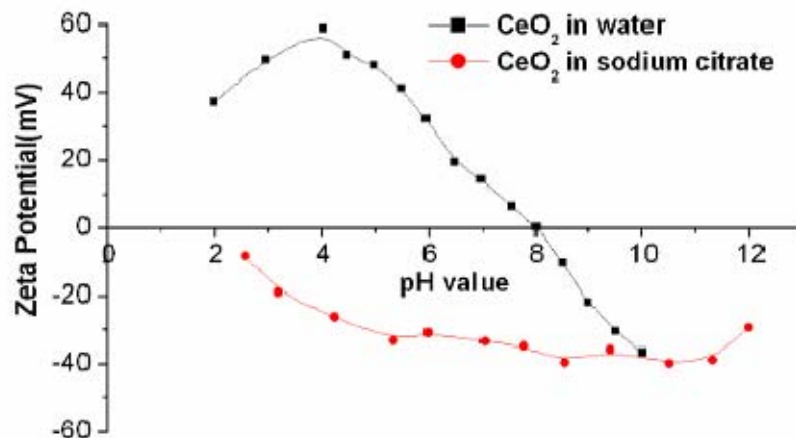


Figure 3-4. Zeta potentials of CeO_2 suspensions as a function of pH.

Stabilization of CeO_2 nanoparticles with citrate imposes two key advantages. First, it extends the shelf-life of the nanoparticle solution, permitting the performance of longitudinal studies with the same nanoparticle preparation. Second, it minimizes, if not eliminates, the precipitation of CeO_2 nanoparticles from solution. Consequently, the nanoparticle distribution within the solution is homogeneous; allowing for uniform delivery of the nanoparticles to cells either *in vitro* or *in vivo*. Alternatively, partial precipitation of CeO_2 nanoparticles could lead to a heterogeneous delivery because the local CeO_2 concentration in the vicinity of cells may be altered, resulting in a variable intracellular uptake of the nanoparticles.

A key parameter in assessing the efficacy of CeO_2 nanoparticles to scavenge reactive oxygen species is the intracellular concentration and compartmentation of the CeO_2 nanoparticles. To quantify the intracellular concentration of CeO_2 nanoparticles, β TC-tet cells were incubated in the modified media containing 0, 50, 100 and 200 μ M CeO_2 for 48 hrs. At the end of this incubation period, the cells were digested and the concentration of CeO_2 nanoparticles was determined by ICP. Table 3-1 shows the CeO_2 concentrations in β TC-tet cells after 48 hours of incubated in different extracellular concentrations. The data show that the

accumulation of CeO_2 in β TC-tet cells proportion to the extracellular concentration. However, exposure of β TC-tet cells to large concentrations of citrate-adsorbed CeO_2 nanoparticles in the culture media ($>200 \mu\text{M}$) was detrimental to the cells. This is illustrated by the lower number of cells that were measured when cells were exposed to media containing $200 \mu\text{M}$ CeO_2 . Since all flasks used in this experiment were prepared identically, this lower cell count may be attributed to (1) detachment of cells during the incubation period, (2) a decrease in the rate of proliferation by the cells or (3) combination of (1) and (2). It is important to note that cell viability was measured on the cells that were used to quantify the intracellular CeO_2 content and does not include cells that may have been detached during incubation with the nanoparticles.

Once the intracellular concentration of CeO_2 nanoparticles was determined (Table 3-1), we proceeded to determine the intracellular allocations of CeO_2 nanoparticles. CeO_2 nanoparticles are clearly visible in a TEM picture of β TC-tet cells. Figure 3-5 shows the allocations of CeO_2 nanoparticles in the treated cells. These data showed that CeO_2 nanoparticles were present throughout the cytoplasm as well as within organelles such as the mitochondrion, either as small or large aggregates. TEM cell samples were examined by EDS and the presence of cerium was clearly detected.

Table 3-1. Intracellular amount of CeO_2 in β TC-tet cells following 48 hrs of incubation with media containing CeO_2 nanoparticles.

Extracellular CeO_2 concentration (μM)	ICP Reading (μg)	Cell Numbers ($\times 10^6$)	Amount of CeO_2 in Cell (pg/cell)	Viability
0	0.24	49.8	0.01	>90%
50	2.33	42.3	0.06	>90%
100	4.59	42.6	0.11	>90%
200	7.8	22.2	0.35	>90%

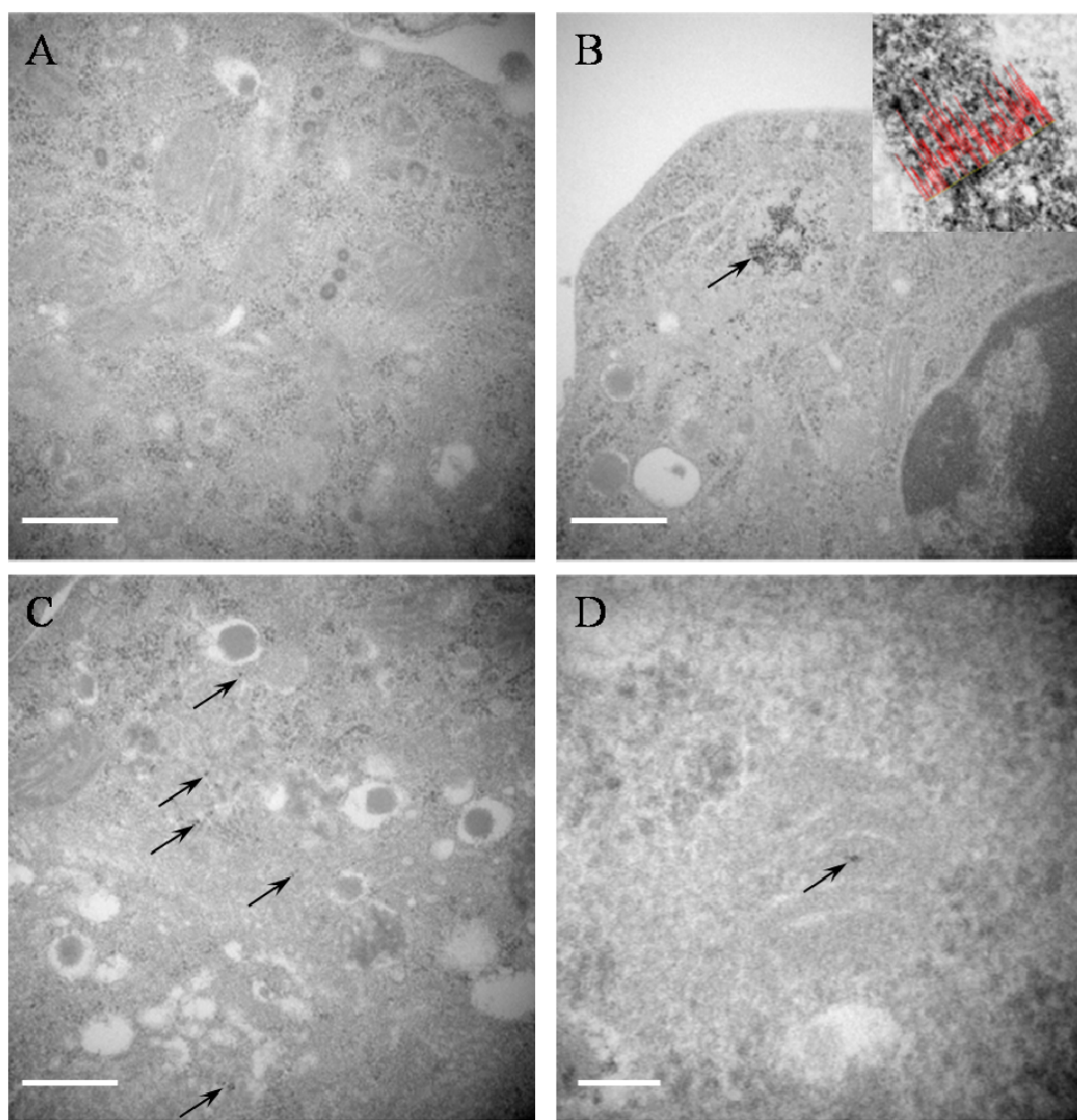


Figure 3-5. TEM micrographs of CeO_2 nanoparticles in β TC-tet cells. A) Control cell without not exposure to CeO_2 nanoparticles. B) A large aggregate of CeO_2 nanoparticles positioned in the cytoplasm of a β TC-tet cell following a 48 hr exposure to media containing 100 μ M CeO_2 nanoparticles. C) Small aggregate of CeO_2 nanoparticles that are distributed throughout the cytoplasm of the same cell in B. D) A small aggregate of CeO_2 nanoparticles that is positioned within the mitochondrion of the same cell in B and C. The EDS chemical analysis is shown on the upper right corner of the image, indicates the presence of cerium in the pointed spots. Scale bar 500nm in A-C, and 100 nm in D.

The effectiveness of these citrate-adsorbed CeO_2 nanoparticles to scavenge intracellular free radicals was assessed by exposing β TC-tet cells to 1 or 2 mM HQ for 15 min. Figure 3-6

indicates the effect of HQ exposure on the intracellular free radical concentration. The data show that in the absence of CeO_2 nanoparticles such an insult results in an increase in the intracellular free-radical concentration. However, when cells were preloaded with either 50 or 100 μM CeO_2 , the intracellular free radical concentration decreased regardless of the extracellular hydroquinone concentration. These data represented the effectiveness of CeO_2 nanoparticles to scavenge free radicals *in vitro*. It is important to note that labeling β TC-tet cells with CeO_2 nanoparticles did not affect either their viability of the cells as depicted in Table 3-1 or their ability to secrete insulin as it is illustrated in Figure 3-7. These data support earlier reports demonstrating the neuroprotective, ophthalmoprotective, and cardioprotective properties of CeO_2 nanoparticles, although the CeO_2 concentrations in our work were up to 4 orders of magnitude higher than in the above reports. However, our data is based on quantitative measurement of the concentration via full chemical analysis using ICP which should be the standard applied to measure concentrations. The earlier papers based their calculated concentrations on a qualitative picture analysis.

Another important observation from our experiments was the lack of cytotoxic effects associated with the use of the CeO_2 nanoparticles. This observation is in contrast to a recent *in vitro* study on human lung cancer cells that demonstrated a significant decrease in cell viability with exposure to CeO_2 nanoparticle [76]. The loss of cell viability was attributed to large quantities of free radicals generated by the nanoparticles resulting in excessive oxidative stress. Although the doses of CeO_2 nanoparticles used in that study is similar to that used in the present study (i.e., Lin et al. used 3.5-23.3 $\mu g/ml$ for 1-3 days, while our present study used 17.2-34.4 $\mu g/ml$ for 2 days), the effect of the nanoparticles is opposite. Whereas Lin et al. reported generation of free radicals, we report scavenging of free radicals. This difference in function

may be attributed to the reported photocatalyst-nature of CeO_2 nanoparticles ($E_g = 3.15\text{eV}$) upon the illumination of UV lights [77]. However, higher energy is required to stimulate free radical formation by our CeO_2 nanoparticles, since the broader bandgap energy (3.65eV in terms for 3.7 nm CeO_2 nanoparticles) was reported for CeO_2 nanoparticles smaller than 20 nm [78] (i.e., Lin et al. used 20 nm particles whereas we used 3.7 nm particles).

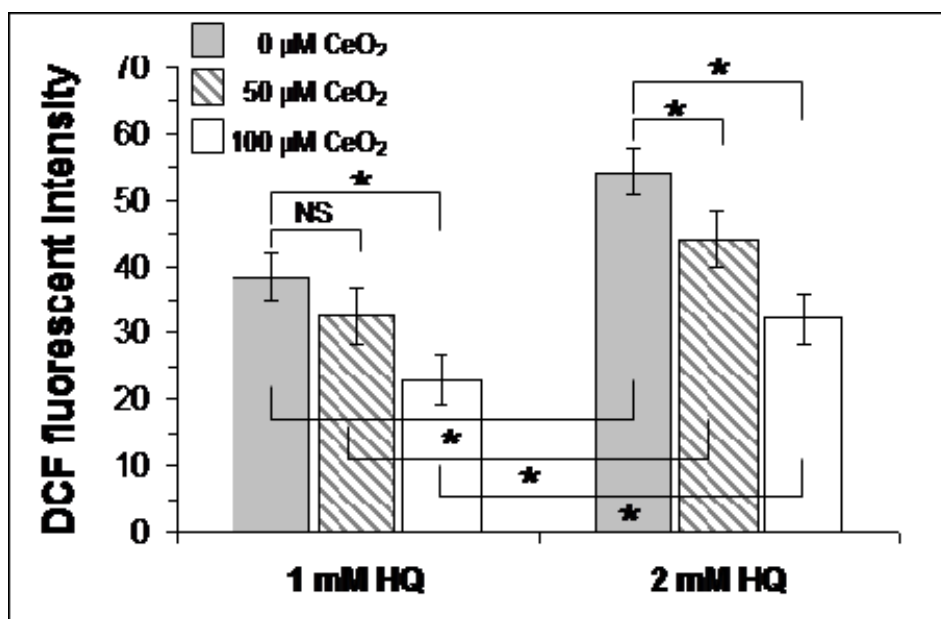


Figure 3-6. Free radical concentration in $\beta\text{TC-tet}$ cells. The solid gray bars represent intracellular free radical concentrations of non- CeO_2 loaded $\beta\text{TC-tet}$ cells following exposure to 1 or 2 mM hydroquinone (HQ). The shaded and white bars represent intracellular free radical concentrations of CeO_2 labeled $\beta\text{TC-tet}$ cells (50 and $100\ \mu\text{M}$ respectively) following identical hydroquinone exposures. Each bar is the average of three measurements and the error bars represent the standard deviation of the mean. Statistical comparisons amongst the various groups were performed using a t-test analysis and the asterisks indicate p values <0.03 . The only comparison that was not statistically (NS) significant was that between non-labeled and cells labeled with $50\ \mu\text{M}$ CeO_2 and exposed to 1 mM HQ. These data represent one of three independent experiments.

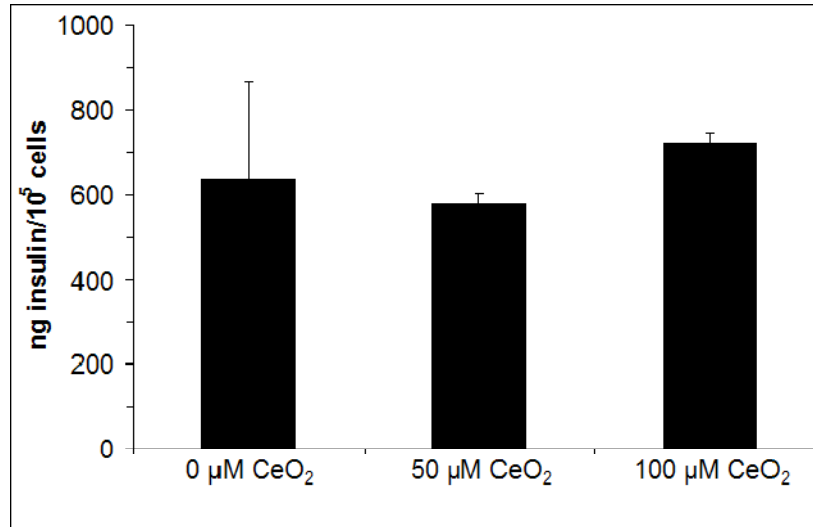


Figure 3-7. The amount of insulin secreted by non-labeled and CeO_2 labeled βTC -tet cells. Labeled cells were exposed to media containing either 50 or 100 μM CeO_2 nanoparticles for 24 hours. Each bar represents the average of two measurements and the error bars represent the standard deviation of the mean. Similar measurements were also performed with cells exposed to 50 or 100 μM CeO_2 containing media for 48 hours with identical results.

There are many potential applications in medicine that can benefit from the free radical scavenging abilities of CeO_2 nanoparticles. One such application having a potential for dramatic impact is that of islet transplantation. One of the many challenges that face islet transplantation is the loss of islet viability shortly after transplantation due to oxidative stresses induced by mechanical trauma and/or immunosuppressive medication [79]. Although several antioxidants such as Heme Oxygenase-1, SOD mimetics, vitamin C and/or E have been shown to improve oxidative stress in transplanted islets, they either degrade over a relatively short time span once incorporated into the islets, or the islets require genetic manipulation to express the desired antioxidant protein [1,79]. The proposed CeO_2 nanoparticles are a promising alternative to the existing methods because they can be delivered intracellularly and possibly targeted to specific organelles, are stable over long periods of time, do not require the genetic manipulation of cells and do not affect either the viability or insulin secretion of the host islets.

3.3 Summary

In this study, we presented novel CeO_2 nanoparticles synthesis based on a reverse micelle formation technique. The nanoparticles were crystalline, had an average particle size of 3.7 nm, and could be dispersed in medium for long periods of time due to their coating with citrate. When tested *in vitro*, the CeO_2 nanoparticles were deposited in the cytoplasm of insulin secreting cells, and the intracellular concentration of CeO_2 nanoparticles reached 0.35 pg/cell. In addition, our observation of a reduced intracellular free radical concentration was consistent with the intracellular concentration of CeO_2 nanoparticles, which is proportional to the extracellular CeO_2 concentrations. The ability of these nanoparticles to scavenge free radicals was maintained *in vivo*, providing effective protection to β TC-tet cells against an insult by the free radical generator, hydroquinone.

CHAPTER 4

SYNTHESIS OF CERIUM-ZIRCONIUM OXIDE NANOPARTICLES

This chapter introduces the preparation procedures prior to analyzing the free radical scavenging activities in $Ce_xZr_{1-x}O_2$ nanoparticles. The preparation procedures include synthesis of $Ce_xZr_{1-x}O_2$ nanoparticles using reverse micelle system, dispersion of $Ce_xZr_{1-x}O_2$ nanoparticles using buffers of multi-valent ions, and evaluating their particle size distributions in the nanosuspensions. In each preparation procedure, the background of the techniques will be described in order to provide a thorough understanding.

In order to evaluate free radical scavenging activities in $Ce_xZr_{1-x}O_2$ nanoparticles, it is important to prepare a system with narrow nanoparticle size distribution, and these nanoparticles in the particular systems should be well stabilized in a solution. The reason for doing so is to minimize the influences from the surface area that can be diminished by particle size and agglomerations. Since reverse micelle synthesis provides the system a relatively narrow nanoparticle size distribution (usually 3-10 nm), the technique was selected to synthesize $Ce_xZr_{1-x}O_2$ nanoparticles.

These synthesized $Ce_xZr_{1-x}O_2$ nanoparticles are then dispersed in a saline/tri-sodium citrate buffer. The capability for this specific buffer to disperse CeO_2 nanoparticles has been described in Chapter 2. In this buffer, tri-sodium citrate not only acts as an optimum dispersant, but the saline/tri-sodium citrate/citric acid system also stabilizes the suspension's pH value. A stable pH value is essential for the activity tests to free radical scavenging, because the fluctuating pH value can strongly influence the stability of free radicals. The particle size distribution was measured using particle size analyzer. It is to ensure the suspensions have comparable surface area and to confirm that particle agglomerations are prevented in the preparation.

Finally, the Ce/Zr ratio and the concentration of $Ce_xZr_{1-x}O_2$ nanoparticles were measured using chemical analysis methods. This procedure is also crucial, because it shows potential leaching of cerium or zirconium ions in the synthesis; and it provides precise nanoparticle concentrations for the activity tests.

4.1 Nanoparticle Synthesis

4.1.1 Reverse Micelle Synthesis

Reverse micelle method was invented as a process for preparing nanoparticles with narrow particle size distribution in the 1980's. Reverse micelles are the reversed aggregates of normal surfactant micelles. They are stabilized by the dissolution of the hydrophobic groups located outside of the reversed micelles in an apolar media in order to minimize the interfacial energy. In the reverse micelle route, each aqueous precursor is surrounded by a surfactant monolayer, and each reverse micelle works as a single nanoreactor, and has a size around 2 nm to 10 nm. The formation of nanoparticles is accomplished by diffusing a small amount of reactant, such as ammonium hydroxide, into reverse micelles. According to the electrochemical stability, nucleation and growth occur due to the increasing pH value in these nanoreactors. Therefore, nanoparticles are formed in reverse micelles. This method has been used to synthesize a variety of materials, including ceramics and polymeric nanoparticles. Several examples are: $CaCO_3$, $BaCO_3$ [80], ZrO_2 [81], CeO_2 [82], CdS [83], proteins, and enzymes [84,85].

The shape and size of the products strongly depend on the synthesis conditions. By adjusting the water/surfactant ratio to desired conditions, nanoparticles with different shapes including spherical, planar, cylindrical, discoidal, or even vesicular can be formed [86]. Also, particle sizes in the range from 1 nm to 100 nm with high crystallinity can be synthesized. The reverse micelle method increases the homogeneity of chemical composition and facilitates the preparation of nanoparticles that often have monodispersed particle size.

In order to compare the scavenging activity in our proposed system with other competitive groups, a surfactant that other groups used to synthesize CeO_2 nanoparticles was used instead of surfactant lecithin.

4.1.2 Experimental Methods

Bis(2-ethylhexyl) sulphosuccinate (AOT, laboratory grade), toluene (laboratory grade), cerium (III) nitrate hexahydrate (99.5%, M.W. = 434.22 g/mol), zirconyl(IV) nitrate hydrate (99.5%, M.W. = 231.23 g/mol), and ammonium hydroxide (NH₃ content 28~30%) were purchased from Fisher Scientific and used without further purification. One and half grams of AOT was dissolved in 100 mL of toluene to form reverse micelles. Five mini-liters of precursor solution was prepared by mixing 0.1 M cerium nitrate and 0.1 M zirconyl nitrate aqueous solutions according to the Ce/Zr ratios. The precursor solution was then pipetted into the colloidal micelle system, and the mixture was strongly stirred for 30 minutes until the system appeared homogeneous. Ten mini-liters of 1.5 M ammonium hydroxide solution was titrated into the system to initiate the precipitation. The chemicals and their amounts used in the synthesis are listed in Table 4-1.

After 45 min of stirring, $Ce_xZr_{1-x}O_2$ nanoparticles had gradually precipitated in the reverse micelles, and the appearance of the system became yellowish. The nanoparticles were collected by centrifugation with a force field of 18 G and then sequentially rinsed with 50 mL of acetone, Fifty mini-liters of ethanol, and 50 mL of water in order to remove the redundant surfactants. Between each rinses the nanoparticles were collected by centrifugation at 18 G. All samples prepared in the following chapters were synthesized or prepared at room temperature without further heat treatment. The synthesis procedure is illustrated in Figure 4-1.

Table 4-1. Chemicals and the amounts used to prepare $Ce_xZr_{1-x}O_2$ nanoparticles in reverse micelle synthesis.

Nanoparticles	Non-polar Solvent	Surfactant	Precursor Solution		Oxidizing Agent
	Toluene	AOT	Cerium Nitrate (0.1 M)	Zirconyl Nitrate (0.1 M)	Ammonium Hydroxide (1.5 M)
CeO_2	100 ml	1.5 g	5 ml	0	10 ml
$Ce_{0.8}Zr_{0.2}O_2$	100 ml	1.5 g	4 ml	1 ml	10 ml
$Ce_{0.7}Zr_{0.3}O_2$	100 ml	1.5 g	3.5 ml	1.5 ml	10 ml
$Ce_{0.6}Zr_{0.4}O_2$	100 ml	1.5 g	3 ml	2 ml	10 ml
$Ce_{0.4}Zr_{0.6}O_2$	100 ml	1.5 g	2 ml	3 ml	10 ml
$Ce_{0.2}Zr_{0.8}O_2$	100 ml	1.5 g	1 ml	4 ml	10 ml
ZrO_2	100 ml	1.5 g	0	5 ml	10 ml

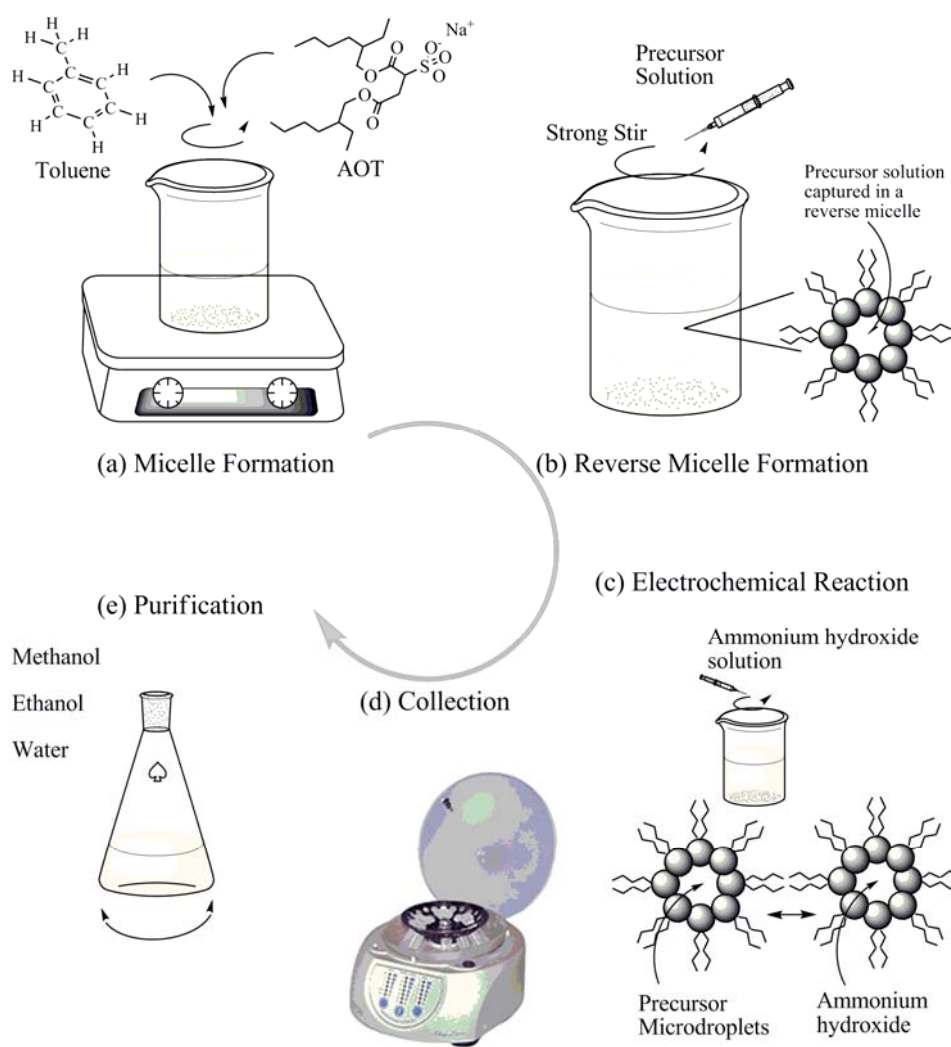


Figure 4-1. Synthesis procedures.

4.2 Nanoparticle Stabilization

4.2.1 Stabilization Using Buffer

Although the isoelectric point (IEP) of CeO_2 ranges between 6.5 to 7.5 [87,88], using sodium citrate buffer solution allows to disperse $Ce_xZr_{1-x}O_2$ nanoparticles at pH 7.4 and to retain pH stability at the same time. The optical images of CeO_2 nanoparticles stabilized in aqueous solutions are shown in Figure 4-2.

A 0.05 M saline/sodium citrate buffer (Cat. # 821840, MP Biomedical) was prepared according to the manufacturer's instructions. After the $Ce_xZr_{1-x}O_2$ nanoparticles were rinsed and collected, the products were dispersed in the sodium citrate buffer. The pH value of each sample was adjusted to 7.4 by titrating 0.1 N citric acid (97.5%, Sigma-Aldrich) or 0.1 N NaOH (Sigma-Aldrich). The suspensions were ultrasonicated overnight until the suspension changed from turbid to transparent. The suspensions were then filtered through a 0.2 μm syringe filter in order to remove unexpected agglomerates.



Figure 4-2. Optical images of CeO_2 nanoparticles dispersed in DI water (left), and in sodium citrate buffer solution solution (right).

4.3 Particle Size Analysis

4.3.1 Dynamic Light Scattering Technique

Dynamic light scattering (DLS) technique is established for measuring particle size over the size range from a few nanometers to a few microns. When light hits small particles the light scatters in all directions so long as the particles are small compared to the wavelength. If the light source is monochromatic and coherent, then a time-dependent fluctuation in the scattering intensity can be observed. These fluctuations are due to the fact that the small molecules in solutions are undergoing Brownian motion and so the distance between the scatterings in the solution is constantly changing with time. When the coherent source of light having a known frequency is directed at the moving particles, the light is scattered but at a different frequency. The shift in light frequency is related to the size of the particles causing the shift. Due to their higher average velocity, smaller particles cause a greater shift in the light frequency than larger particles. It is this difference in the frequency of the scattered light among particles of different sizes that is used to determine the sizes of the particles. Here, the size distribution of agglomeration is used to evaluate the stabilization of suspensions, since the degree of agglomerations may influence the scavenging activity of nanoparticles. The particle size distributions of the suspensions were measured by NanoTrac (MicroTrac Inc.) at PERC.

4.3.2 Agglomerate Size Distribution

Figure 4-3 shows the agglomerate size distribution in $Ce_xZr_{1-x}O_2$ suspensions measured by DLS. The mean agglomerate size M_n , D_{50} and D_{95} of all suspensions are listed in Table 4-2. The DLS results show that the $Ce_xZr_{1-x}O_2$ nanoparticles, except for ZrO_2 , are well dispersed in the sodium citrate buffer solution at pH 7.4. All the suspensions are able to sustain stabilization for more than 6 months without observable deposition.

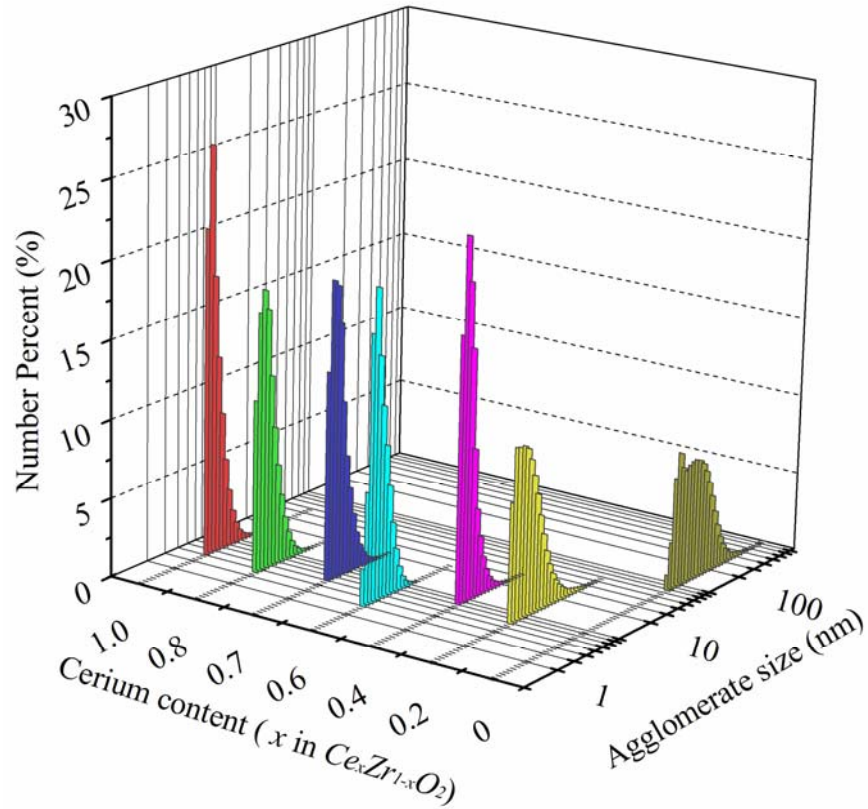


Figure 4-3. Agglomerate size distribution in $Ce_xZr_{1-x}O_2$ suspensions at pH 7.4 ($x=0, 0.2, 0.4, 0.6, 0.7, 0.8, 1.0$). The agglomerate size and number percentage of agglomeration are measured by NanoTrac.

Table 4-2. Mean agglomeration size (M_n), D_{50} , and D_{95} of $Ce_xZr_{1-x}O_2$ suspensions obtained using NanoTrac.

Suspension	D_{50} (nm)	D_{95} (nm)	M_n (nm)
CeO_2	4.6	7.0	4.9
$Ce_{0.8}Zr_{0.2}O_2$	4.2	6.7	4.6
$Ce_{0.7}Zr_{0.3}O_2$	5.8	9.2	6.3
$Ce_{0.6}Zr_{0.4}O_2$	3.9	6.0	4.2
$Ce_{0.4}Zr_{0.6}O_2$	7.9	12.0	8.5
$Ce_{0.2}Zr_{0.8}O_2$	8.2	16.4	7.2
ZrO_2	123.0	248.6	138.6

4.4 Chemical Analysis

4.4.1 Inductively Coupled Plasma Spectroscopy

The inductively coupled plasma spectroscopy (ICP) is a sophisticated spectroscopic technique for chemical analysis. The term inductively coupled plasma is a type of plasma source in which the energy is supplied by electrical currents which are produced by electromagnetic induction. The ICP system is equipped with monochromators covering the particular spectral ranges with a grating ruling, and it is operated based on the principle of atomic emission by atoms ionized in the argon plasma. Light of specific wavelengths is emitted as electrons return to the ground state of the ionized elements, quantitatively identifying the species present.

The ICP samples are prepared as ions in a solution, since the samples need to be injected through plasma and form an ionized mist. Therefore, acids and bases are usually involved in sample preparations. The system is capable of analyzing the trace concentration of materials in both organic and aqueous matrices with a detection limit range of less than 1 ppm.

The *Ce/Zr* ratios, nanoparticle concentrations in $Ce_xZr_{1-x}O_2$ suspensions were confirmed by Perkin-Elmer Plasma 3200 Inductively Coupled Plasma Spectroscopy at Particle Engineering Research Center (PERC). Sulfuric acids were used to dissolve CeO_2 , since it is reported that CeO_2 only dissolved in this particular acid. The solubility of CeO_2 was tested in several acids, i.e. sulfuric acid, hydrochloric acid, and nitric acid, prior to the concentration analysis, and it was confirmed that only sulfuric acid was able to completely dissolve CeO_2 prior to concentration measurements.

To prepare samples for ICP, an adequate amount of products was dissolved by 95% of sulfuric acid (Aldrich-Sigma) at 90°C overnight. The samples were diluted using DI water prior to use. Before measuring the cerium and zirconium concentrations in the samples, 100 ppm, 10 ppm, and 1 ppm of cerium ICP standard and zirconium ICP standard (Ricca Chemical) were

used to prepare as standard samples. The nanoparticle concentrations used in this dissertation were confirmed using ICP.

4.4.2 Compositions of Final Products

The compositions of final products are shown in Table 4-3. The compositions correspond to the designed *Ce/Zr* ratios, and the standard deviations of the compositions are between 0.00018 to 0.02 (standard deviations were obtained from 2 different suspension preparations). The ICP results suggest the fact that reverse micelle synthesis method is a remarkable method to prepare nanoparticles in laboratory scale, and the compositions of solid solutions can be controlled in fewer than 2% of deviations.

Table 4-3. Chemical compositions of final products determined.

Formula	Ce ratio	Std. deviation (Ce)	Zr ratio	Std. deviation (Zr)	Ce/Zr
<i>CeO₂</i>	0.987	0.00236	0.011	0.00825	0.99/0.01
<i>Ce_{0.8}Zr_{0.2}O₂</i>	0.819	0.00018	0.181	0.00037	0.82/0.18
<i>Ce_{0.7}Zr_{0.3}O₂</i>	0.712	0.00284	0.288	0.00569	0.71/0.19
<i>Ce_{0.6}Zr_{0.4}O₂</i>	0.633	0.00319	0.367	0.00638	0.63/0.37
<i>Ce_{0.4}Zr_{0.6}O₂</i>	0.433	0.01026	0.567	0.02052	0.43/0.57
<i>Ce_{0.2}Zr_{0.8}O₂</i>	0.218	0.00626	0.782	0.01252	0.22/0.78
<i>ZrO₂</i>	-0.00199	0.00141	1.002	0.00282	0.0/1.0

4.5 Summary

A series of *Ce_xZr_{1-x}O₂* nanoparticles using reverse micelle systems was synthesized, and the chemical compositions of cerium and zirconium (i.e. *x* and *1-x*) were precisely controlled between 0.0 to 1.0 (*x*= 0.0, 0.2, 0.4, 0.6, 0.7, 0.8, 1.0). The products were washed and collected using centrifugation. The sediments could be re-dispersed in an anticoagulation buffer, tri-sodium citrate buffer at pH 7.4. In this chapter, measuring particle sizes using NanoTrac also yields the agglomerate sizes of final products. According to the results in DLS measurements,

we concluded that the nanoparticles were well dispersed in a tri-sodium citrate buffer. The chemical compositions of the final products were confirmed using ICP, and their chemical compositions corresponded to the initial design. In this chapter, we have confirmed that $Ce_xZr_{1-x}O_2$ nanoparticles with a series of Ce/Zr ratios can be prepared in reverse micelle synthesis, and these nanoparticles can be dispersed in sodium citrate buffer. The chemical compositions of the final products correspond to the initial design.

CHAPTER 5

STRUCTURAL PROPERTIES AND NONSTOICHIOMETRIC BEHAVIOR OF CERIUM-ZIRCONIUM OXIDE NANOPARTICLES

This chapter discusses the structural properties and nonstoichiometric behavior of $Ce_xZr_{1-x}O_2$. Several characterization techniques including TEM, XRD, and Raman spectroscopy are used to confirm the crystal structures, phases, crystallite size, and crystallinity of these nanoparticles.

It is worth to note that these nanoparticles were synthesized in a designed reverse micelle system, and they were formed from hydrated cerium/zirconium salts at room temperature. Heat treatments to these nanoparticles were prevented in the synthesis. The exemption of heat treatments may cause the residual stress in the lattice, and cause mixture of several phases in each single nanoparticles. In general, the residual stress may eliminate the symmetry of structures and exclude the resolution beyond the limitation of the characterization techniques.

5.1 Characterization Techniques and Experimental Methods

5.1.1 Structural Characterization Using TEM

Transmission electron microscopy (TEM) is applied to determine the particle size, crystal structures, and partially to characterize the crystallinity of $Ce_xZr_{1-x}O_2$ nanoparticles. TEM is a technique whereby a beam of electrons is transmitted through a specimen, interacting with the specimen as it passes through it. A contrast is formed from when the transmitted electrons interact with electrons and nucleus in the specimen and the signal is magnified and focused by an objective lens and appears on an imaging screen, or is detected by a sensor such as a CCD camera.

Experimental methods

In this section, the Feret particle diameter will be measured through particle analysis in TEM images. The crystal structures of $Ce_xZr_{1-x}O_2$ nanoparticles will be evaluated by analyzing

the SAD patterns stimulated by the transmission electron beams. The crystallinity of nanoparticles will be estimated through analysis of the lattice planes/fringes of nanoparticles in TEM images.

TEM samples were prepared by re-dispersing adequate amounts of $Ce_xZr_{1-x}O_2$ nanoparticles in methanol, sonicating for 5 minutes, and dropping the suspensions on formvar carbon film supported copper grids (Electron Microscopy Sciences). A JEOL TEM 2010F TEM located at Major Analytical Instrumentation Center (MAIC, UF) was used to characterize these samples.

The particle size of each sample was determined by averaging the Feret's diameter of nanoparticle images which arbitrarily selected in TEM micrographs. The standard deviation of particle sizes was estimated around 0.5 nm, owing to the resolution of TEM micrographs.

5.1.2 Structural Characterization Using XRD

X-ray diffraction (XRD) is applied to determine the crystallite size, crystal structures of $Ce_xZr_{1-x}O_2$ nanoparticles. XRD is an x-ray technique based on the principle of scattering. The electromagnetic x-ray incidents to a specimen, and interacts with its electrons and nucleus. The contrast only appears when constructive interference occurs in the condition that the diffraction angles satisfied Bragg's Law. The diffraction pattern of a specimen reveals the characteristics of the particular material, including crystal structures, crystallite sizes, lattice parameters, etc.

Experimental methods

In this section, Scherrer's equation will be used to determine the crystallite size in the range of submicron sizes. The crystal structures of these nanoparticles will be determined by comparing their diffraction spectra with that of the corresponded crystalline materials.

All $Ce_xZr_{1-x}O_2$ nanoparticles were synthesized using reverse micelle method, washed with methanol, collected, and dried overnight. A glass slide was cleaned and covered with a double

face tape, and the dried powders were poured on the tape and evenly applied on the tape. The x-ray diffraction spectra were obtained using XRD Phillips APD 3720 at MAIC, UF.

The crystallite size of each sample was calculated using Scherrer's equation.

$$D_v = \frac{\kappa\lambda}{\beta \cos\theta} \quad (5-1)$$

where D_v is the volume weighted crystallite size, κ is Scherrer constant falls in the range of 0.87 to 1.0, λ is the wavelength of radiation, and β is the integral breadth of the reflection located at 2θ . In this study, Scherrer's constant is 0.89, and wavelength of radiation is of 1.54 angstroms [75].

5.1.3 Structural Characterization Using Raman

Raman spectroscopy is applied to determine the crystal structures, their sub-phases, and phase transformation in the series of synthesized $Ce_xZr_{1-x}O_2$ nanoparticles. Raman spectroscopy is a spectroscopic technique used in condensed matter physics and chemistry to study vibrational, rotational, and other low-frequency modes in a system. The vibration relies on inelastic scattering, or Raman scattering of monochromatic electromagnetic radiation, induced by laser light interacting with phonons or other excitations in the system, resulting in the energy of the laser photons being shifted due to the vibrational transitions in the molecules. In this dissertation, Raman spectroscopy is used to characterize the crystal structures of $Ce_xZr_{1-x}O_2$ nanoparticles. By detecting the vibrational energy induced by the symmetry of lattices, it is allowed to distinguish the crystal structures and the sub-phases of materials using Raman spectroscopy.

Experimental methods

All $Ce_xZr_{1-x}O_2$ nanoparticles were synthesized using reverse micelle methods, washed with methanol, collected, and dried overnight. Commercial 7 nm CeO_2 nanoparticles were purchased

from Nanoscale Materials Inc., USA, and commercial 40 nm CeO_2 nanoparticles were purchased from Alfa Aesar. Commercial ZrO_2 nanoparticles (tetragonal phase) were purchased from Alfa Aesar. The samples were poured on a cleaned glass slide, and tested using Renishaw Bio Raman at the Particle Engineering Research Center (PERC, UF). The excitation wavelength of incident radiation of Renishaw Bio Raman is 514 nm.

5.2 TEM Results and Discussion

Figure 5-1 to Figure 5-7 represent TEM micrographs of $Ce_xZr_{1-x}O_2$ nanoparticles ($x=0, 0.2, 0.4, 0.6, 0.7, 0.8, 1.0$) and their selective area electron diffraction (SAD) patterns. In these TEM micrographs, nanoparticles prepared in reverse micelle synthesis have particle size between 2 to 7 nm. The particle size distributions of 50 arbitrary picked particle images are recorded in Table 5-1, and their mean particle sizes are averaged and shown in the same table. The mean particle sizes of nanoparticles in our preparation are between 3.2 nm of ZrO_2 to 3.8 nm of $Ce_{0.2}Zr_{0.8}O_2$, and the standard deviation of mean particle sizes is around 0.5 nm according to the resolution of particle images.

From Figure 5-1 to Figure 5-7, we can conclude that synthesis of $Ce_xZr_{1-x}O_2$ nanoparticles using reverse micelle method is possible. Using this method, 2-7 nm of nanoparticles are prepared, and these nanoparticles remain highly crystallized even though heat treatment was exempted during preparation. In TEM images, lattice fringes are observed in the particle images, implying highly ordered crystallization in nanoparticles. Furthermore, well defined rings are observed in SAD patterns, which reconfirm the ability for this preparation method to synthesize highly crystallized $Ce_xZr_{1-x}O_2$ nanoparticles in nature.

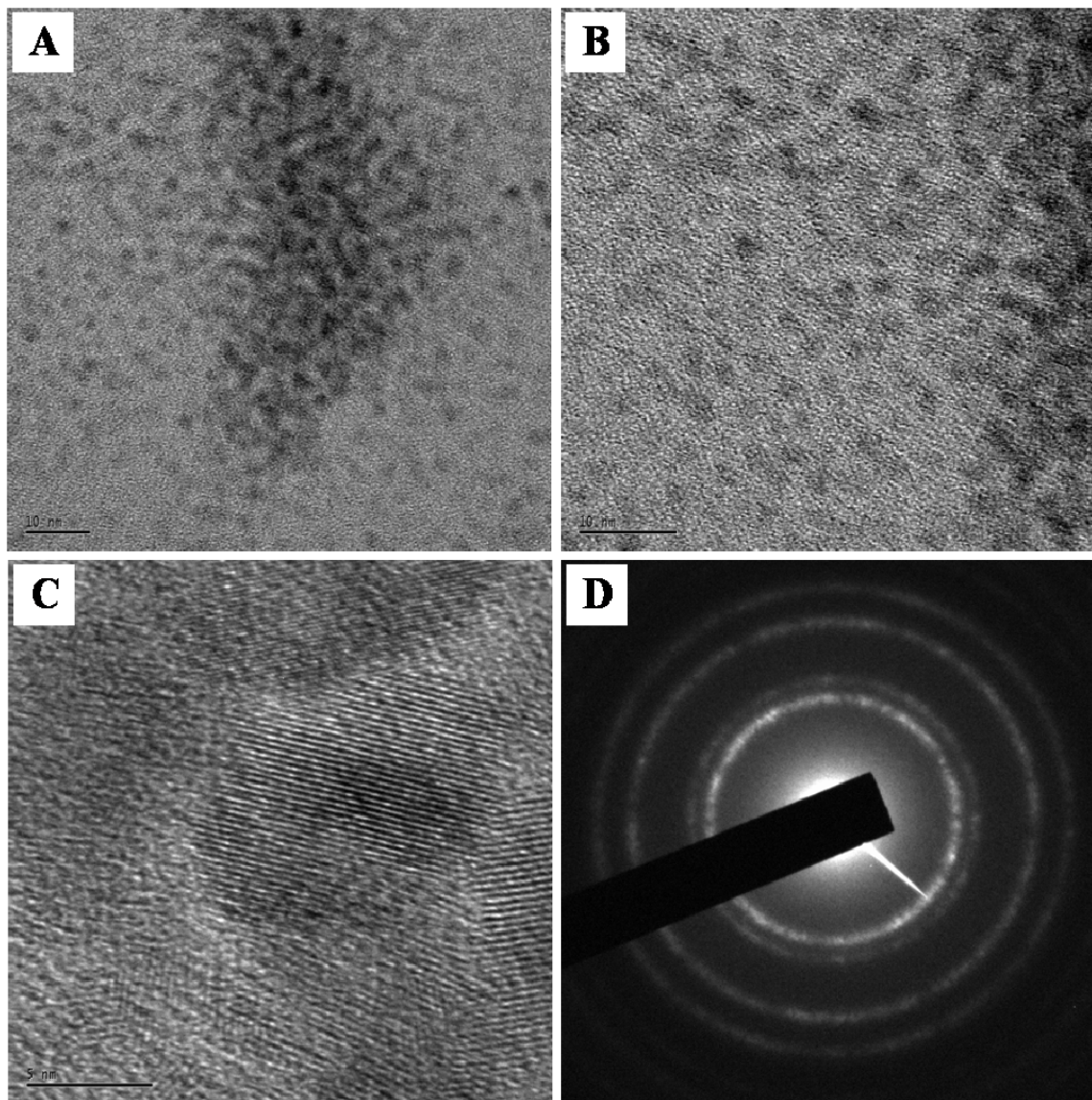


Figure 5-1. TEM micrographs of CeO_2 nanoparticles. A) Micrograph of CeO_2 nanoparticles (magnification 200 kX, scale bar 10 nm). B) Micrograph of CeO_2 nanoparticles (magnification 300 kX, scale bar 10 nm). C) Micrograph showing the lattice fringes of CeO_2 nanoparticles. The fringes imply the highly ordered crystallinity of nanoparticles (magnification 1,000 kX, scale bar 5 nm). D) SAD pattern of CeO_2 nanoparticles. The bright contrasts in the images are the accumulation of scattered electrons, therefore the ordered ring patterns indicate the polycrystalline materials detected in the TEM electron beam.

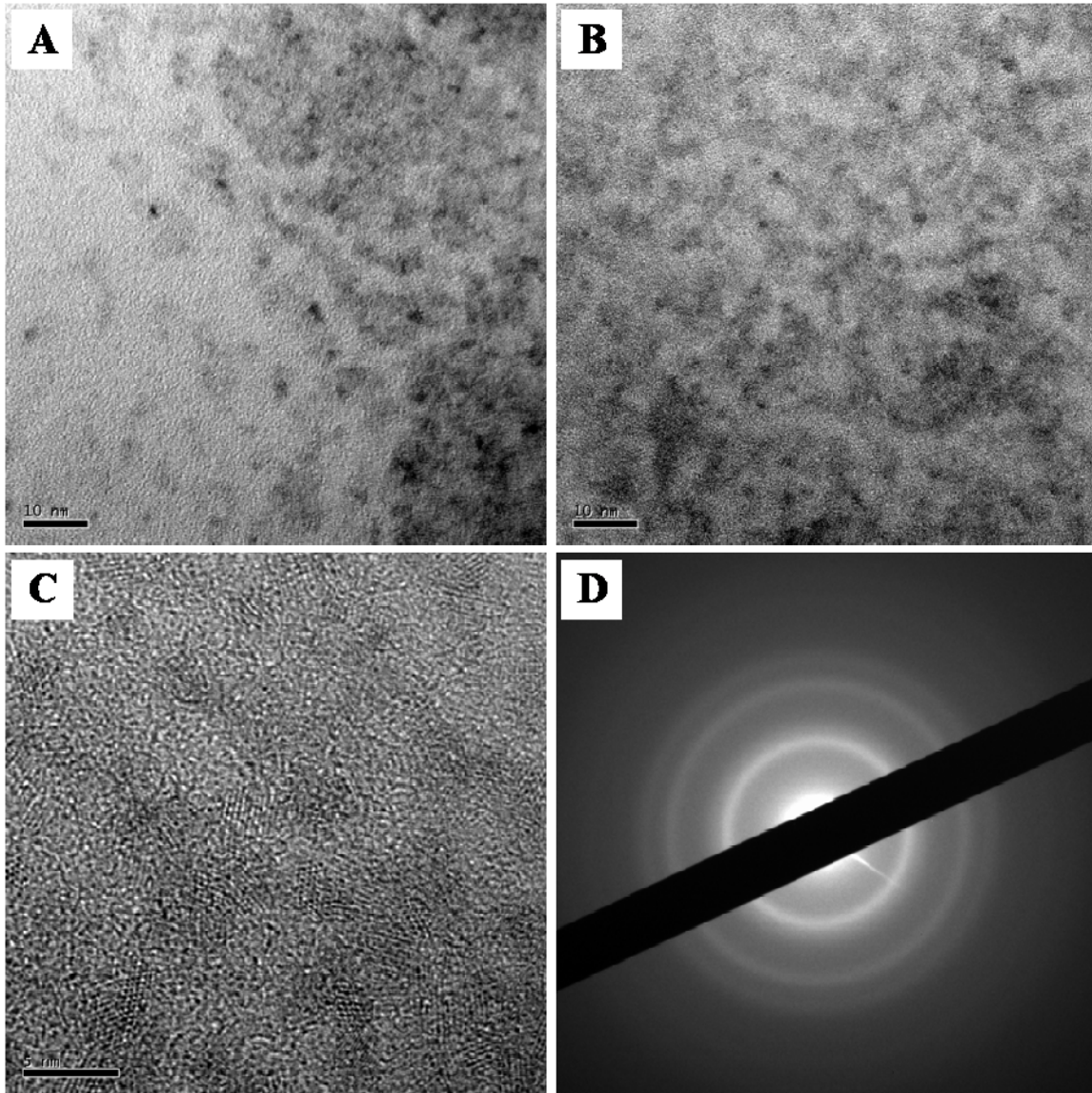


Figure 5- 2. TEM micrographs of $Ce_{0.8}Zr_{0.2}O_2$ nanoparticles. A) Micrograph of $Ce_{0.8}Zr_{0.2}O_2$ nanoparticles (magnification 200 kX, scale bar 10 nm). B) Micrograph of $Ce_{0.8}Zr_{0.2}O_2$ nanoparticles (magnification 200 kX, scale bar 10 nm). C) Micrograph showing the lattice fringes of $Ce_{0.8}Zr_{0.2}O_2$ nanoparticles. The fringes imply the highly ordered crystallinity of nanoparticles (magnification 600 kX, scale bar 5 nm). D) SAD pattern of $Ce_{0.8}Zr_{0.2}O_2$ nanoparticles. The bright contrasts in the images are the accumulation of scattered electrons, therefore the ordered ring patterns indicate the polycrystalline materials detected in the TEM electron beam.

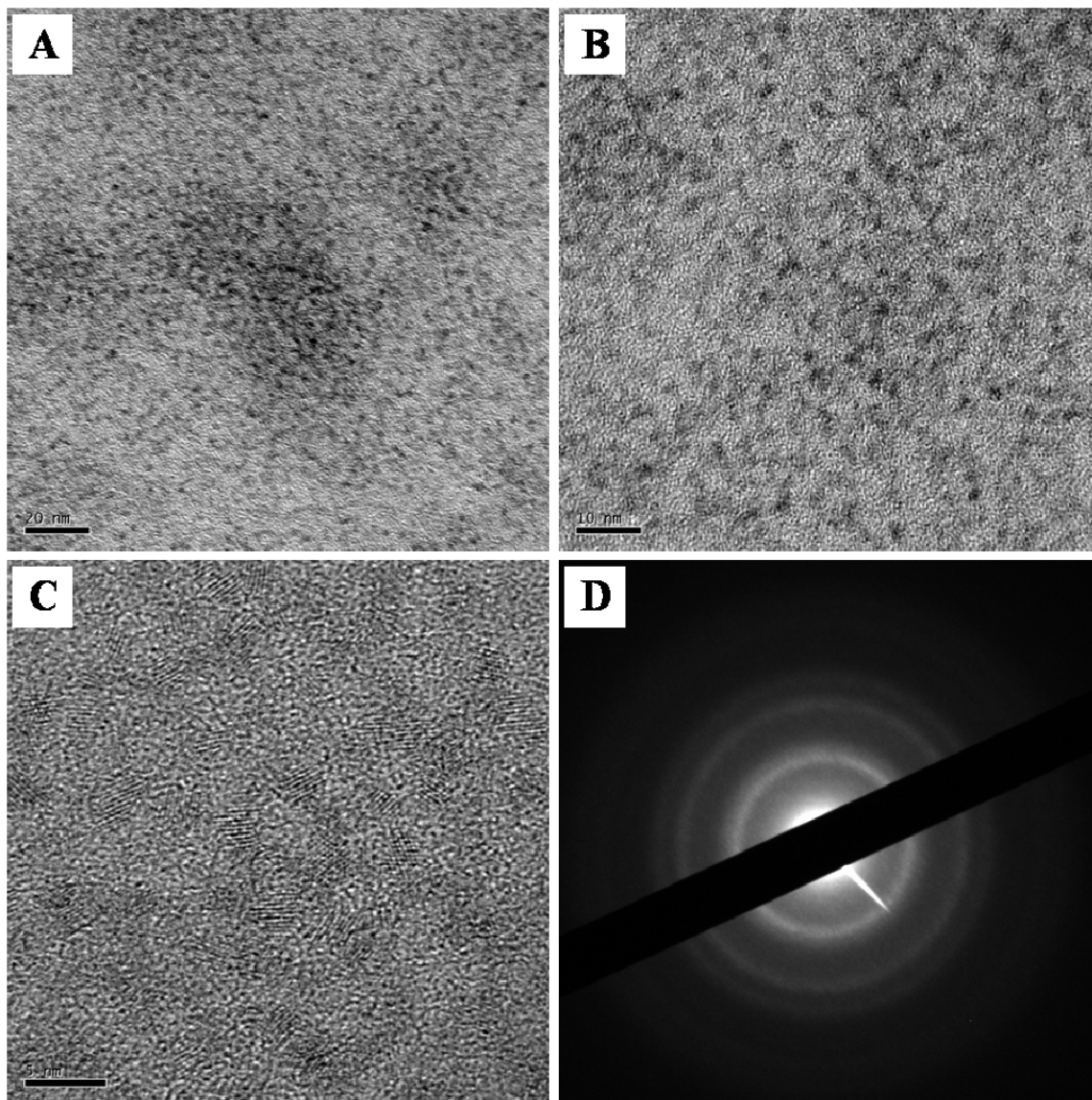


Figure 5-3. TEM micrographs of $Ce_{0.7}Zr_{0.3}O_2$ nanoparticles. A) Micrograph of $Ce_{0.7}Zr_{0.3}O_2$ nanoparticles (magnification 100 kX, scale bar 20 nm). B) Micrograph of $Ce_{0.7}Zr_{0.3}O_2$ nanoparticles (magnification 200 kX, scale bar 10 nm). C) Micrograph showing the lattice fringes of $Ce_{0.7}Zr_{0.3}O_2$ nanoparticles. The fringes imply the highly ordered crystallinity of nanoparticles (magnification 500 kX, scale bar 5 nm). D) SAD pattern of $Ce_{0.7}Zr_{0.3}O_2$ nanoparticles. The bright contrasts in the images are the accumulation of scattered electrons, therefore the ordered ring patterns indicate the polycrystalline materials detected in the TEM electron beam.

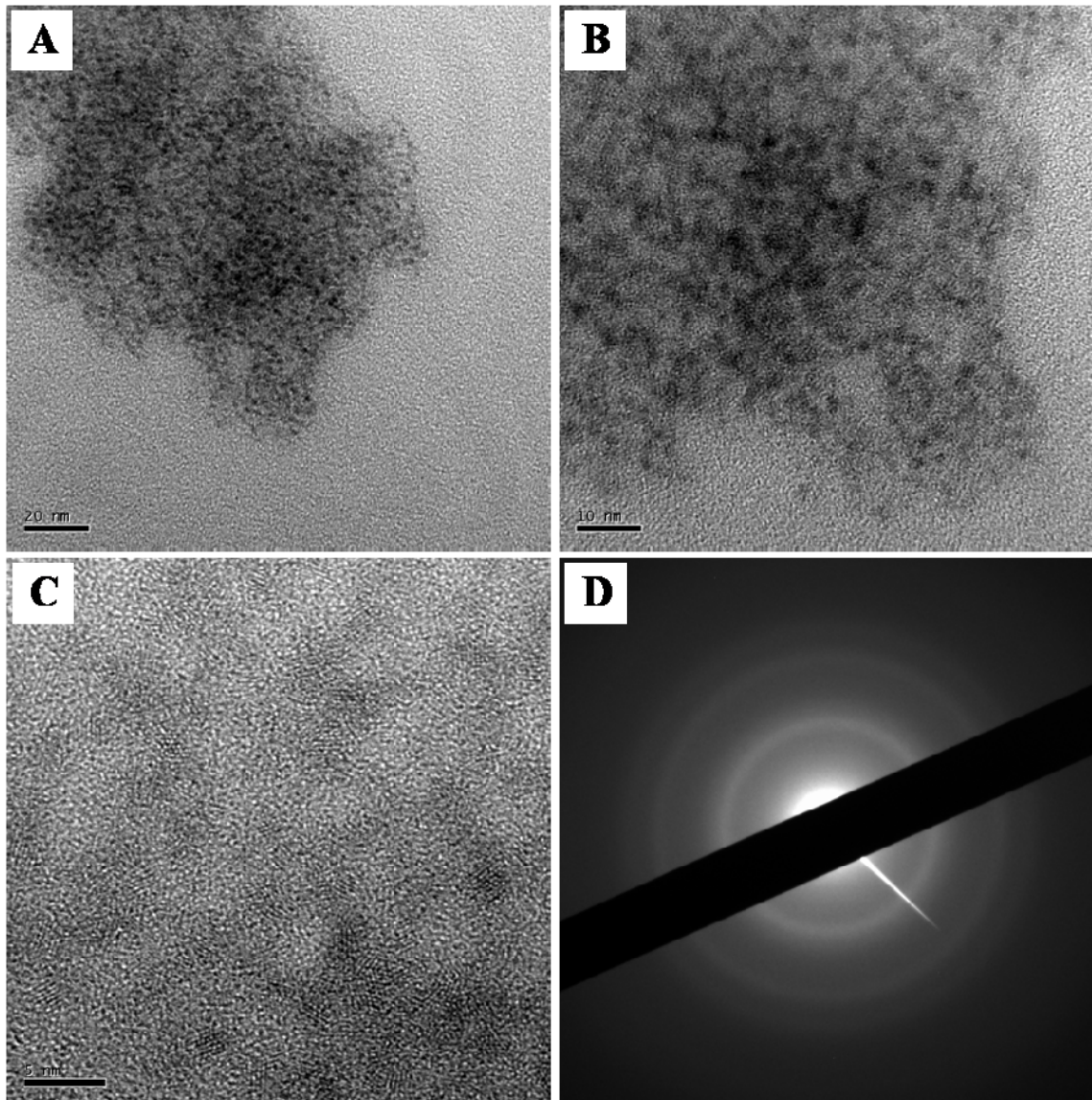


Figure 5-4. TEM micrographs of $Ce_{0.6}Zr_{0.4}O_2$ nanoparticles. A) Micrograph of $Ce_{0.6}Zr_{0.4}O_2$ nanoparticles (magnification 100 kX, scale bar 20 nm). B) Micrograph of $Ce_{0.6}Zr_{0.4}O_2$ nanoparticles (magnification 200 kX, scale bar 10 nm). C) Micrograph showing the lattice fringes of $Ce_{0.6}Zr_{0.4}O_2$ nanoparticles. The fringes imply the highly ordered crystallinity of nanoparticles (magnification 500 kX, scale bar 5 nm). D) SAD pattern of $Ce_{0.6}Zr_{0.4}O_2$ nanoparticles. The bright contrasts in the images are the accumulation of scattered electrons, therefore the ordered ring patterns indicate the polycrystalline materials detected in the TEM electron beam.

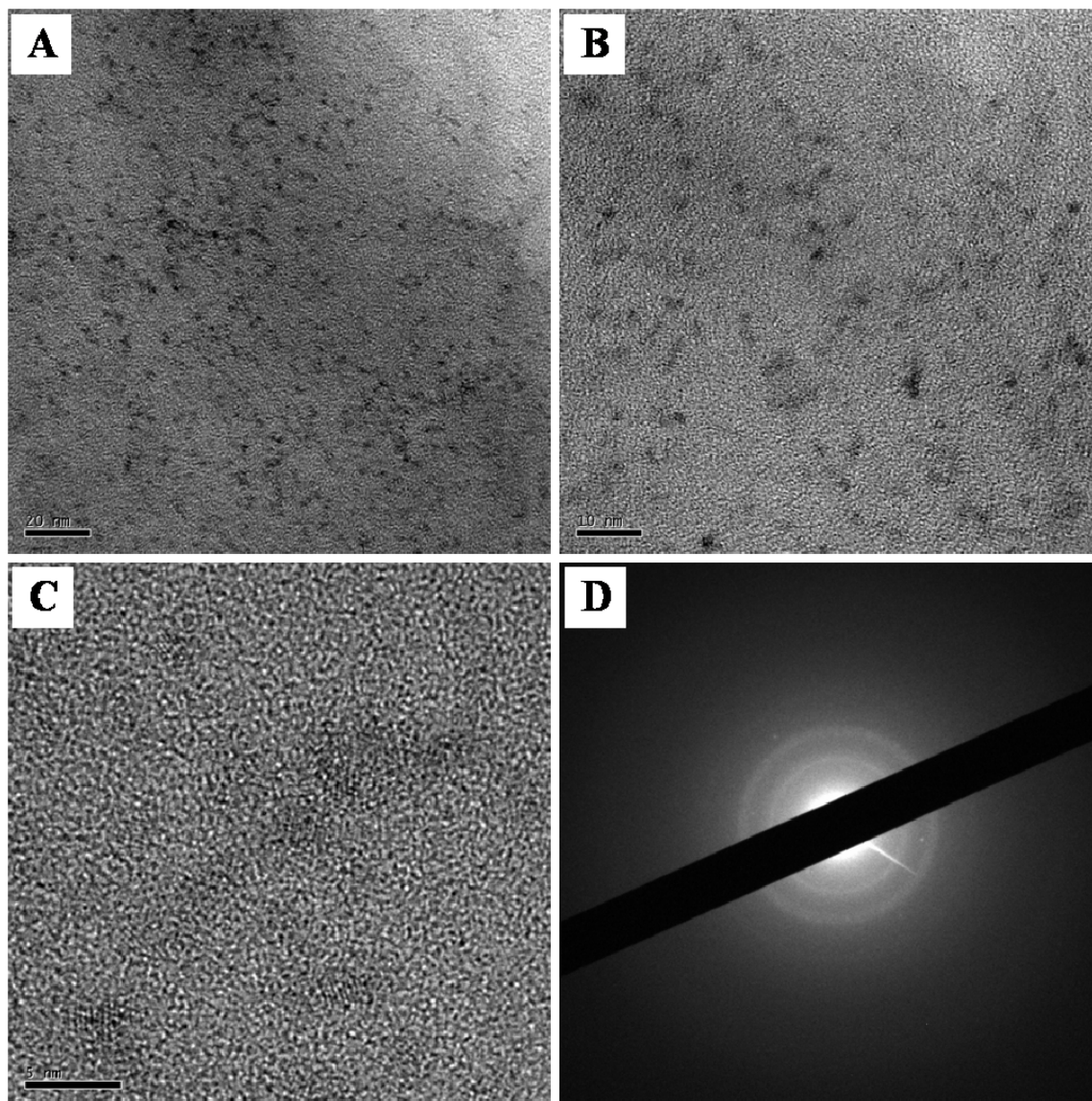


Figure 5-5. TEM micrographs of $Ce_{0.4}Zr_{0.6}O_2$ nanoparticles. A) Micrograph of $Ce_{0.4}Zr_{0.6}O_2$ nanoparticles (magnification 100 kX, scale bar 20 nm). B) Micrograph of $Ce_{0.4}Zr_{0.6}O_2$ nanoparticles (magnification 200 kX, scale bar 10 nm). C) Micrograph showing the lattice fringes of $Ce_{0.4}Zr_{0.6}O_2$ nanoparticles. The fringes imply the highly ordered crystallinity of nanoparticles (magnification 600 kX, scale bar 5 nm). D) SAD pattern of $Ce_{0.4}Zr_{0.6}O_2$ nanoparticles. The bright contrasts in the images are the accumulation of scattered electrons, therefore the ordered ring patterns indicate the polycrystalline materials detected in the TEM electron beam.

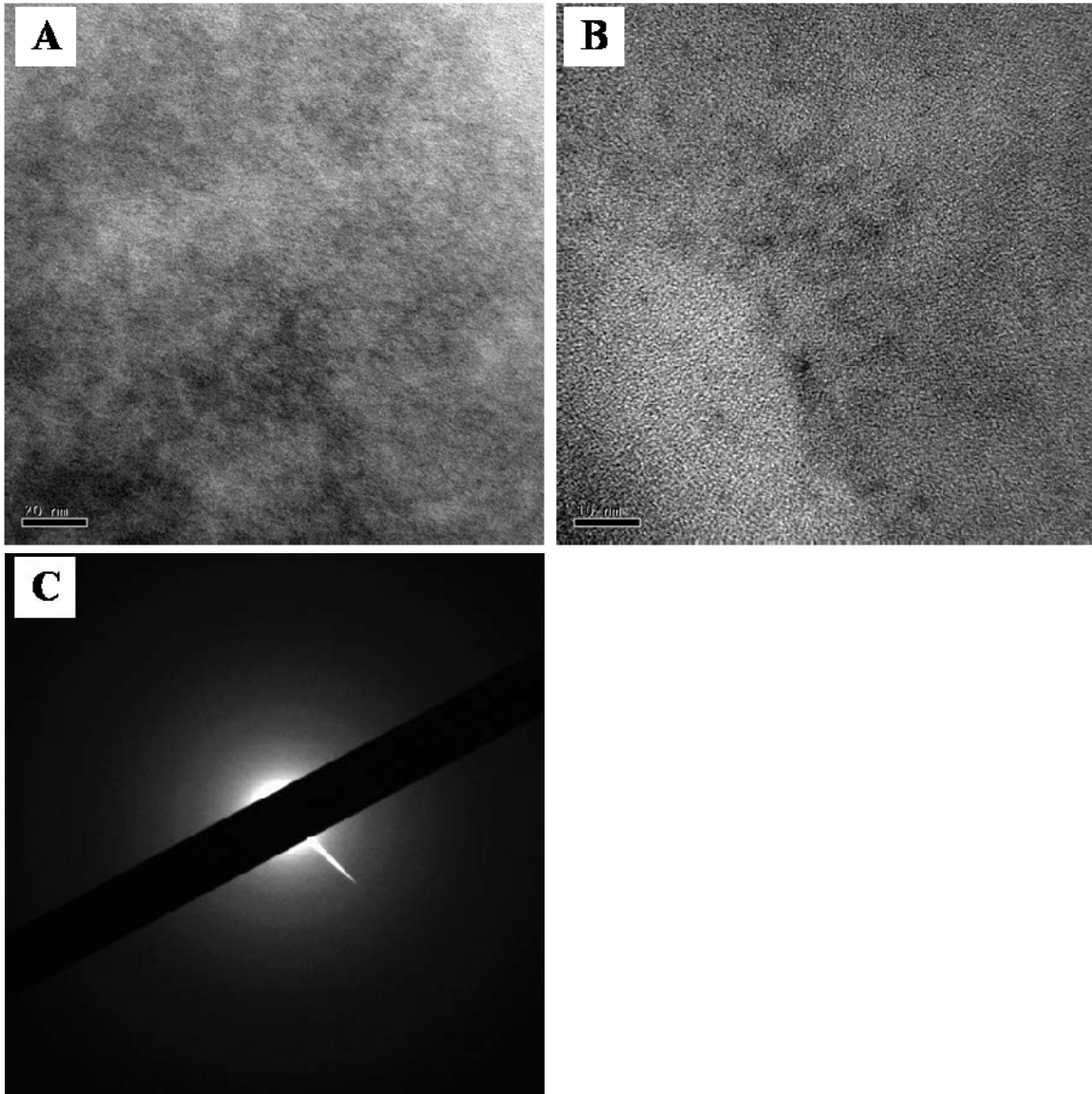


Figure 5-6. TEM micrographs of $Ce_{0.2}Zr_{0.8}O_2$ nanoparticles. A) Micrograph of $Ce_{0.2}Zr_{0.8}O_2$ nanoparticles (magnification 100 kX, scale bar 20 nm). B) Micrograph of $Ce_{0.2}Zr_{0.8}O_2$ nanoparticles (magnification 200 kX, scale bar 10 nm). C) SAD pattern of $Ce_{0.2}Zr_{0.8}O_2$ nanoparticles. The bright contrasts in the images are the accumulation of scattered electrons. The contrast of the ring is not strong due to the residual surfactants on particle surface.

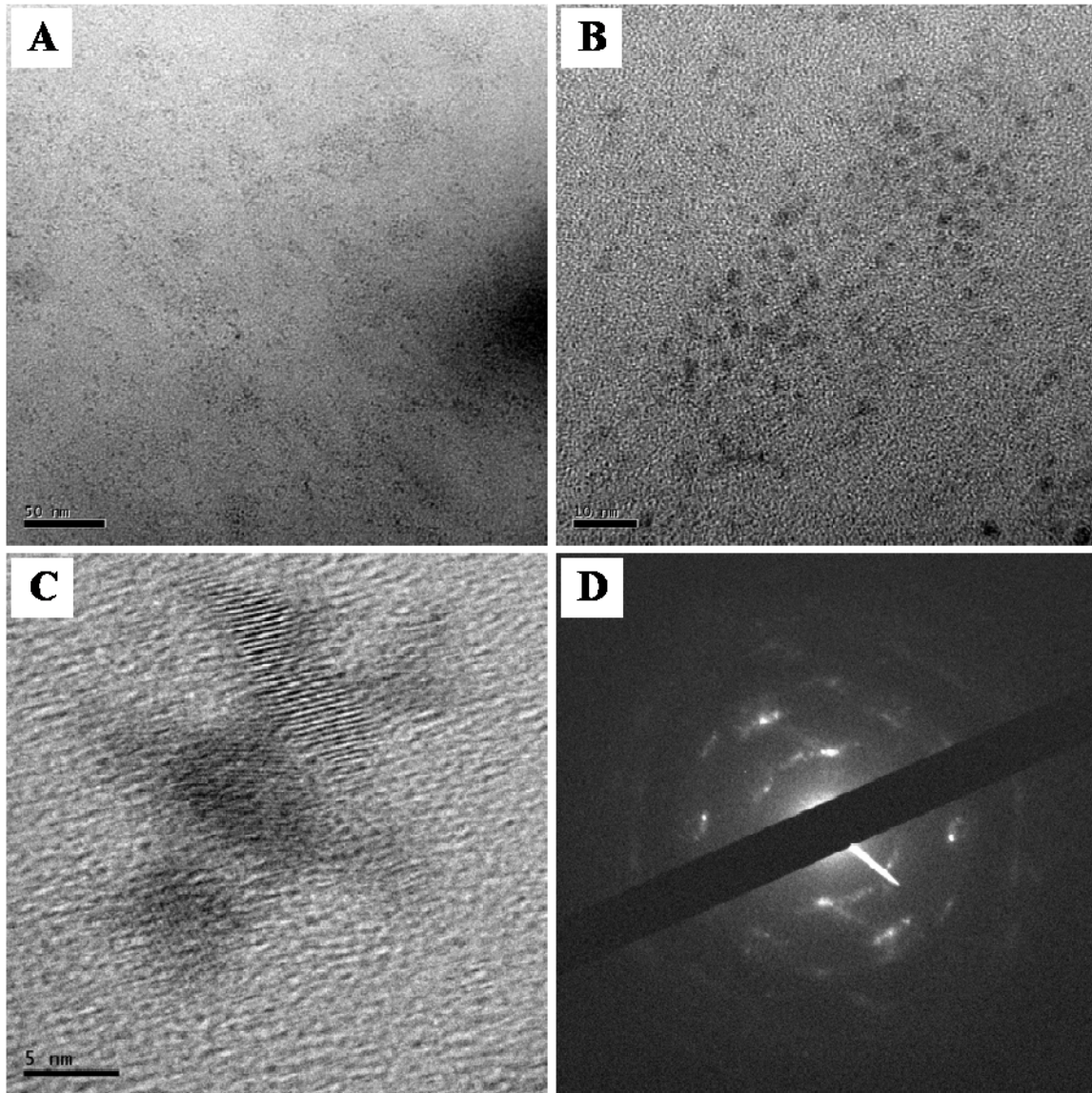


Figure 5-7. TEM micrographs of ZrO_2 nanoparticles. A) Micrograph of ZrO_2 nanoparticles (magnification 50 kX, scale bar 50 nm). B) Micrograph of ZrO_2 nanoparticles (magnification 200 kX, scale bar 10 nm). C) Micrograph showing the lattice fringes of ZrO_2 nanoparticles. The fringes imply the highly ordered crystallinity of nanoparticles (magnification 600 kX, scale bar 5 nm). D) SAD pattern of ZrO_2 nanoparticles. The bright contrasts in the images are the accumulation of scattered electrons, therefore the ordered ring patterns indicate the polycrystalline materials detected in the TEM electron beam.

Table 5-1. Particle sizes of $Ce_xZr_{1-x}O_2$ nanoparticles averaged from 50 arbitrary selected particles in TEM micrographs.

Samples	Feret Diameter* (nm) *largest dimension of each particle								Mean Particle Size (nm)
	1-2	2-3	3-4	4-5	5-6	6-7	7-8	>8	
CeO_2	0(BA)	10	14	22	3	1	0	0	3.7
$Ce_{0.8}Zr_{0.2}O_2$	0	11	27	10	2	0	0	0	3.6
$Ce_{0.7}Zr_{0.3}O_2$	1	18	22	9	0	0	0	0	3.3
$Ce_{0.6}Zr_{0.4}O_2$	3	11	26	10	0	0	0	0	3.4
$Ce_{0.4}Zr_{0.6}O_2$	0	18	22	6	3	0	1	0	3.5
$Ce_{0.2}Zr_{0.8}O_2$	0	1	6	2	1	0	0	0	3.8 [§]
ZrO_2	1	23	19	6	1	0	0	0	3.2

[§]The mean particle size of $Ce_{0.2}Zr_{0.8}O_2$ was measured from 10 arbitrary selected particle images due to the limited resolution in TEM micrographs.

5.3 XRD Results and Discussion

Figure 5-8 shows the XRD spectra of synthesized $Ce_xZr_{1-x}O_2$ nanoparticles ($x = 0, 0.2, 0.4, 0.6, 0.7, 0.8, 1.0$). In Figure 5-8, each individual peak in the XRD spectrum of CeO_2 nanoparticles fit to the corresponded XRD spectra of crystalline CeO_2 . The peaks (111) in CeO_2 , $Ce_{0.8}Zr_{0.2}O_2$, $Ce_{0.7}Zr_{0.3}O_2$, and $Ce_{0.6}Zr_{0.4}O_2$ slightly shift to a higher diffraction angle, which is a result of lattice expansion. The shift of peaks (111) corresponds to the reported spectra, and is an evidence of solid solutions throughout the nanoparticles. The tetragonal feature appears in the XRD spectrum of CeO_2 , $Ce_{0.8}Zr_{0.2}O_2$, $Ce_{0.7}Zr_{0.3}O_2$, and $Ce_{0.6}Zr_{0.4}O_2$ nanoparticles, which is a feature of phase transformation from cubic to tetragonal crystal structure. From XRD spectra, we conclude that CeO_2 , $Ce_{0.8}Zr_{0.2}O_2$, $Ce_{0.7}Zr_{0.3}O_2$, $Ce_{0.6}Zr_{0.4}O_2$ nanoparticles have cubic fluorite structure, and the phase transformation occurred when more than 40% of zirconium ions doped in the solid solution. The results correspond to crystal structures as well as phase transformation of $Ce_xZr_{1-x}O_2$ nanoparticles ($x = 0.6-1.0$) reported by Zhang et al. [75]. However, the XRD

spectra of $Ce_xZr_{1-x}O_2$ nanoparticles with more than 60% of zirconium dopants do not correspond to the results reported in the other literatures [36,75]. In the nanoparticles synthesized in our laboratory, the broadened XRD spectra of $Ce_{0.4}Zr_{0.6}O_2$, $Ce_{0.2}Zr_{0.8}O_2$, and ZrO_2 nanoparticles show mixed crystal structures in these nanoparticles. The position of the two major peaks matches the reported XRD spectra of cubic fluorite, tetragonal and monoclinic crystal structures. Thus, we assume that $Ce_{0.4}Zr_{0.6}O_2$, $Ce_{0.2}Zr_{0.8}O_2$, and ZrO_2 nanoparticles are mixtures of cubic, tetragonal, and monoclinic structures.

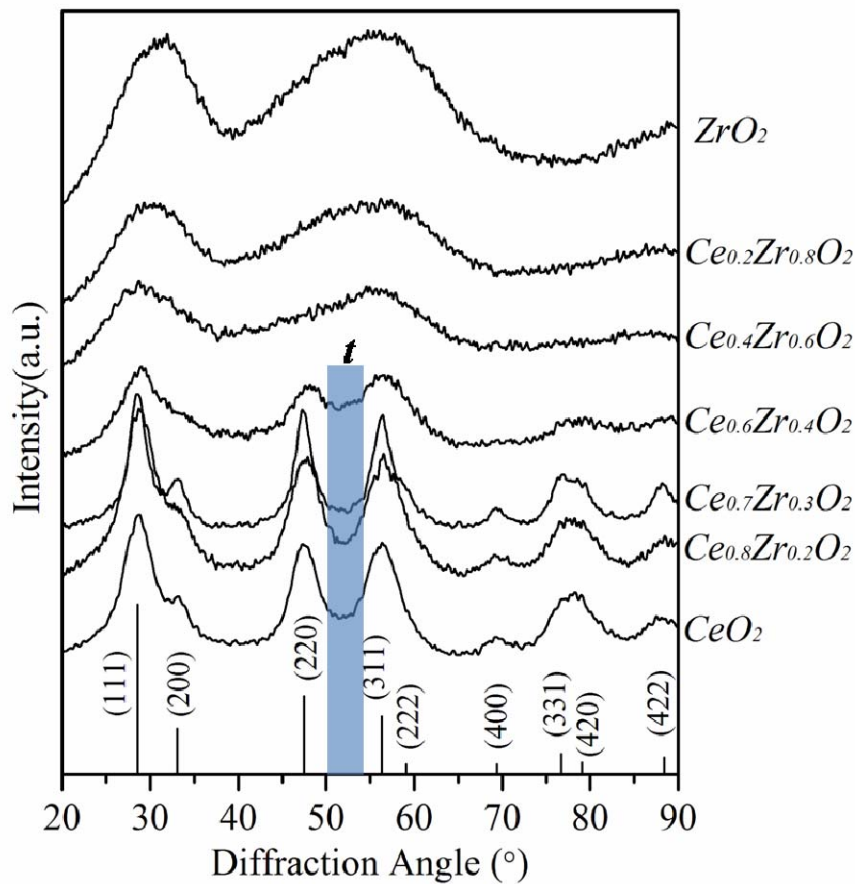


Figure 5-8. XRD spectra of a series of $Ce_xZr_{1-x}O_2$ nanoparticles ($x=0, 0.2, 0.4, 0.6, 0.7, 0.8, 1.0$). The XRD spectrum of CeO_2 crystalline is plugged in the bottom to show the correspondence of XRD between synthesized CeO_2 and reference data. The tetragonal feature (t) appears and increases when more zirconium doped into the solid solutions, indicating phase transformation in the series of nanoparticles.

The crystallite size of CeO_2 nanoparticles is determined by XRD spectra associated with Scherrer's equation, and the crystallite size is calculated to be 3.7 ± 0.2 nm by averaging the values obtained from XRD peaks (111), (200), (220). The crystallite size corresponds to particle size determined by TEM micrographs, and the results implied that each nanoparticle is of a single crystallite. Accordingly, the crystallite sizes of $Ce_{0.8}Zr_{0.2}O_2$ and $Ce_{0.7}Zr_{0.3}O_2$ nanoparticles that obtained from their XRD peaks (111), (200), (220) are 2.0 ± 0.07 nm and 3.4 ± 0.2 nm, respectively. However, the $Ce_{0.6}Zr_{0.4}O_2$, $Ce_{0.4}Zr_{0.6}O_2$, $Ce_{0.2}Zr_{0.8}O_2$, and ZrO_2 nanoparticles have broadened XRD spectra, therefore Scherrer's equation is not suitable to calculate the crystallite sizes of these samples.

5.4 Raman Results and Discussion

To identify the phases in $Ce_xZr_{1-x}O_2$, there are six distinct Raman shifts being used. The shift of each peak may be unique in the samples that prepared in different synthesis methods, heat treatment, or particle size, therefore, we adopted the wave numbers in Raman spectra that reported by Zhang et al. [75] in this dissertation. Figure 2-6(b) is the Raman spectra of $Ce_xZr_{1-x}O_2$ solid solutions adopted from Zhang's work. The numbers in the figure represent the features for identifying c , t , t' , or t'' phases. In order to simplify the classification, the indications of each peak are listed in

Table 5-2, where peak 4 is a strong peak pointing toward the main cubic structure; peaks 1-3 represent the tetragonal distortion in the lattice; peaks 5, 6 contributed by defects and oxygen displacements that distort the cubic structure. Briefly, by identifying the intensity of Raman shift peak 4 and peaks 1-3, it is possible to identify metastable t'' phase in cubic fluorite structure and phase transformation from cubic to tetragonal structure in $Ce_xZr_{1-x}O_2$ nanoparticles.

Table 5-2. Crystal structures and their sub-phases in $Ce_xZr_{1-x}O_2$, and the classification using Raman spectroscopy.

Phase	Crystal System	Stable or Metastable	Axial Ratio (c/a)	Oxygen Displacement	Identifying Peaks
<i>c</i>	Cubic	Stable	1	None	4 and 4 only
<i>t''</i>	Cubic	Metastable	1	Existing	1, 2, 3, and 4
<i>t'</i>	Tetragonal	Metastable	>1	Existing	1-6 and weak 4
<i>t</i>	Tetragonal	Stable	>1	Existing	1-6 and weak 4

Figure 5-9 shows Raman spectra of commercial 7 nm, 40 nm CeO_2 nanoparticles, and a series of synthesized $Ce_xZr_{1-x}O_2$ nanoparticles. Due to instrumental limitation, the Raman shifts in this work was detected down to 200 cm^{-1} .

The Raman spectra of commercial 7 nm, 40 nm, and synthesized CeO_2 nanoparticles are shown in Figure 5-9(a). According to their Raman spectra, commercial CeO_2 nanoparticles and synthesized CeO_2 nanoparticles have a very strong peak 4, so their crystal structures are based on cubic fluorite structure. In the Raman spectra of synthesized CeO_2 nanoparticles peaks 3, 5, and 6 are noted, so *t''* phase also exists in the system. This is the result of lattice distortion, due to the residual lattice stress formed in the synthesis, in which the exemption of heat treatment caused the phenomenon.

From Figure 5-9(a) to (d), peak 4 in Raman spectra was observed, although the intensity of peak 4 decreases with increasing zirconium dopants. The results suggest, first, samples CeO_2 , $Ce_{0.8}Zr_{0.2}O_2$, $Ce_{0.7}Zr_{0.3}O_2$, and $Ce_{0.6}Zr_{0.4}O_2$ have cubic structure. Second, the cubic structure in these samples was distorted by zirconium dopants, while the cubic feature (peak 4) gradually diminished with increasing zirconium dopants. Meanwhile, peaks 3, 5, and 6 remain constant in these samples, indicating greater portion of *t''* phase appearing in the cubic based structure when more zirconium ions were doped into the solid solution. In general, *t''* phase is a metastable

phase in cubic structure, and the axial ratio of its lattice structure equals to one. In conclusion, CeO_2 , $Ce_{0.8}Zr_{0.2}O_2$, $Ce_{0.7}Zr_{0.3}O_2$, and $Ce_{0.6}Zr_{0.4}O_2$ have cubic structures, and the ratio of metastable cubic phase (t'') increases when more and more zirconium doped in the crystal structure. Comparing to the characterization of the same materials that were conducted by Zhang et al., it is noted that the metastable t'' phase appears in the undoped CeO_2 nanoparticles. The early appearing t'' phase conflicts the results reported by Zhang et al. [78]. It is believed that the metastable t'' phase in $CexZr_{1-x}O_2$ nanoparticles with lower zirconium dopants is a result of lattice distortion. Due to the lack of heat treatment, the residual stress in $CexZr_{1-x}O_2$ nanoparticles may cause lattice distortion.

In Figure 5-9(e), peak 4 disappears while peaks 3, 5, 6 remain sound in the Raman spectra. The vanished peak 4 is a sign of phase transition from cubic to tetragonal. At this state, the axial ratio of crystal structure in samples $Ce_{0.4}Zr_{0.6}O_2$ becomes greater than one and its crystal lattice no longer belongs to cubic but rectangular. From Figure 5-9(e) to (g), none or weak peak 4 was observed in the Raman spectra, and peaks 3, 5, 6 remain constant while more and more zirconium dopants in the materials. Furthermore, peak 2 arises while more than 80% of zirconium ions doped in the lattice. Perhaps, the rising peak 2 represents phase transition from metastable t' to t phase. In conclusion, the results suggest that $Ce_{0.4}Zr_{0.6}O_2$, $Ce_{0.2}Zr_{0.8}O_2$, and ZrO_2 nanoparticles are no longer in cubic structure. Instead, they are tetragonal in structure, and their axial ratio of lattice is greater than one.

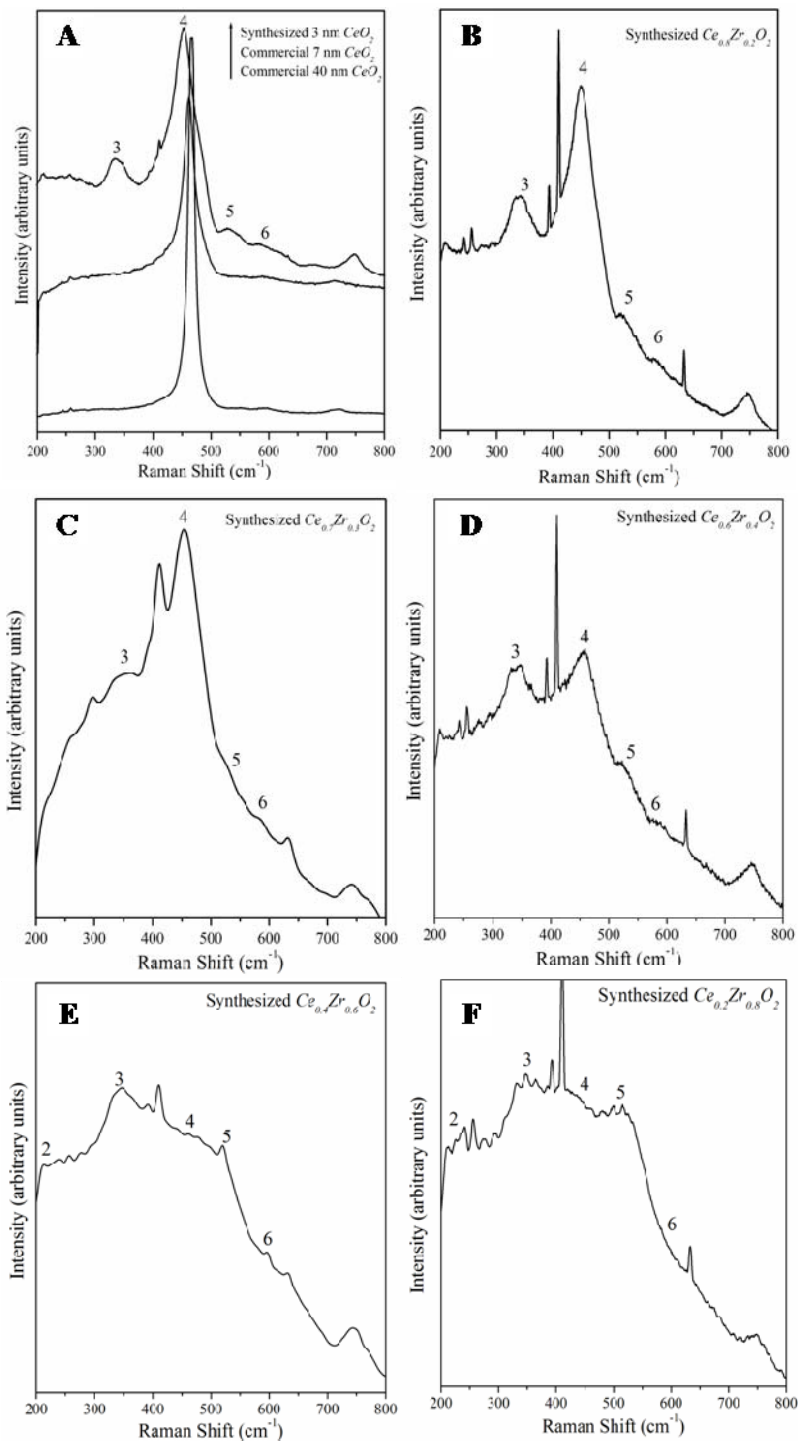


Figure 5-9. Raman spectra of $Ce_xZr_{1-x}O_2$ nanoparticles. A) commercial 7 nm CeO_2 , 40 nm CeO_2 , and synthesized CeO_2 nanoparticles. B) $Ce_{0.8}Zr_{0.2}O_2$. C) $Ce_{0.7}Zr_{0.3}O_2$. D) $Ce_{0.6}Zr_{0.4}O_2$. E) $Ce_{0.4}Zr_{0.6}O_2$. F) $Ce_{0.2}Zr_{0.8}O_2$. G) synthesized ZrO_2 . H) commercial ZrO_2 nanoparticles (shown in the following page). The numbers marked in the spectra were defined in previous paragraph.

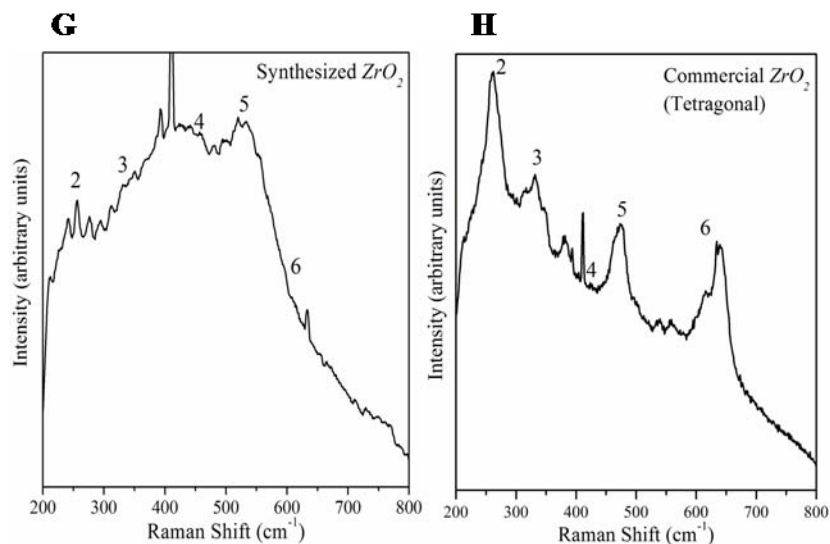


Figure 5-9. Continued.

5.5 Summary of TEM, XRD, Raman Results

5.5.1 Crystalline $Ce_xZr_{1-x}O_2$ Nanoparticles with Homogeneous Particle Size

From the lattice fringes, diffraction patterns in TEM images, and defined peaks in XRD spectra, it can be concluded that $Ce_xZr_{1-x}O_2$ nanoparticles prepared by reverse micelle synthesis method are crystalline in nature. In addition, the defined Raman shifts in $Ce_xZr_{1-x}O_2$ nanoparticles support the conclusion that these $Ce_xZr_{1-x}O_2$ nanoparticles are crystalline in nature. Although other studies have shown that $Ce_xZr_{1-x}O_2$ nanoparticles precipitated in other reverse micelle systems were amorphous and heat treatments were preferred, we have been able to perform an improved, more confined reverse micelles system that allows improving crystallinity of the final products. Observed in TEM, all samples synthesized in the particular reverse micelle system are homogeneous in size, and their particle sizes are around 3-7 nm in diameters.

5.5.2 Phase Transition Detected by XRD and Raman Spectroscopy

In this work, the information obtained using XRD and Raman spectroscopy has provided credible conclusions in terms of crystal structures as well as sub-structures of the lattice. Using

XRD, it is found that CeO_2 , $Ce_{0.8}Zr_{0.2}O_2$, $Ce_{0.7}Zr_{0.3}O_2$, and $Ce_{0.6}Zr_{0.4}O_2$ nanoparticles have cubic fluorite structure, while $Ce_{0.4}Zr_{0.6}O_2$, $Ce_{0.2}Zr_{0.8}O_2$, and ZrO_2 nanoparticles have complex structures which mixed with cubic fluorite, tetragonal, and monoclinic structures. Perhaps the mixed crystal structures in $Ce_{0.4}Zr_{0.6}O_2$, $Ce_{0.2}Zr_{0.8}O_2$, and ZrO_2 nanoparticles are a result of residual stress in the lattice due to exempted heat treatment. Using Raman spectroscopy, the phase transformation from cubic to tetragonal was found when more than 60% of cerium ions were replaced with zirconium dopants. In addition, it is found that the more metastable cubic phase t'' were formed when the concentration of zirconium dopants increased in the lattice. The portion of t'' phase finally no longer sustained in cubic structure, so the metastable t'' phase finally transformed to tetragonal structure. The crystal structure as well of its sub-structure of $Ce_xZr_{1-x}O_2$ nanoparticles can be identified using XRD associated with Raman spectroscopy. In addition, the phase transformation, sub-phases in $Ce_xZr_{1-x}O_2$ nanoparticles can be detected by comparing the shifted peaks of Raman spectra.

CHAPTER 6

FREE RADICAL SCAVENGING BY CERIUM-ZIRCONIUM OXIDE NANOPARTICLES

It is hypothesized that free radical scavenging in CeO_2 nanoparticles is a consequence of catalysis, and the scavenging activity of CeO_2 nanoparticles can be improved structurally by doping zirconium into lattice. To demonstrate our hypothesis is correct, the scavenging activities of $Ce_xZr_{1-x}O_2$ nanoparticles shall be tested and the obtained activities will be used to compare the reported OSC in the same materials. By doing so, it may help to understand the scavenging mechanism carried out by $Ce_xZr_{1-x}O_2$ nanoparticles. In addition, the scavenging mechanism of these nanoparticles can be promoted further, according to the obtained knowledge.

In this chapter, two of ROS, hydrogen peroxide and superoxide radicals, will be used to probe the scavenging activities of $Ce_xZr_{1-x}O_2$ nanoparticles. It is because these two oxygen species are very influential ROS in biological systems, and do play essential roles in cell metabolism as well as apoptosis. To successfully test nanoparticle's scavenging activities, several innovative methodologies are applied in this dissertation. These innovative methodologies are assays that based on biochemical reactions, and these assays are the first time used to evaluate a metal oxide catalyst's activity at room temperature. At the end of this chapter, the free radical scavenging activities of $Ce_xZr_{1-x}O_2$ nanoparticles as well as the scavenging mechanism will be discussed based on the structural properties of $Ce_xZr_{1-x}O_2$ nanoparticles.

6.1 Prospective Scavenging Activities in $Ce_xZr_{1-x}O_2$ Nanoparticles

As aforementioned, free radical scavenging mechanism carried out by $Ce_xZr_{1-x}O_2$ nanoparticles is a result of surface oxygen exchange. Based on the hypothetic mechanism proposed in Figure 2-2, there are two prerequisites in the scavenging. First is that the transition of oxygen species only occur when mobile electrons available in the lattice. Second is that the exchange only occur when oxygen vacancies present in the lattice. According to the

understanding, a model that is available to describe free radical scavenging by $Ce_xZr_{1-x}O_2$ nanoparticles is illustrated in Figure 6-1.

Since the available mobile electrons can be provided by oxygen vacancies in the lattice, the scavenging activities of $Ce_xZr_{1-x}O_2$ nanoparticles likely are limited by the concentration of oxygen vacancies in the lattice. The concentration of oxygen vacancies in CeO_2 -based materials is reported to be proportional to their OSC. Therefore, we can presume that free radical scavenging activities of $Ce_xZr_{1-x}O_2$ nanoparticles follow the level of OSC in the same materials. Fortunately, OSC of $Ce_xZr_{1-x}O_2$ have been reported, and Figure 6-2 is reproduced from the paper published by Descorme et al. [62]. Since the catalytic activity of CeO_2 nanoparticles can be promoted up to four times by incorporating 20-40 % of zirconium dopants, it is prospecting to have four times of greater scavenging activities in $Ce_xZr_{1-x}O_2$ nanoparticles than in undoped CeO_2 nanoparticles.

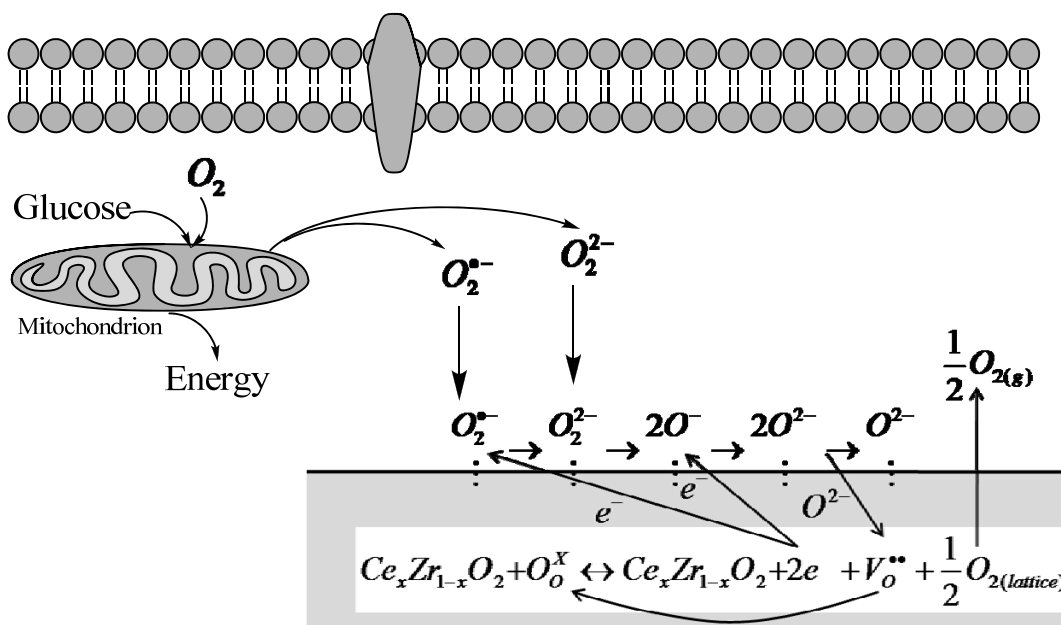


Figure 6-1. Hypothesized scheme of free radical scavenging by $Ce_xZr_{1-x}O_2$ nanoparticles.

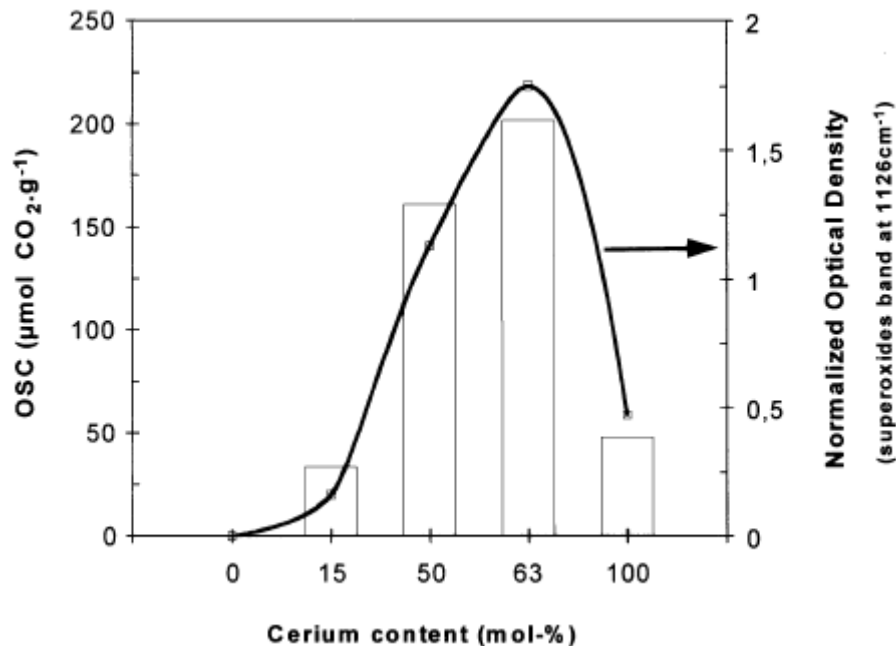


Figure 6-2. OSC of $Ce_xZr_{1-x}O_2$ measured a pulse chromatographic system at 400 °C. Figure reproduced from [62].

6.2 Activities against Hydrogen Peroxide

Among the reactive oxygen species, hydrogen peroxide and superoxide radicals are the most influential ROS in metabolism as well as programmed cell death. Both of them have been widely discussed and their concentrations have been directly measured in biological systems [1]. The concentrations of hydrogen peroxide in biological systems were even used to represent the levels of endogenous oxidative stress or even cell culture's viability [1]. In this chapter, $Ce_xZr_{1-x}O_2$ nanoparticles' scavenging activities against hydrogen peroxide at physiological level are presented. This level of hydrogen peroxide is selected to mimic the efficiency of these nanoparticles in biological systems.

6.2.1 Experimental Methods

To test hydrogen peroxide scavenging, hydrogen peroxide solutions were mixed with $Ce_xZr_{1-x}O_2$ ($x = 0, 0.2, 0.4, 0.6, 0.7, 0.8, 1.0$) suspensions and the residual peroxide concentration

over time was evaluated. Peroxide concentrations in each sample were determined using an Amplex® red hydrogen peroxide/peroxidase assay kit (Cat. # A22188, Invitrogen™). The principle to measure hydrogen peroxide is illustrated in Figure 6-3. The Amplex® reagents were prepared according to manufacturer's instructions. To prepare samples for activity tests, 100 µl of 200 µM $Ce_xZr_{1-x}O_2$ suspensions were prepared in a 96-wells plate (Corning Inc.). A small amounts of substrate hydrogen peroxide was titrated into 0.25 M phosphate buffer (pH = 7.4), forming 100 µM hydrogen peroxide. To initiate the free radical scavenging tests, 100 µl of 100 µM hydrogen peroxide solutions were pipetted into each well at the designated time. The reactions were finally stopped by introducing enzyme horse radish peroxidase and Amplex® reagents into each well at the designated reaction time. The Amplex® reagents were also diluted using 0.25 M phosphate buffer. Each sample's peroxide concentration was determined by measuring the optical density of the red product, resorufin, at 570 nm absorbance. Optical density measurements were made using Synergy HT multi-detection microplate reader (BioTech Instruments Winooski, VT).

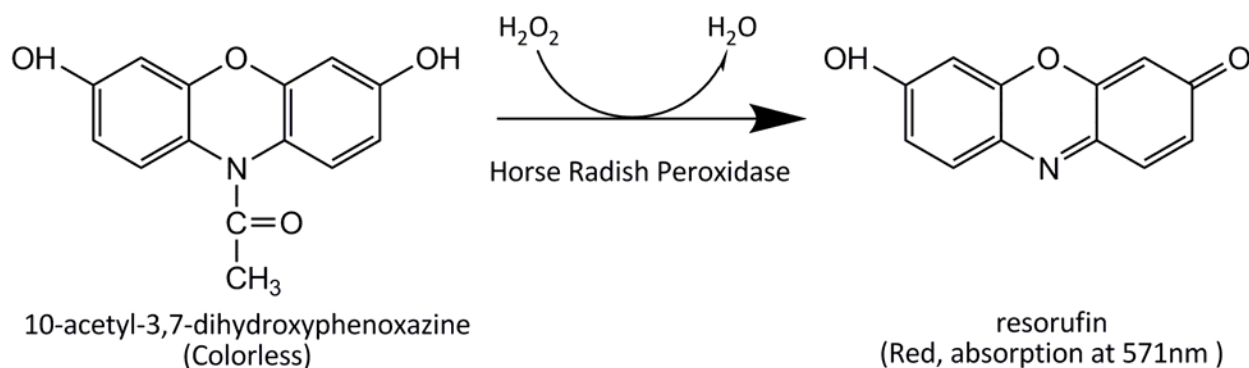


Figure 6-3. Detection scheme used to determine the peroxide concentration in activity tests. Colorless Amplex® Red reagent (10-acetyl-3,7-dihydroxyphenoxazine) reacts with peroxide, forming red resorufin. The reaction is catalyzed by enzyme horse radish peroxidase.

6.2.2 Results and Discussion

The free radical scavenging efficiency of $Ce_xZr_{1-x}O_2$ nanoparticles are determined by measuring the reduction of 50 μ M hydrogen peroxide solutions in 100 μ M $Ce_xZr_{1-x}O_2$ suspensions over time. Figure 6-4(a) shows the peroxide concentration decreased by a series of $Ce_xZr_{1-x}O_2$ nanoparticles over time. Figure 6-4(b) shows the residual hydrogen peroxide concentration divided by initial peroxide concentration in natural logarithmic scale. In Figure 6-4(a), it is obvious that $Ce_{0.7}Zr_{0.3}O_2$ and $Ce_{0.6}Zr_{0.4}O_2$ nanoparticles exhibited the most efficient radical scavenging property, while $Ce_{0.4}Zr_{0.6}O_2$, $Ce_{0.8}Zr_{0.2}O_2$ exhibited moderate efficiency and CeO_2 , $Ce_{0.2}Zr_{0.8}O_2$ exhibited the lowest efficiency. There is no significant peroxide concentration change in the sample of ZrO_2 nanoparticles. In Figure 6-4(b), the slope of each profile represents the hydrogen peroxide scavenging activities of each sample. From high to low, the rankings of peroxide scavenging activities in $Ce_xZr_{1-x}O_2$ nanoparticles are $Ce_{0.7}Zr_{0.3}O_2$, $Ce_{0.6}Zr_{0.4}O_2$, $Ce_{0.4}Zr_{0.6}O_2$, $Ce_{0.8}Zr_{0.2}O_2$, CeO_2 , $Ce_{0.2}Zr_{0.8}O_2$, commercial CeO_2 , and ZrO_2 , respectively.

According to the free radical scavenging mechanism illustrated in Figure 2-2, the scavenging mechanism of hydrogen peroxide can be summarized in Equation (6-4). It is: the adsorption/desorption of peroxide, the transition of peroxide to oxygen ions, and finally the diffusion of oxygen ions into oxygen vacancies in the lattice. The oxygen vacancies are then restored by emitting lattice oxygen molecules. To evaluate the scavenging activities of $Ce_xZr_{1-x}O_2$ nanoparticles, we then simplify Equation (6-4) to Equation (6-5). In Equation (6-3), κ_1 , κ_{-1} , and κ_t , refer to the adsorption constant, desorption constant, catalytic rate constant, respectively. The initial condition in each sample is the same and hydrogen peroxide concentration in each sample is very diluted, thus we are able to ignore the influences from adsorption/desorption (κ_1/κ_{-1}) in the reactions. Therefore, the scavenging activities (i.e. effective rate constant) K can be

calculated using Equation (6-7). The scavenging activity K of each $Ce_xZr_{1-x}O_2$ samples is shown in Figure 6-5 in terms of Ce/Zr molar ratios.

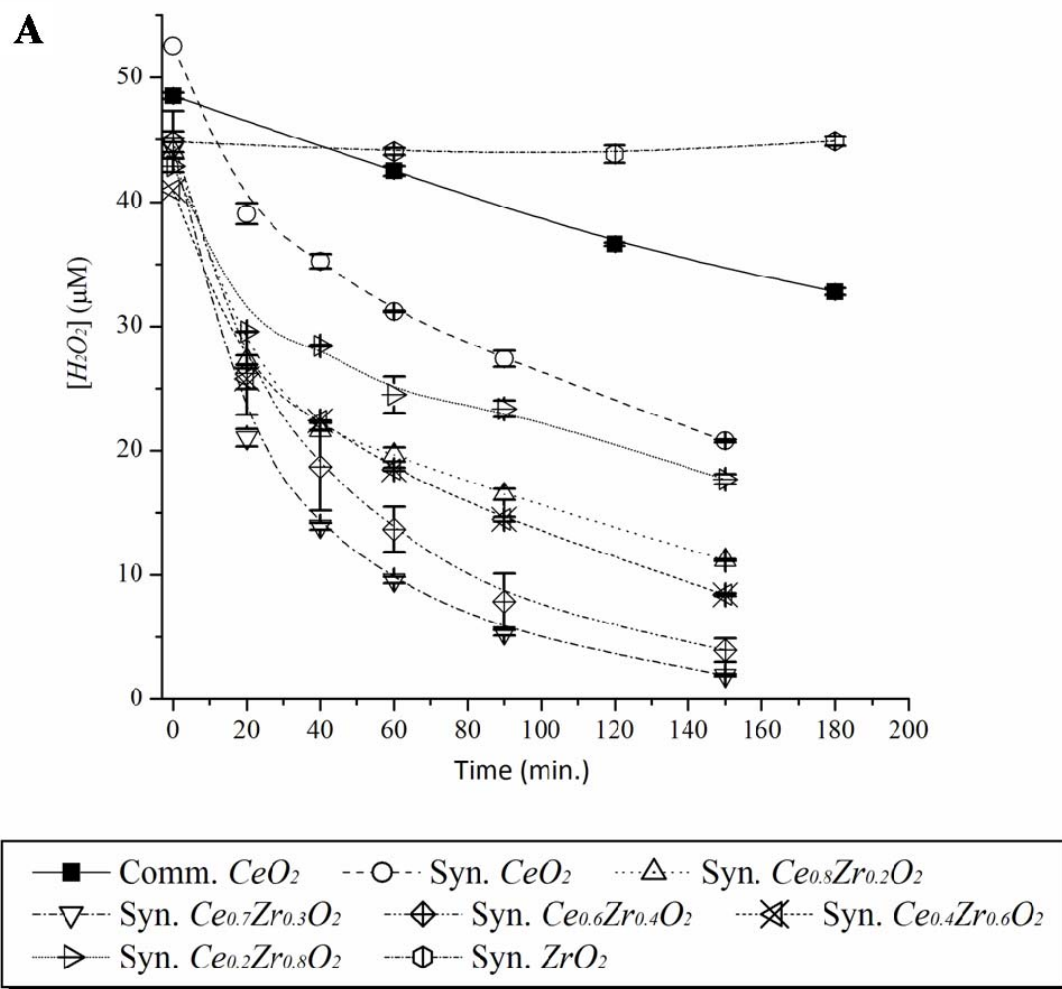


Figure 6-4. A) shows the peroxide concentration in the presence of 7 nm commercial CeO_2 and synthesized $Ce_xZr_{1-x}O_2$ nanoparticles over time. B) shows the natural logarithmic values of the peroxide concentration divided by initial peroxide concentration. The slopes of profiles in B represent the peroxide radical scavenging efficiency.

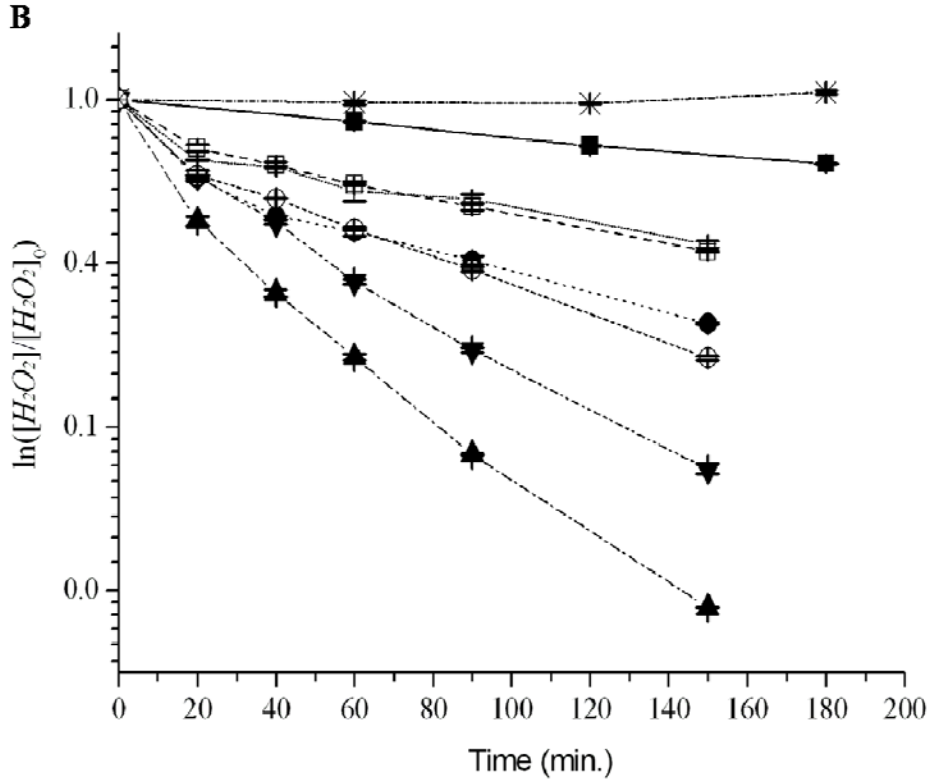
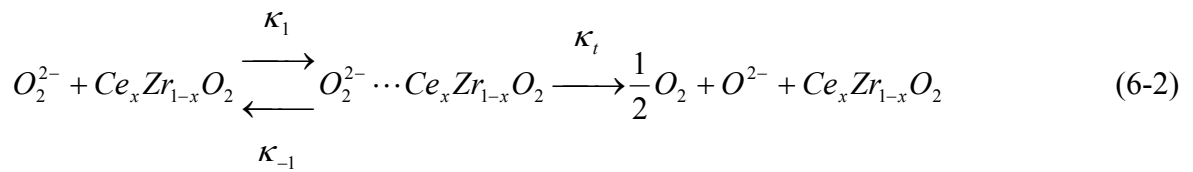
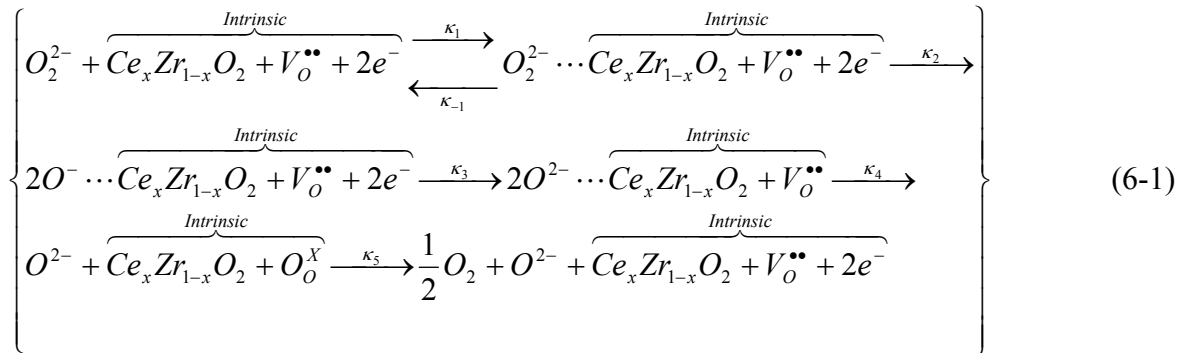


Figure 6-4. Continued.



$$-\frac{d[O_2^{2-}]}{dt} = K \cdot [O_2^{2-}] \cdot [Ce_xZr_{1-x}O_2] \quad (6-3)$$

$$\ln \frac{[O_2^{2-}]}{[O_2^{2-}]_{Initial}} = -K \cdot [Ce_xZr_{1-x}O_2] \cdot t \quad (6-4)$$

where $K = \frac{\kappa_t}{\kappa_M + [O_2^{2-}]}$, $\kappa_M = \frac{\kappa_t + \kappa_{-1}}{\kappa_1}$

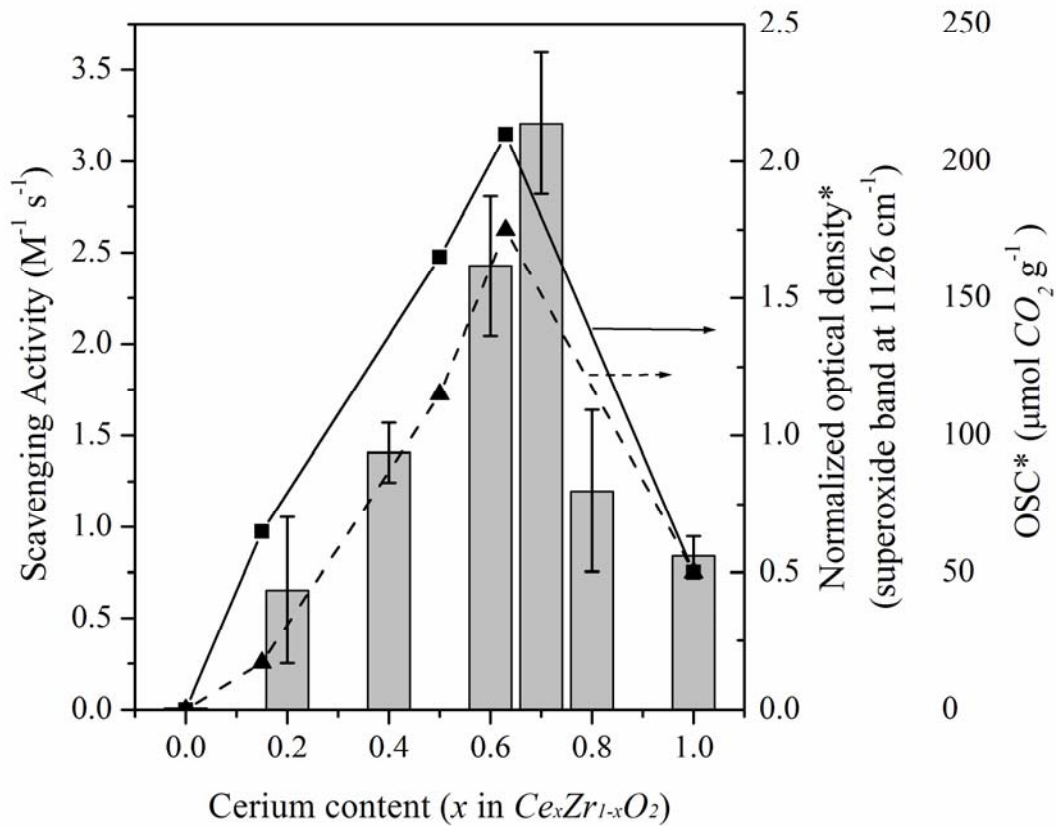


Figure 6-5. The effective scavenging efficiency K of $Ce_xZr_{1-x}O_2$ nanoparticles (bar diagram) vs. OSC (■) and the amount of superoxide radicals (▲) detected on $Ce_xZr_{1-x}O_2$ nanoparticles. The error bars represent the standard deviations of effective efficiencies between each data points [62].

According to the activity tests, the hydrogen peroxide scavenging activities in $Ce_xZr_{1-x}O_2$ nanoparticles is enhanced by doping zirconium ions into CeO_2 lattice. More importantly, the

scavenging activities of $Ce_xZr_{1-x}O_2$ correlates to the magnitudes of OSC measured by pulse chromatographic system [62]. In Figure 6-5, we show that the scavenging activities increase with the amounts of zirconium dopants in CeO_2 lattice. The scavenging activity increases to maximum in $Ce_{0.7}Zr_{0.3}O_2$ nanoparticles, and gradually decreases when more than 40% of cerium ions are substituted. There is no distinguishable peroxide radical scavenging property observed in the case of pure ZrO_2 nanoparticles. On the other hand, OSC measured at 400 °C increases to the highest level when 20% to 40% of cerium ions were substituted; then OSC dropped gradually when more cerium ions were replaced; finally OSC totally diminished in pure ZrO_2 nanoparticles. In addition, the scavenging activity of $Ce_{0.7}Zr_{0.3}O_2$ nanoparticles is four times greater compared to the undoped CeO_2 nanoparticles, corresponding to the same enhancement that occurred in $Ce_{0.63}Zr_{0.37}O_2$ nanoparticles in respect to OSC [48,62]. According to the correlation, the nanoparticle concentrations utilized to evaluate the effective free radical scavenging efficiencies can be replaced by the concentration of active sites. Equation (6-8) shows that the enhanced free radical scavenging efficiency in $Ce_xZr_{1-x}O_2$ is a consequence of improved lattice oxygen vacancies. The correspondence between the free radical scavenging efficiency and the magnitude of OSC confirms the idea that free radical scavenging is mediated by oxygen vacancies. Also, the results deliver a message that the enhanced free radical scavenging activities are achieved by manipulating oxygen vacancies in the CeO_2 lattice.

$$\ln \frac{[O_2^{2-}]}{[O_2^{2-}]_{Initial}} = -K \cdot [V_O^{\bullet\bullet}] \cdot t \quad (6-5)$$

It is worth to note that $Ce_xZr_{1-x}O_2$ nanoparticles may also exhibit greater superoxide radical scavenging properties compared to the undoped CeO_2 . It has been demonstrated that CeO_2 nanoparticles exhibited superoxide dismutase mimetic properties, and their catalytic activity is comparable to enzyme superoxide dismutase [66]. Yet the greater superoxide radical scavenging

properties in $Ce_xZr_{1-x}O_2$ nanoparticles will be demonstrated later. Prior to this work, we found that Descorme et al. had detected larger amounts of superoxide radical adsorption on $Ce_xZr_{1-x}O_2$ nanoparticles than on the undoped CeO_2 , even at room temperature. Importantly, the superoxide radical adsorption on $Ce_xZr_{1-x}O_2$ surfaces also corresponds to the magnitude of OSC in $Ce_xZr_{1-x}O_2$ nanoparticles (shown in Figure 6-5) [62].

In summary, their activities were tested in a 50 μ M hydrogen peroxide solution in order to investigate their free radical scavenging efficiency in biological systems. The free radical scavenging activities of these $Ce_xZr_{1-x}O_2$ nanoparticles is enhanced up to four times in $Ce_{0.7}Zr_{0.3}O_2$ nanoparticles and gradually decreased when tetragonal phase appear in the structures. The effective free radical scavenging activities of $Ce_xZr_{1-x}O_2$ nanoparticles correlates to the magnitude of OSC in the same materials, where OSC is used to evaluate oxygen vacancy concentration in metal oxide catalysts. The correlation confirmed that $Ce_xZr_{1-x}O_2$ nanoparticles scavenge hydrogen peroxide through the exchange of peroxide ions and lattice oxygen, and the scavenging activities are mediated by oxygen vacancies in the lattice. As consequence, the enhanced free radical scavenging properties of CeO_2 nanoparticles are achieved by increasing oxygen vacancies in the lattice through doping zirconium into CeO_2 nanoparticles. The improvement is as great as four times compared to the undoped CeO_2 .

6.3 Activities against Superoxide Radicals

In this section, the scavenging activities of $Ce_xZr_{1-x}O_2$ nanoparticles are tested against superoxide radicals. Different to hydrogen peroxides, superoxide radicals are defined free radicals which have unpaired electrons. Since the electron configurations of superoxide radicals are unpaired, superoxide radicals are much more reactive than hydrogen peroxide and they have great affinity to become hydrogen peroxides or oxygen molecules by electron exchange. Therefore, the half life of superoxide radicals is as short as 0.05 second at high concentrations.

Perhaps, the damage caused by superoxide radicals to biological systems may be more influential than hydrogen peroxide due to their reactivity [1].

6.3.1 Experimental Methods

Due to the short half life of superoxide radicals, it is important to generate this species continuously in the activity tests. To generate the designed radicals, we used hypoxanthine and enzyme xanthine oxidase to produce superoxide radicals, hydrogen peroxide, and uric acids. The hydrogen peroxide produced in this reaction is then removed by adding large amounts of enzyme CAT, in order to prevent the effects from hydrogen peroxide. The reaction used to generate superoxide radicals is illustrated in Figure 6-6.

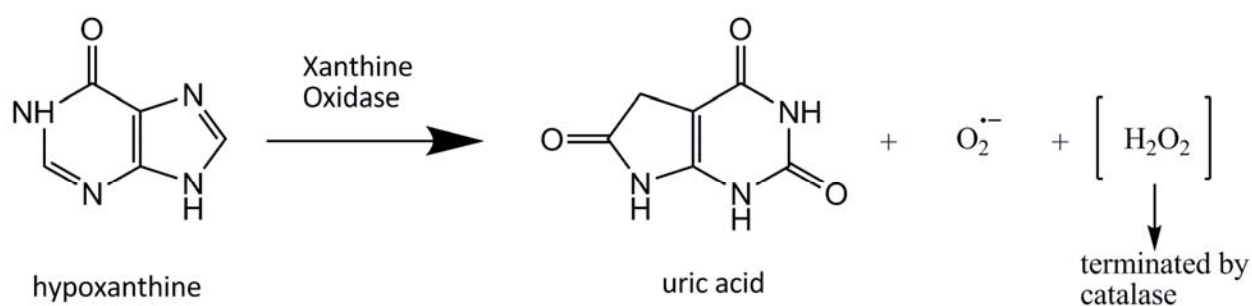


Figure 6-6. Superoxide radicals produced by hypoxanthine and xanthine oxidase.

To detect the presence of superoxide radicals, a water soluble compound, sodium salt of 4-[3-4iodophenyl)-2-(4-nitrophenyl)-2H-5-tetrazolio]-1,3-benzene disulfonate (WST-1, Dojindo), is used as a superoxide probe. Only react with superoxide radicals, WST-1 salts become an irreversible, water-soluble formazan dye (shown in Figure 6-7). The dye formation can be observed at around 450 nm with the maximum density at 438 nm spectrophotometrically [89], and is not affected by the generation of hydrogen peroxide in the reaction. In this study, the formation of formazan dye is observed using two techniques, UV-Vis (UV/Vis - Perkin-Elmer Lambda 800) and microplate reader. UV-Vis spectroscopy and microplate reader are both

spectrophotometric basis; however, comparing to microplate reader UV-Vis is a technique with higher resolution and allows measuring the dye formation continuously. However, the application of UV-Vis is limited by the numbers of samples that can be measured. Therefore, the technique based on microplate reader is engaged in order to test multiple samples simultaneously.

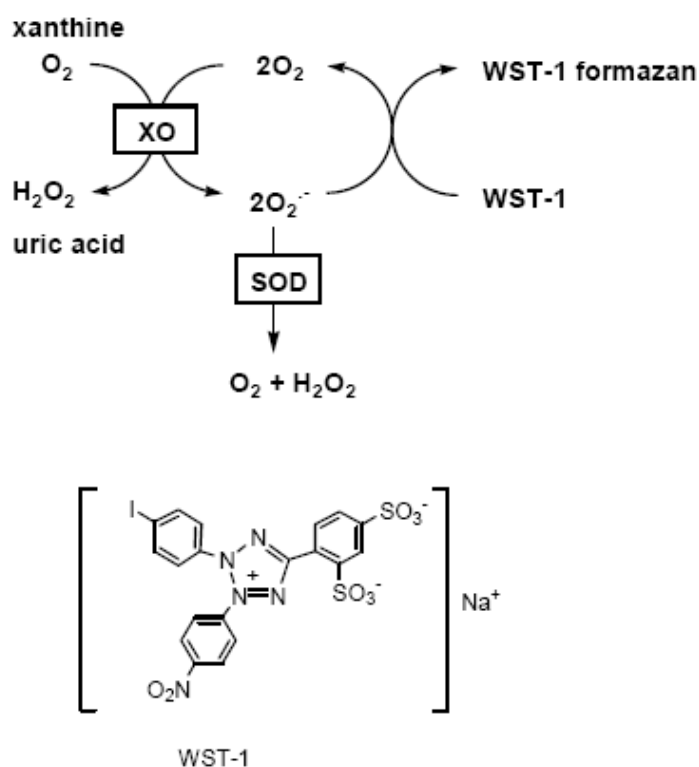


Figure 6-7. Principle of WST-1 assay to detect superoxide radicals [90].

For the samples prepared for UV-Vis, 0.5 mM EDTA (Aldrich), 0.5 mM hypoxanthine (Aldrich), 9.65 mU/ml xanthine oxidase (Invitrogen), 0.5 mM WST-1, and 1 mM $Ce_xZr_{1-x}O_2$ nanoparticle suspensions ($x = 0, 0.4, 0.6, 0.7, 0.8, 1.0$) were prepared in 100 mM phosphate buffer (pH = 7.4, Aldrich) as stock solutions. Two hundreds micro-liters of each stock solution except hypoxanthine stock solution were titrated into a 1 ml cuvette, i.e. EDTA, xanthine

oxidase, WST-1, and nanoparticle suspension. To initiate the reaction, 200 μ l of hypoxanthine stock solution was titrated into the cuvette in order to generate superoxide radicals. The total concentrations of $Ce_xZr_{1-x}O_2$ nanoparticle suspensions were then diluted to 200 μ M in the reactions. The dye formation was detected by UV-Vis at 450 nm. The absorbance was recorded and shown in Figure 6-11. In order to obtain the reaction rate constants of $Ce_xZr_{1-x}O_2$ nanoparticle against to superoxide radicals, another sample prepared with enzyme SOD (Cat. #190117, MP Biomedical LLC) was repeated instead of nanoparticle suspensions. In the experiment, various stock solutions with SOD concentrations (0.25, 0.5, 1, 5, 10, 100 U/ml) were mixed in the cuvettes instead of 1 mM $Ce_xZr_{1-x}O_2$ nanoparticle suspensions. The total concentrations of enzyme SOD were then diluted to 0.05, 0.1, 0.2, 1.0, 2.0, 20 unit/ml in the reactions. The stock solutions, their final concentrations, and experimental procedures are illustrated in Figure 6-8.

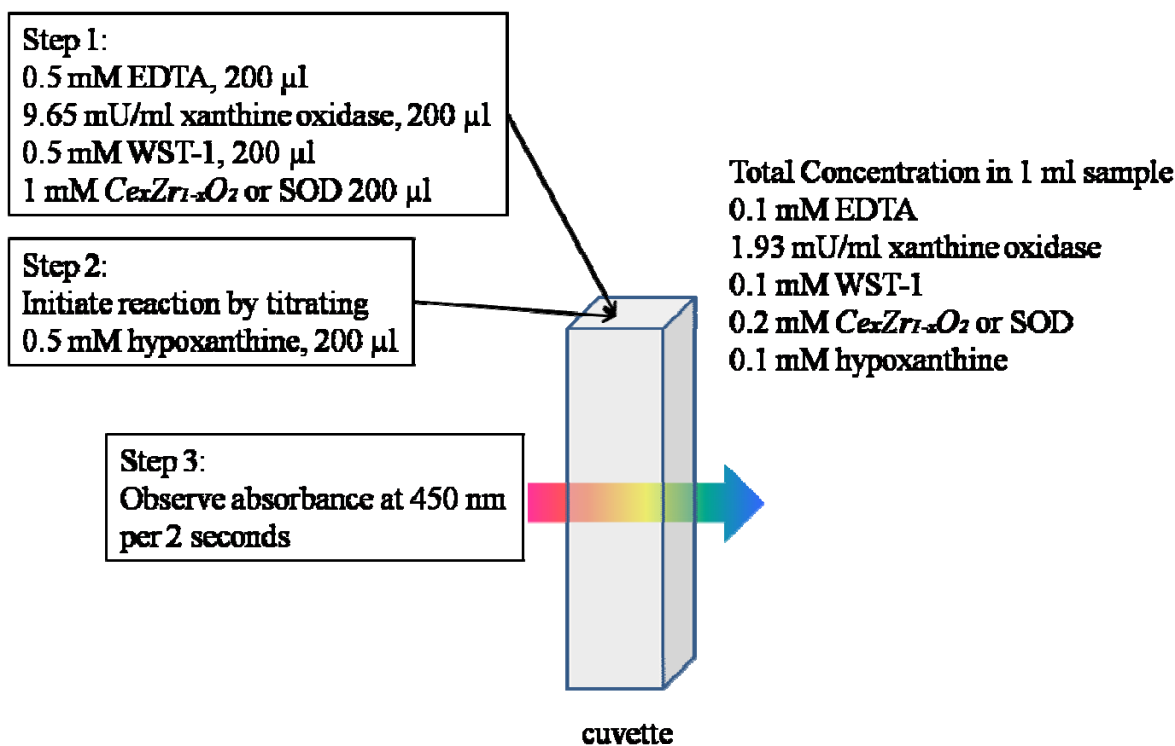


Figure 6-8. Experimental arrangement of stock solution concentrations, total concentrations, and experimental procedures.

For the samples prepared for microplate reader, different nanoparticle concentrations were tested in the setups with various superoxide production rates. The superoxide radical production rates were controlled by the amounts of enzyme xanthine oxidase in the reactions. In the standard radical production rate, the total concentration of 1.93 mU/ml xanthine oxidase was used. However, the reaction may take too long to complete. To conquer this disadvantage, the other two tests with five times (5X) and twenty-five times (25X) of xanthine oxidase (i.e. 9.65 mU/ml and 48.25 mU/ml in total) were repeated using the same experimental procedures.

In the test with standard superoxide production rate (i.e. 1.93 mU/ml xanthine oxidase in total), 0.5 mM EDTA, 0.5 mM hypoxanthine, 9.65 mU/ml xanthine oxidase, and 0.5 mM WST-1 were prepared in 100 mM phosphate buffer (pH = 7.4) as stock solutions. The control samples were a series of enzyme SOD with different concentrations. They were 0.01, 0.05, 0.1, 0.5, 1.0, 2.5, 5.0, 10, 20, 50 U/ml SOD prepared in phosphate buffers. The total concentration of SOD in the reaction therefore was divided by five, which were 0.002, 0.01, 0.02, 0.1, 0.2, 0.5, 1.0, 2.0, 4.0, 10 U/ml. The samples of our interest were $Ce_xZr_{1-x}O_2$ nanoparticle suspensions ($x = 0, 0.4, 0.6, 0.7, 0.8, 1.0$) with three different concentrations. The nanoparticle concentrations were 0.05, 0.25, 1.0 mM in stock solutions, therefore the total concentrations in the test were 0.01, 0.05, 0.2 mM. After the stock solutions were prepared, 50 μ l of tested samples, control samples, and other stock solutions (except hypoxanthine solution) were titrated in a 96 well microplate (Corning, NY) accordingly. Finally, 50 μ l of hypoxanthine solutions were titrated into each well quickly in order to initiate the reaction. The plate was then placed in microplate reader to read the optical density (absorbance) at 450 nm. Figure 6-9 shows the arrangement of sample preparation in microplate and the concentration of each stock solution in the plate.

The activity tests underwent in higher superoxide production rates were carried out under similar protocols. The concentrations of xanthine oxidase that was used to proceed different superoxide production rates were increased from 1.93 mU/ml to 9.65 mU/ml and 48.25 mU/ml in total.

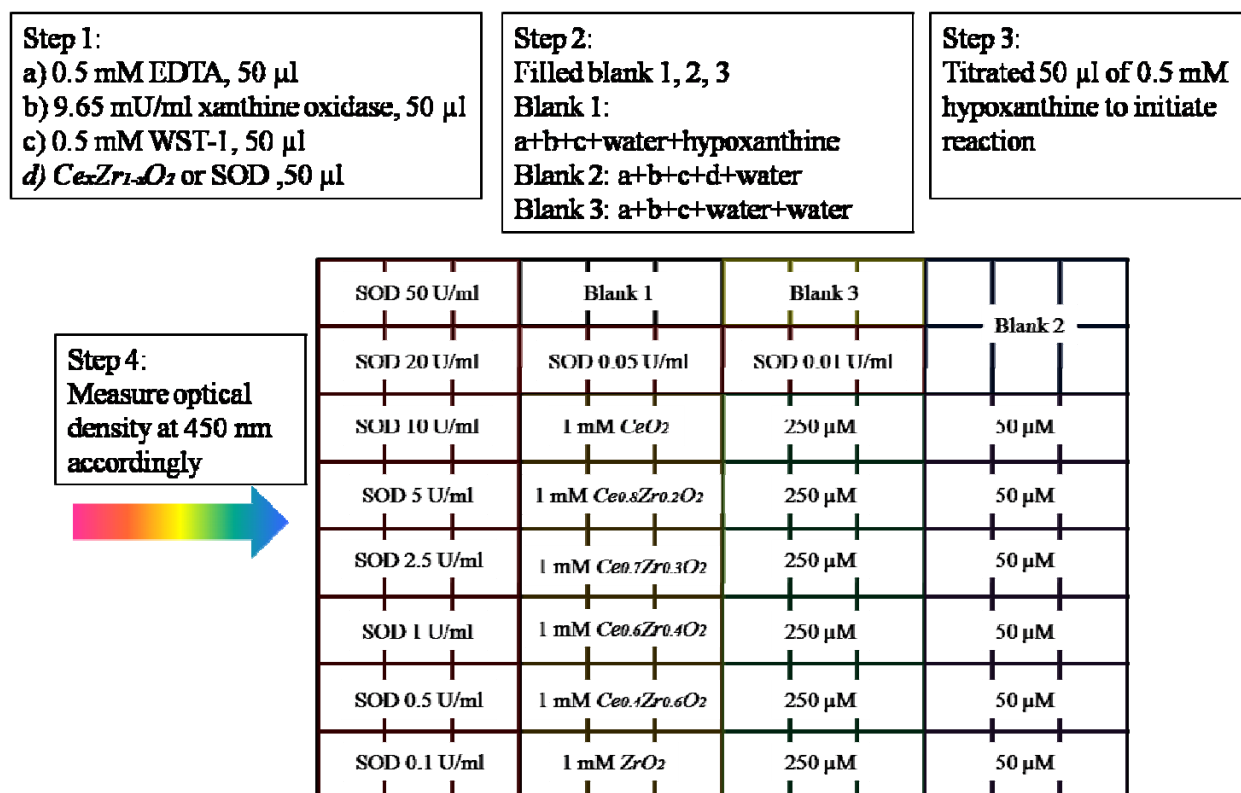


Figure 6-9. The setup of stock solutions and their concentrations in a 96-wells microplate.

6.3.2 Results and Discussion

Figure 6-10 shows the results of activity tests using UV-Vis. In Figure 6-10, each profile represents the absorbance of each sample over time. The absorbance readings are results of formazan dye formation, which are caused by the interaction of WST-1 and superoxide radicals. Thus, the dropped optical density in the control sample is a result of protection received from enzyme SOD. The inhibition from dye formation represents the enzyme activity, so the

inhibition is used to calculate the rate constants in the reaction. In Figure 6-10, the inhibition to dye formation is SOD concentration dependent. The samples with 1 U/ml or higher concentration of enzyme SOD achieved 100% protection, while the different percentage of protection is distinguishable in the diagram.

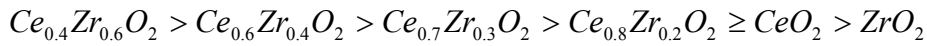
Figure 6-11 shows the results of the same experimental setups but $Ce_xZr_{1-x}O_2$ nanoparticles were used to scavenge superoxide radicals instead of enzyme SOD. In Figure 6-11, $Ce_{0.4}Zr_{0.6}O_2$ has greater inhibition percentages to dye formation, indicating a greater superoxide scavenging activity. Also, ZrO_2 has no significant superoxide scavenging activity, while CeO_2 has the lowest activity among all the CeO_2 -based nanoparticles. The rankings of superoxide scavenging activity in $Ce_xZr_{1-x}O_2$ nanoparticles are listed as follow according to the results in Figure 6-11.



The results can be concluded that zirconium dopants in CeO_2 nanoparticles prompt the scavenging activities against superoxide radicals. The scavenging activities in $Ce_xZr_{1-x}O_2$ nanoparticles become zirconium dopants dependent but not oxygen vacancy concentration dependent.

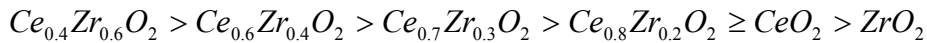
Figure 6-12 shows the results of activity tests measured by microplate reader. The superoxide radicals in this test were produced by 1.93 mU/ml xanthine oxidase and 0.1 mM hypoxanthine. Each data point was the average of three different measurements, and the standard errors were included in the marks. Figure 6-12(a) shows the inhibition to dye formation in samples with enzyme SOD. In Figure 6-12(a), it is obvious that the inhibition to dye formation is SOD concentration dependent. The SOD concentrations greater than 0.5 U/ml totally inhibit dye formation made by superoxide radicals. In Figure 6-12(b), inhibition to dye formation also occurred as 200 μ M $Ce_xZr_{1-x}O_2$ nanoparticles were involved in the reaction.

According to the profiles, $Ce_{0.4}Zr_{0.6}O_2$ nanoparticles exhibit the greatest superoxide radical scavenging activity, and the activities of $Ce_xZr_{1-x}O_2$ nanoparticles decrease as fewer dopants incorporated in the solid solutions. In contrast to the CeO_2 -based nanoparticles, ZrO_2 nanoparticles exhibited none or indistinguishable scavenging activity. In Figure 6-12(c) and (d), inhibition to dye formation is reproducible when lower nanoparticle concentrations present in the reaction. 50 μ M and 10 μ M $Ce_xZr_{1-x}O_2$ nanoparticles also performed distinguishable scavenging activity against superoxide radicals; however, the protections were not as efficient as in the systems of 200 μ M $Ce_{0.4}Zr_{0.6}O_2$ nanoparticles. According to the results in Figure 6-12, it can be concluded that the rankings of superoxide scavenging activity in $Ce_xZr_{1-x}O_2$ nanoparticles are,



The scavenging activities of $Ce_xZr_{1-x}O_2$ nanoparticles are zirconium dopants dependent. The results correspond to the observation in experiments carried out by UV-Vis.

The same experiment was reproduced with higher xanthine oxidase concentrations (9.65 and 48.25 mU/ml) in order to shorten the reaction time. The results are shown in Figure 6-13 and Figure 6-14. In Figure 6-13 and Figure 6-14, the results are reproducible compared to that of 1.93 mU/ml xanthine oxidase. The scavenging activities of CeO_2 and $Ce_{0.8}Zr_{0.2}O_2$ are very close, while very limited scavenging activity was observed in ZrO_2 samples. The superoxide radical scavenging activities of $Ce_xZr_{1-x}O_2$ nanoparticles are ranked as follow,



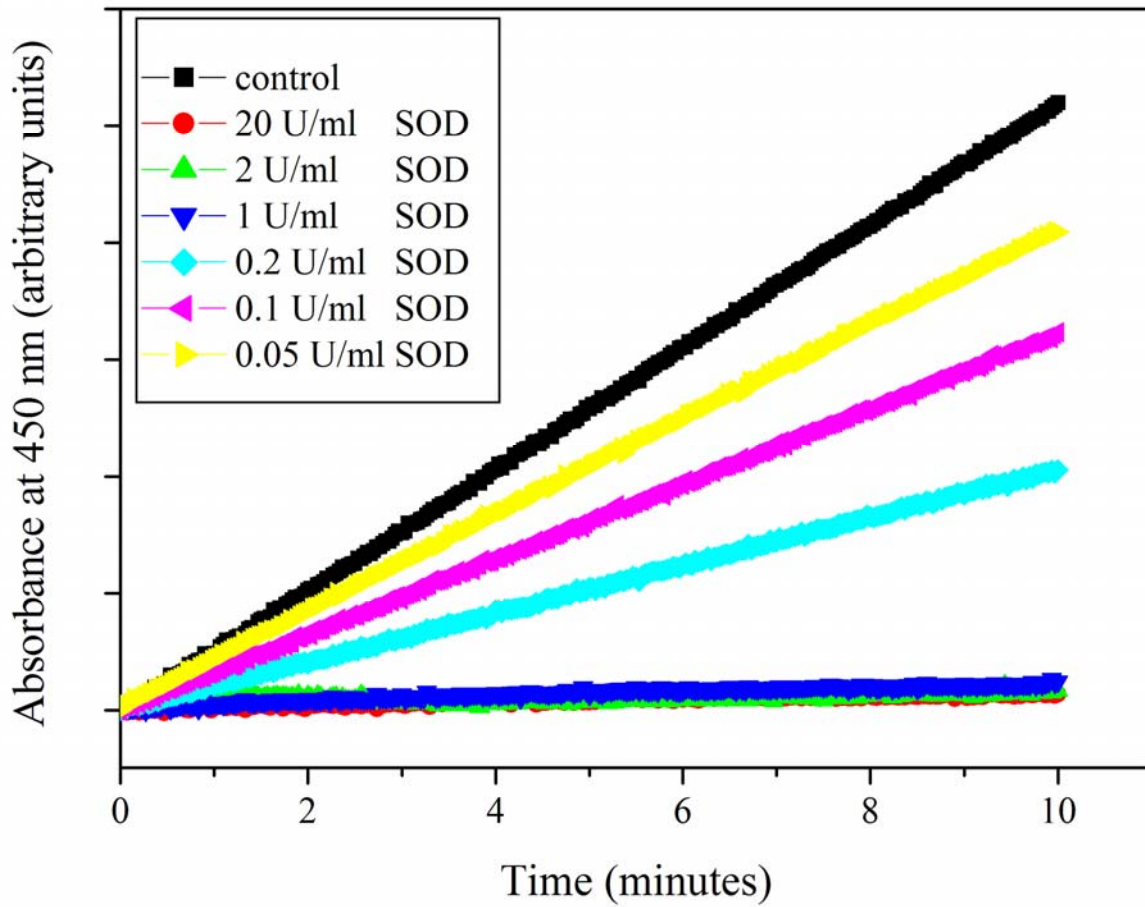


Figure 6-10. The results of activity test obtained using UV-Vis. A series of enzyme SOD with different concentrations (total concentration) protected WST-1 salts against superoxide radicals. The higher the absorbance indicates the more formazan formation caused by superoxide radicals.

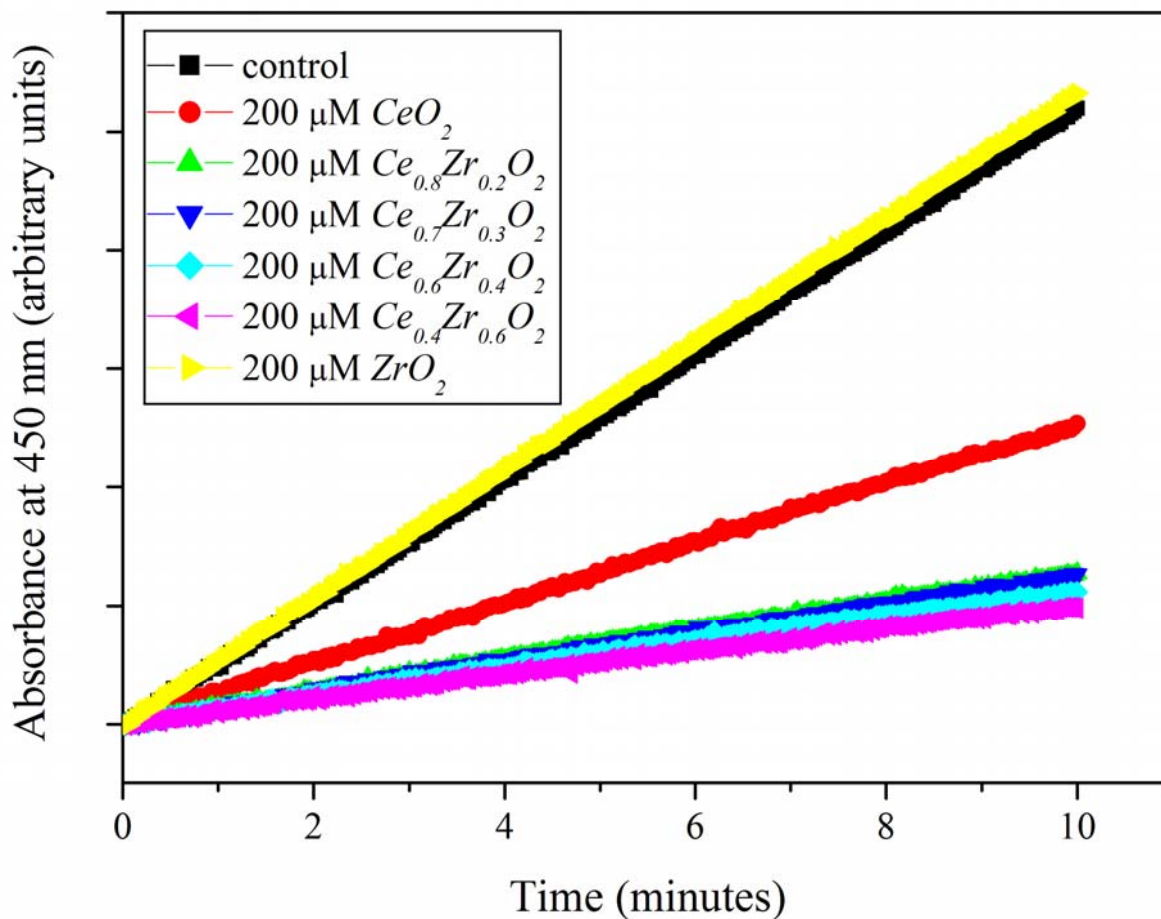


Figure 6-11. The results of activity tests obtained using UV-Vis. A series of 200 μM $Ce_xZr_{1-x}O_2$ nanoparticles ($x = 0, 0.4, 0.6, 0.7, 0.8, 1.0$) with different concentrations protected WST-1 salts against superoxide radicals. The higher the absorbance indicates the more formazan formation caused by superoxide radicals. The results have shown that $Ce_xZr_{1-x}O_2$ nanoparticles exhibit extraordinary scavenging properties against superoxide radicals.

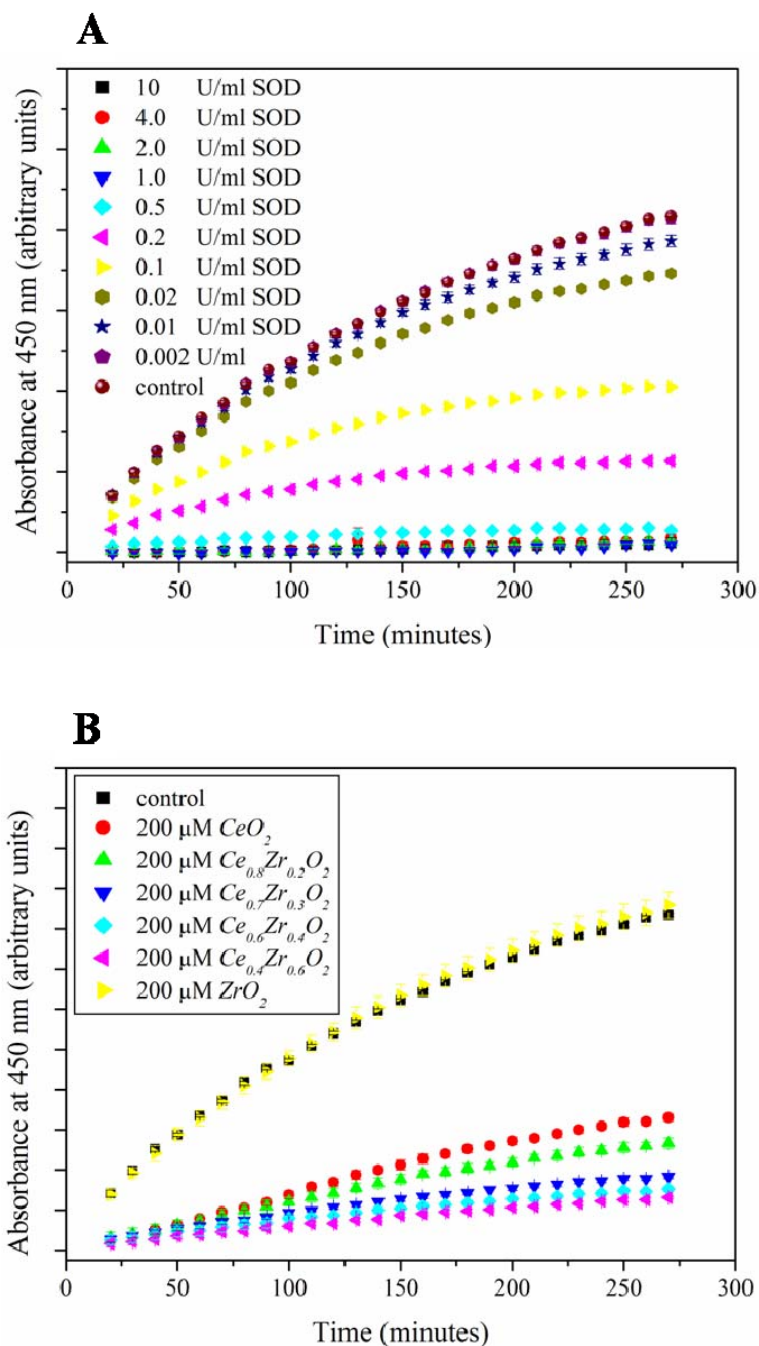


Figure 6-12. The results of activity tests measured by microplate reader. A) shows the inhibition to dye formation in samples with enzyme SOD. B) in samples with 200 μM $\text{Ce}_x\text{Zr}_{1-x}\text{O}_2$ nanoparticles. C) in samples with 50 μM $\text{Ce}_x\text{Zr}_{1-x}\text{O}_2$ nanoparticles. D) in samples with 10 μM $\text{Ce}_x\text{Zr}_{1-x}\text{O}_2$ nanoparticles. The superoxide radicals in all samples were produced by 1.93 mU/ml xanthine oxidase and 0.1 mM hypoxanthine. Each data point was the averaged result of three samples. Standard errors are shown in each data point; however most of the error bars are smaller than the marks.

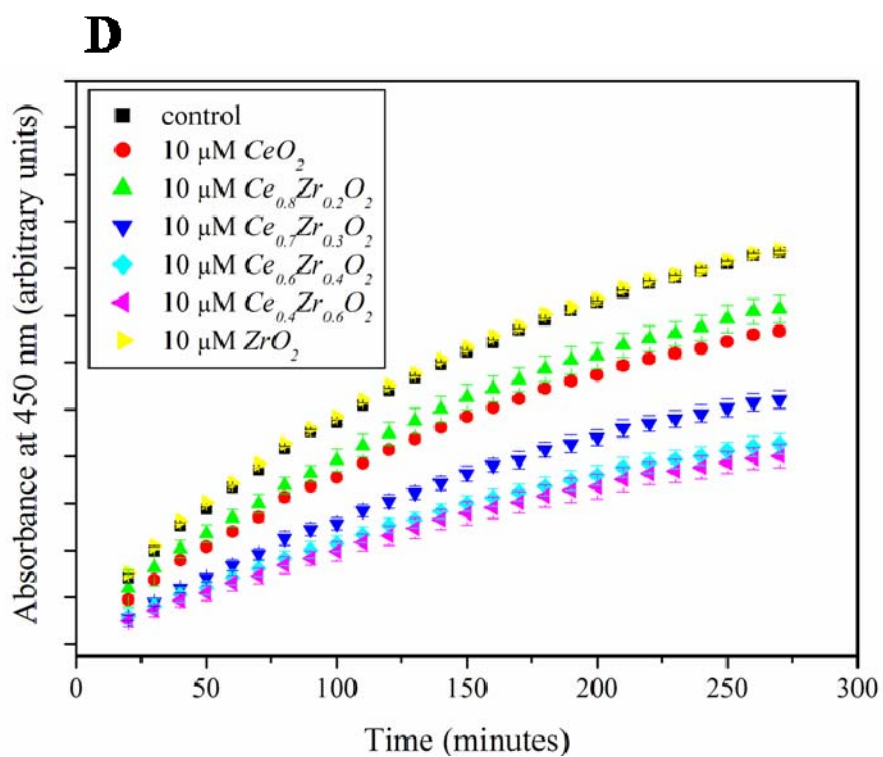
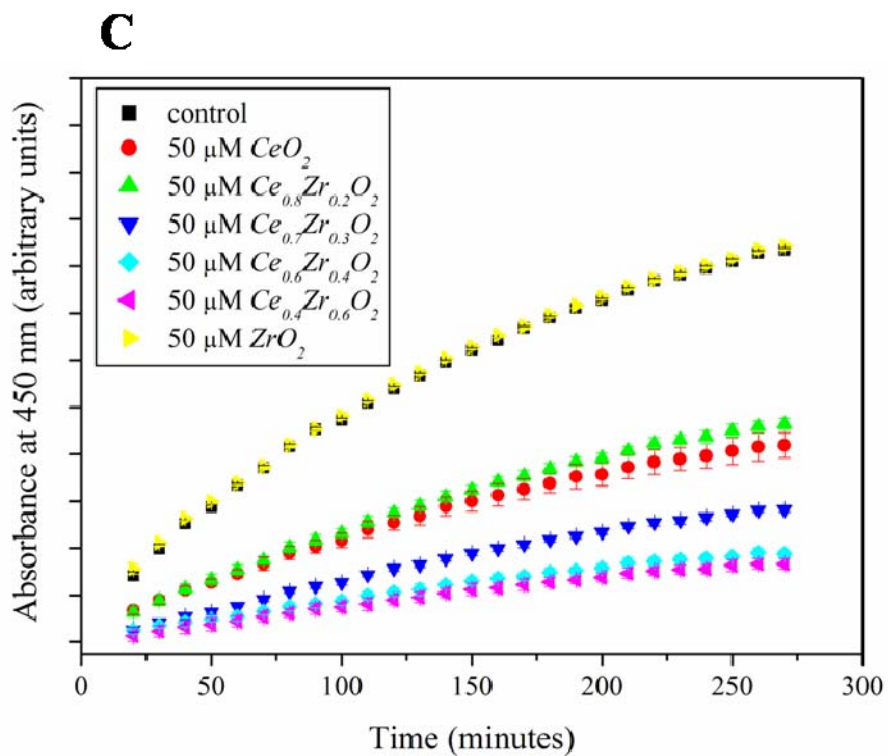


Figure 6-12. Continued.

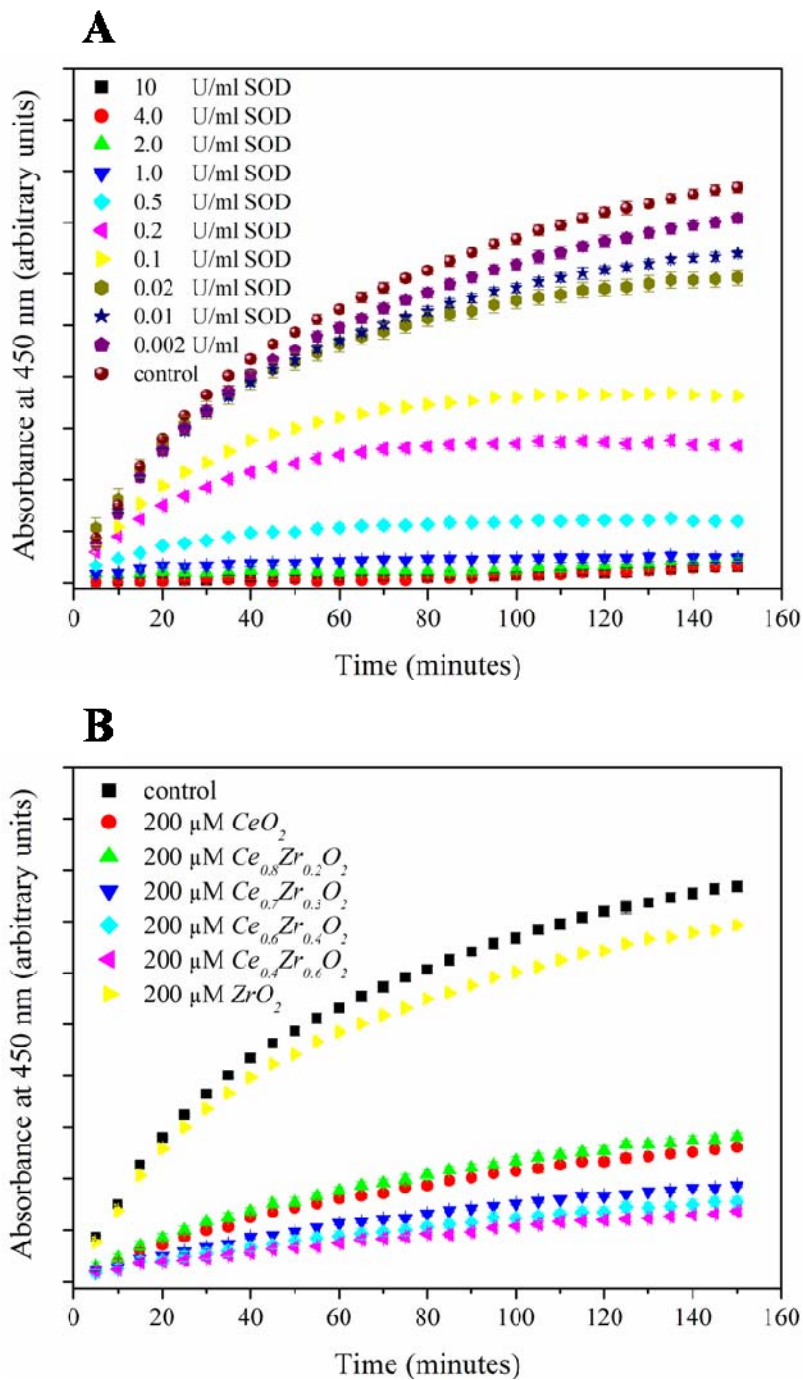


Figure 6-13. The results of activity tests measured by microplate reader. A) shows the inhibition to dye formation in samples with enzyme SOD. B) in samples with 200 μM $Ce_xZr_{1-x}O_2$ nanoparticles. C) in samples with 50 μM $Ce_xZr_{1-x}O_2$ nanoparticles. D) in samples with 10 μM $Ce_xZr_{1-x}O_2$ nanoparticles. The superoxide radicals in all samples were produced by 6.95 mU/ml xanthine oxidase and 0.1 mM hypoxanthine. Each data point was the averaged result of three samples. Standard errors are shown in each data point; however most of the error bars are smaller than the marks.

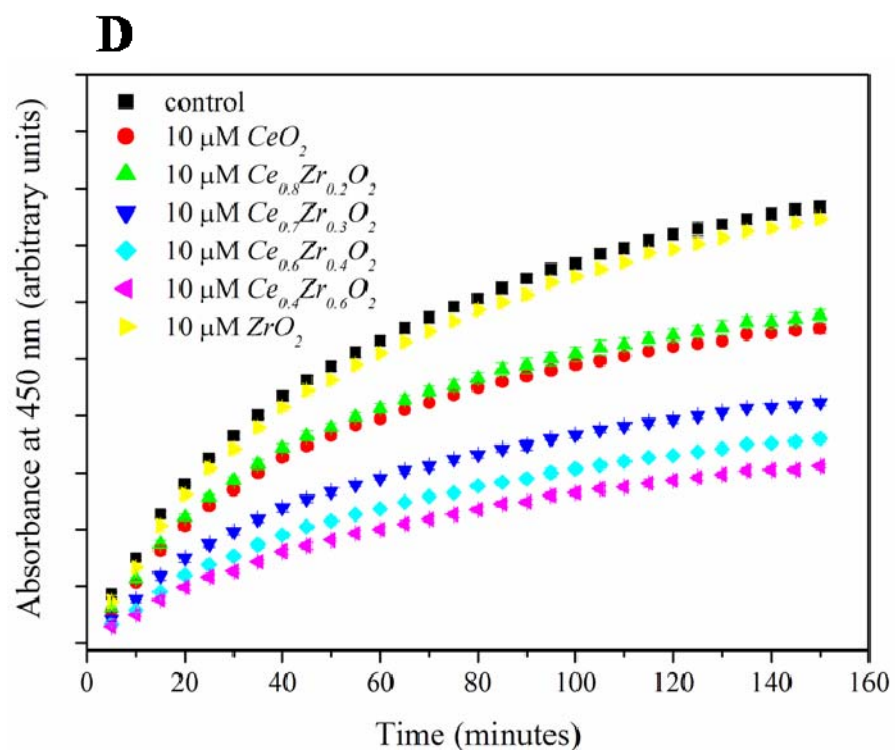
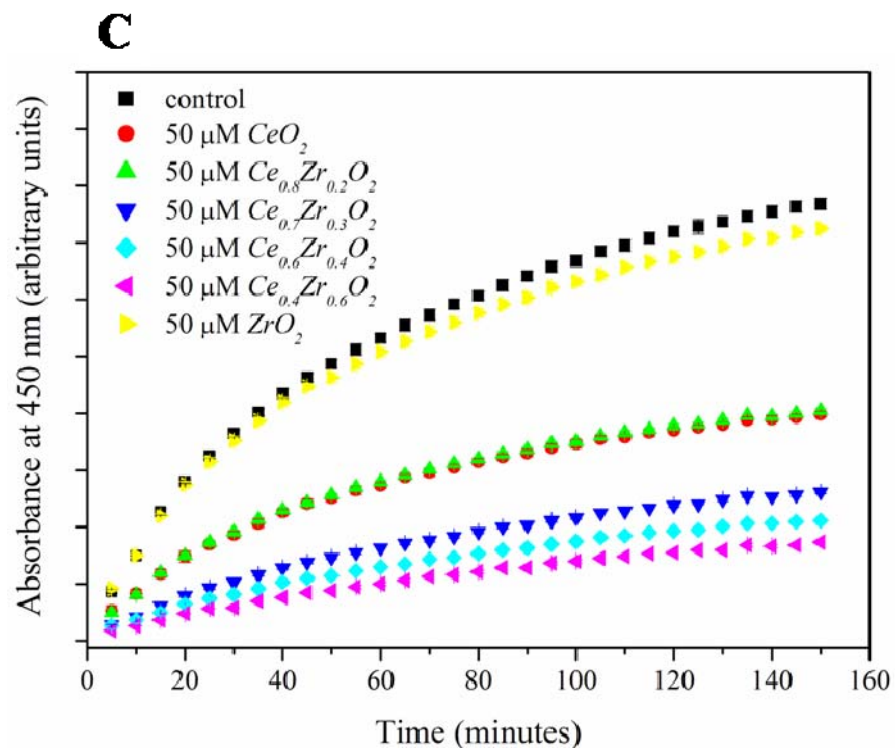


Figure 6-13. Continued.

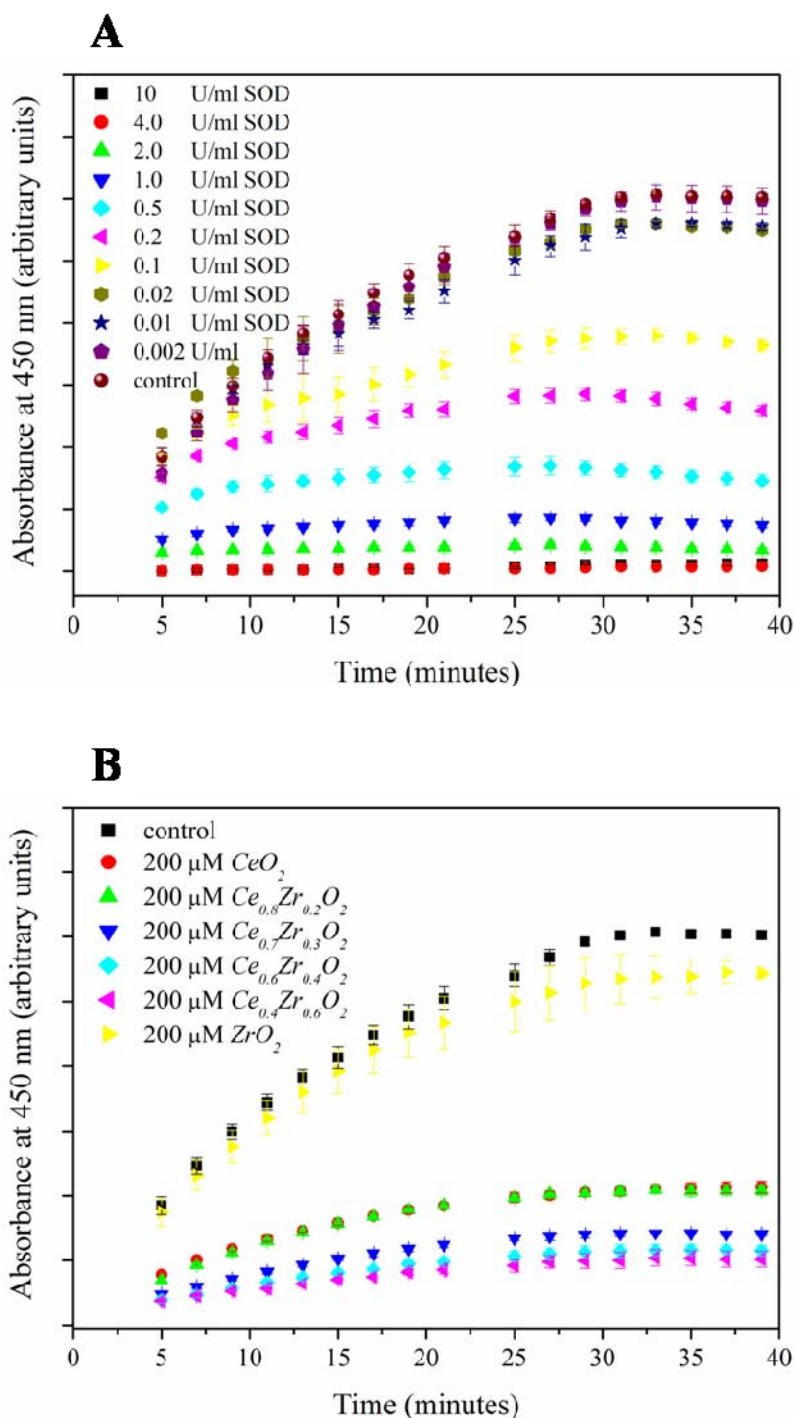


Figure 6-14. The results of activity tests measured by microplate reader. A) shows the inhibition to dye formation in samples with enzyme SOD. B) in samples with 200 μM $\text{Ce}_x\text{Zr}_{1-x}\text{O}_2$ nanoparticles. C) in samples with 50 μM $\text{Ce}_x\text{Zr}_{1-x}\text{O}_2$ nanoparticles. D) in samples with 10 μM $\text{Ce}_x\text{Zr}_{1-x}\text{O}_2$ nanoparticles. The superoxide radicals in all samples were produced by 48.25 mU/ml xanthine oxidase and 0.1 mM hypoxanthine. Each data point was the averaged result of three samples. Standard errors are shown in each data point; however most of the error bars are smaller than the marks.

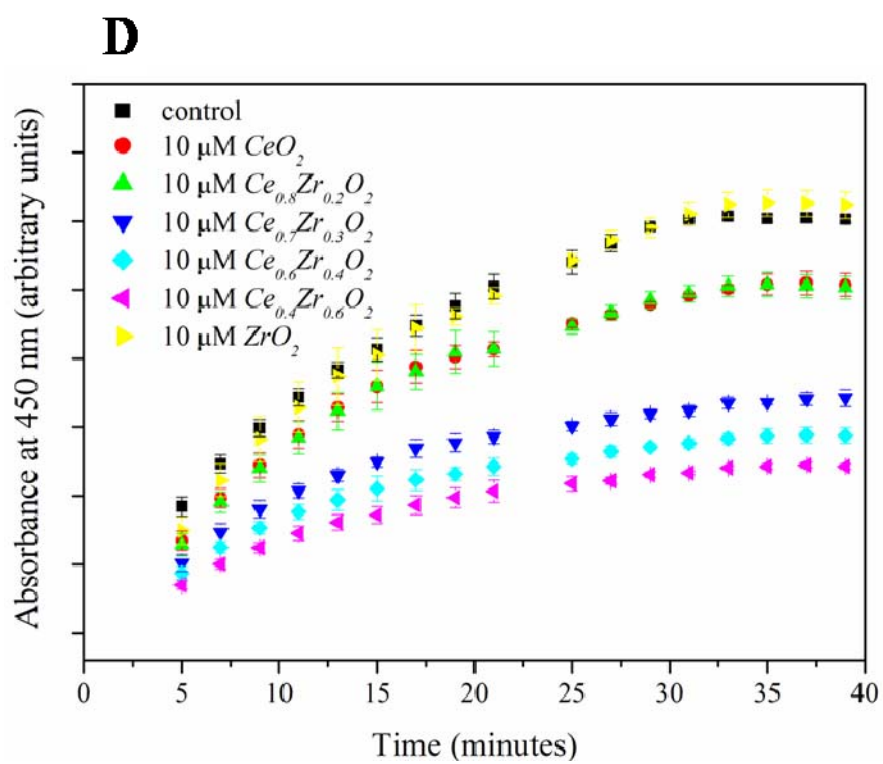
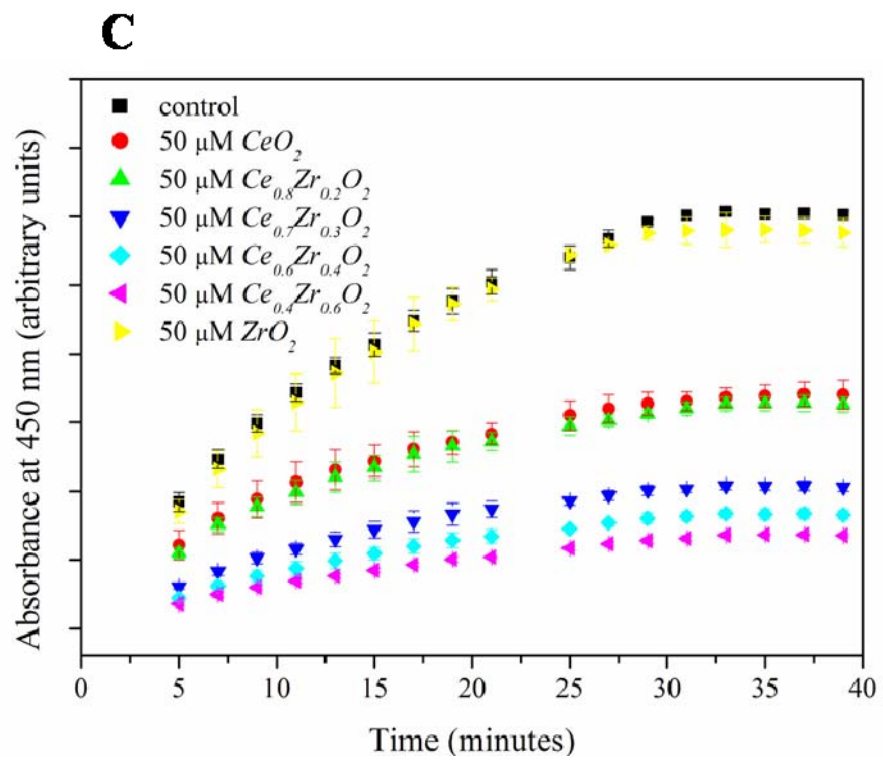


Figure 6-14. Continued.

To calculate the reaction rate constants of $Ce_xZr_{1-x}O_2$ against superoxide radicals, a method to compare the inhibition percentages of $Ce_xZr_{1-x}O_2$ nanoparticles and enzyme SOD is adopted.

The inhibition rate is perceived using the equation in the follow,

$$Activity(inhibitionrate\%) = \frac{\{(A_{blank1} - A_{blank3}) - (A_{sample} - A_{blank2})\}}{(A_{blank1} - A_{blank3})} \times 100 \quad (6-6)$$

Where A represents the absorbance or optical density of samples or blanks in each well.

The denominator in the equation represents the increasing amounts of dye formation in the absence of samples but with superoxide radicals in the reactions. The numerator in the equation represents the inhibition due to tested samples (i.e. enzyme SOD or $Ce_xZr_{1-x}O_2$ nanoparticles) in the presence of superoxide radicals. Thus, the equation is to show the inhibition percentage of dye formation when the tested samples involved in superoxide radical production. To obtain the rate constant, the amounts of enzymes or nanoparticle concentrations that are required to achieve 50% of inhibition are compared. Using the comparative method, the reaction rate constants of $Ce_xZr_{1-x}O_2$ nanoparticles can be obtained according to the reaction rate constant of SOD, $1.3-2.8 \times 10^9 \text{ M}^{-1}\text{s}^{-1}$ (at pH = 7.2, M.W. = 32,600 g/mole).

The inhibition curve of enzyme SOD is shown in Figure 6-15, and the calculation is based on the results in Figure 6-12. The concentrations for enzyme SOD and $Ce_xZr_{1-x}O_2$ nanoparticles to achieve 50% of inhibition rate are calculated according to the results in Figure 6-12 and Figure 6-15, and the values are shown in Table 6-1.

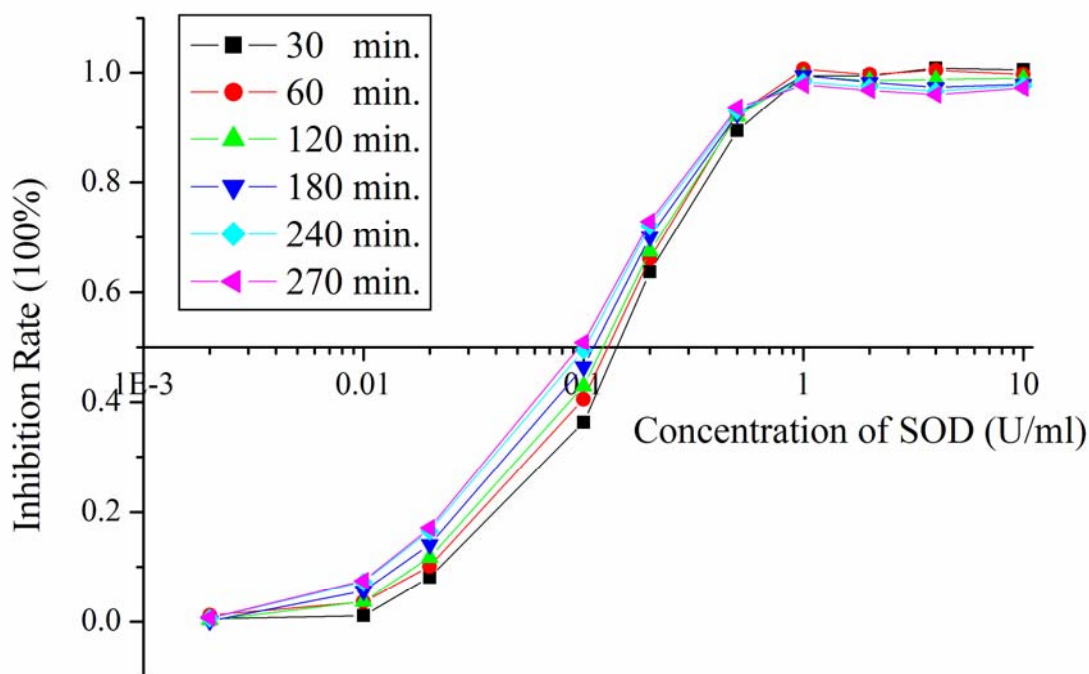


Figure 6-15. Inhibition curves of enzyme SOD with different incubation time. The amounts of SOD that achieved 50% inhibition rate is used to compare the amounts of $Ce_xZr_{1-x}O_2$ nanoparticles that has achieved the same inhibition.

Table 6-1. Concentrations for enzyme SOD and $Ce_xZr_{1-x}O_2$ nanoparticles to achieve 50% of inhibition rate in activity test.

	Concentration to achieve 50% inhibition rate (mole/L)						
	SOD (U/ml)	CeO_2	$Ce_{0.8}Zr_{0.2}O_2$	$Ce_{0.7}Zr_{0.3}O_2$	$Ce_{0.6}Zr_{0.4}O_2$	$Ce_{0.4}Zr_{0.6}O_2$	ZrO_2
Measured at 30 min.	0.150	42.1	44.3	6.3	6.1	5.7	2983.3
60 min.	0.137	40.8	45.5	6.5	6.0	5.8	6020.0
120 min.	0.129	46.1	51.3	7.0	6.2	6.0	16200.0
180 min.	0.115	48.6	54.6	7.3	6.4	6.1	5645.5
240 min.	0.102	49.8	56.6	7.5	6.5	6.2	4773.3
270 min.	0.10	50.3	57.6	7.6	6.5	6.2	3413.6

Since the concentration of 1.0 U/ml SOD approximately equals to 120 nM SOD [29], the reaction rate constants of $Ce_xZr_{1-x}O_2$ nanoparticles can be obtained using simple calculations.

Due to the high molecular weights of SOD, it is necessary to interpret the reaction rate constant

into the format of $(\text{g/l})^{-1}\text{s}^{-1}$ instead of $\text{M}^{-1}\text{s}^{-1}$. The rate constants of all samples are shown in Table 6-2. In Table 6-2, it is shown that rate constants of $\text{Ce}_x\text{Zr}_{1-x}\text{O}_2$ nanoparticles are even higher than enzyme SOD in respect to scavenging superoxide radicals. Enzyme SOD has been tested to exhibit the fastest reaction rate among all enzymes, and its reaction rate is only limited by colloid frequency to superoxide radicals.

Table 6-2. Reaction rate constants of $\text{Ce}_x\text{Zr}_{1-x}\text{O}_2$ nanoparticles against superoxide radicals. The kinetic analysis was measured by microplate reader using WST-1 salts in the samples with 1.93 mU/ml xanthine oxidase.

Scavengers	M.W. (g/mol)	Rate Constant ($\text{M}^{-1}\text{s}^{-1}$)	Rate Constant [(g/l)$^{-1}\text{s}^{-1}$]
SOD	32,600	1.3-2.8$\times 10^9$	39.9$\times 10^3$
CeO_2	172.72	0.6-1.2$\times 10^6$	3.7-7.1$\times 10^3$
$\text{Ce}_{0.3}\text{Zr}_{0.7}\text{O}_2$	163.25	0.6-1.1$\times 10^6$	3.4-7.0$\times 10^3$
$\text{Ce}_{0.7}\text{Zr}_{0.3}\text{O}_2$	158.24	4.3-8.0$\times 10^6$	27.0-50.5$\times 10^3$
$\text{Ce}_{0.6}\text{Zr}_{0.4}\text{O}_2$	153.96	5.0-8.4$\times 10^6$	32.8-54.5$\times 10^3$
$\text{Ce}_{0.4}\text{Zr}_{0.6}\text{O}_2$	143.67	5.2-8.9$\times 10^6$	36.0-61.9$\times 10^3$
ZrO_2	123.22	2.7-16.9$\times 10^3$	0.021-0.14$\times 10^3$

In Table 6-2, it is found that zirconium dopants are able to improve superoxide radical scavenging activities of $\text{Ce}_x\text{Zr}_{1-x}\text{O}_2$ nanoparticles. Instead of correlating to the OSC, the scavenging activities of $\text{Ce}_x\text{Zr}_{1-x}\text{O}_2$ nanoparticles actually correlate to the amounts of zirconium dopants in the system. The rankings and magnitude of improvements do not correspond to the hypothesis.

The results suggest that superoxide radical scavenging activities of $\text{Ce}_x\text{Zr}_{1-x}\text{O}_2$ nanoparticles are correlated with the amounts of zirconium dopants in the lattice but not oxygen vacancy concentrations. The results also conflict what was demonstrated in previous chapters that hydrogen peroxide scavenging activities of $\text{Ce}_x\text{Zr}_{1-x}\text{O}_2$ nanoparticles are correlated with

oxygen vacancy concentrations in lattices. The differences are due to the nature of hydrogen peroxide and superoxide radicals. Comparing to hydrogen peroxide, superoxide radicals are more active due to their unpaired electron configurations. In the catalytic reactions with catalase two steps of chemical reactions are involved. First, hydrogen peroxides donate an oxygen ion to the reduced catalase, forming an intermediate compound. Second, the intermediate compound donates its extra oxygen ion to another hydrogen peroxide, forming water and one oxygen molecule. Except the reactions contributed by electron exchange, it is noticed that oxygen ions also involve in catalysis in the case of hydrogen peroxide. Different to the catalysis to hydrogen peroxide, the catalytic reactions between superoxide radicals and enzyme SOD do not involve the exchange of oxygen ions. It is, superoxide radicals only donate their unpaired electrons to form oxygen molecules or receive electrons to form hydrogen peroxide. In the particular reaction, the scavenging to superoxide radicals are carried out through electron exchange and no oxygen ions are involved. Thus, it can be concluded that the catalysis of superoxide radicals only contributed by the electron exchange with enzyme SOD. However, in the case of $Ce_xZr_{1-x}O_2$ nanoparticles, the electron exchange not only contributed by oxygen vacancies, but also contributed by other cationic defects in the lattice.

To further explain what species of cationic defects contribute in superoxide radical scavenging, it is necessary to investigate the Ce^{3+}/Ce^{4+} ratios in $Ce_xZr_{1-x}O_2$ nanoparticles. Figure 6-16 shows the Ce^{3+} contents and OSC in $Ce_xZr_{1-x}O_2$ nanoparticles reported by Vidal et al. [68,69]. In Figure 6-16, the Ce^{3+} contents were obtained using magnetic susceptibility measurements through a magnetic balance under flowing H_2 (5%)/He gas. The Ce^{3+} contents, or as reduction percentages, were calculated on a $[Ce^{3+}]/[Ce^{3+}+Ce^{4+}]$ basis. According to the reports [68,69], zirconium dopants in the solid solutions promote reduction capability of

nanocrystallites. The results are reproducible at low and high temperatures (473-973 K). The results shown by Vidal et al. may provide the answer for the results that obtained in the superoxide radical scavenging tests.

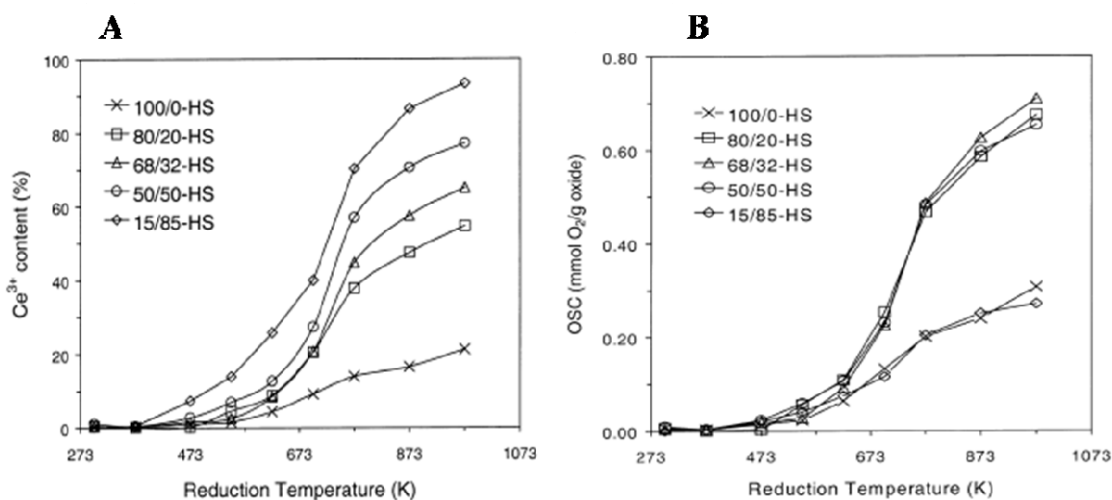
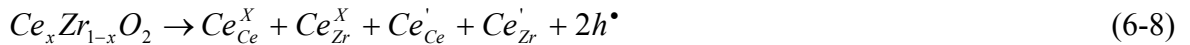


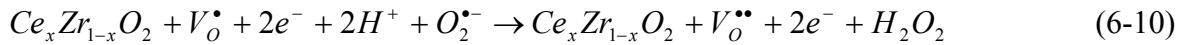
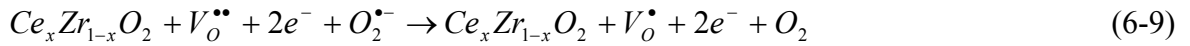
Figure 6-16. A) Ce^{3+} contents and B) OSC in $Ce_xZr_{1-x}O_2$ nanoparticles. CZ100/0-HS (CeO_2); CZ80/20-HS ($Ce_{0.8}Zr_{0.2}O_2$); CZ68/32-HS ($Ce_{0.68}Zr_{0.32}O_2$); CZ50/50-HS ($Ce_{0.5}Zr_{0.5}O_2$); CZ15/85-HS ($Ce_{0.15}Zr_{0.85}O_2$). Figures reproduced from [69].

As previously mentioned, catalysis of superoxide radicals depends on electron exchange in the reaction. The electron exchange relies on the conduction of electrons in the catalysis. Therefore, the reaction rates in catalysis of superoxide radicals depend on the mobile electronic carriers that are available in the scavenging. Doping zirconium into CeO_2 not only promotes the oxygen vacancy concentration structurally, but also promotes the Ce^{3+} contents and so to increase the electron holes. In other words, doping zirconium into CeO_2 improves superoxide scavenging activity due to the increased extrinsic cationic defects and nonstoichiometric oxygen vacancies. The promoted mobile electronic carriers increase the reducibility of $Ce_xZr_{1-x}O_2$ catalysts [68,69]. This perspective is able to explain why more zirconium dopants in nanoparticles always improve their activity, and the results do not correspond to oxygen vacancy

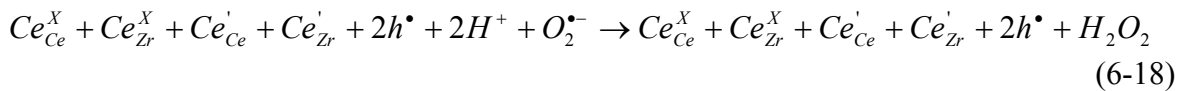
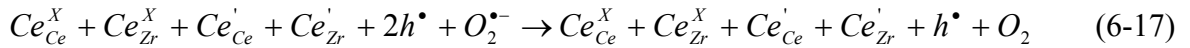
concentration in $Ce_xZr_{1-x}O_2$ nanoparticles. The “active sites” in superoxide radical scavenging, i.e. mobile electronic carriers including oxygen vacancy, electron holes, are listed in the following equation. Equation 6-13 shows that oxygen vacancies are mobile electronic carriers, which are contributed from nonstoichiometric defects. Equation 6-14 shows that electron holes are mobile electronic carriers, electron holes, which are contributed from extrinsic defects.



Here, the model to describe superoxide radical scavenging which mediated by oxygen vacancies in $Ce_xZr_{1-x}O_2$ nanoparticles is listed in the following equations.



The model to describe superoxide radical scavenging which mediated by electron holes in $Ce_xZr_{1-x}O_2$ nanoparticles is listed in the following equation.



In the equation described above, we understand that zirconium dopants in $Ce_xZr_{1-x}O_2$ nanoparticles improve scavenging activities both against hydrogen peroxide and superoxide radicals. The improvements are dependent on the increased oxygen vacancy concentration in the case of hydrogen peroxide, and the improvements in the case of superoxide radicals are dependent on the promoted mobile electronic carriers. The reason to make this difference is due to the characteristics of hydrogen peroxide and superoxide radicals. Moreover, most accumulative oxidative stress occurred in biological systems relies on the transition of electrons

between radicals and molecules, so the optimum free radical scavengers in biological systems are those that have shown greater activities to remove excess electrons from free radicals. In conclusion, we can hypothesize that $Ce_{0.4}Zr_{0.6}O_2$ nanoparticles would be the most effective free radical scavengers in biological systems.

6.4 Electron Conduction in Catalysis

In this section, the capability for $Ce_xZr_{1-x}O_2$ nanoparticles to conduct electrons in catalysis will be inspected and discussed, since the particular property is essential for free radical scavenging. In previous section, the inhibition percentages of dye formation merely indicated nanoparticles' superoxide radical scavenging activities. The capability for $Ce_xZr_{1-x}O_2$ nanoparticles to conduct electrons in catalysis, therefore, would need solid evidence other than the information we acquired. Here, we adopt a classic assay on biochemistry basis to inspect the electron conduction on $Ce_xZr_{1-x}O_2$ nanoparticles. The assay includes a bivalent, reversible conducting molecule, which is colorimetric only in its reduced state. Thus, the rise or decline of optical density of this molecule would indicate its redox states. Replace WST-1 salts in the methodology for scavenging activity test, the redox states of this molecule would indicate the capability for catalysts to conduct electrons in catalysis. The principle of this method is shown in Figure 6-17. The colorimetric molecule that used to test electron conduction on $Ce_xZr_{1-x}O_2$ nanoparticles is cytochrome c (II/III).

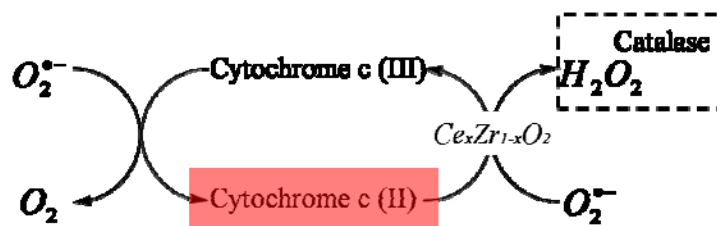


Figure 6-17. Principle of the biochemistry based assay to inspect the capability for $Ce_xZr_{1-x}O_2$ nanoparticles to conduct electrons in catalysis.

6.4.1 Experimental Methods

To generate superoxide radicals, we used hypoxanthine and enzyme xanthine oxidase to produce the final products including superoxide radicals, hydrogen peroxide, and uric acids. The hydrogen peroxide produced in such reaction is then removed by adding large amounts of catalase, in order to prevent the affects of hydrogen peroxide.

To detect the electron conducted on $Ce_xZr_{1-x}O_2$ nanoparticles, a reversible dye, cytochrome c is conducted in the experiment. Reduced by superoxide radicals, cytochrome c forms cytochrome c (II), and is colorimetric at 550 nm. In this study, the redox state of cytochrome c is observed using UV-Vis (UV/Vis - Perkin-Elmer Lambda 800).

For the samples prepared for UV-Vis, a stock solution including 0.5 mM EDTA, 12.5 μ M cytochrome c (Aldrich), in addition of 3,000 unit/ml catalase (Aldrich) is prepared as reagent solution. 0.5 mM hypoxanthine, 0.9 U/ml xanthine oxidase, and 1 mM $Ce_xZr_{1-x}O_2$ nanoparticle suspensions ($x = 0, 0.4, 0.6, 0.7, 0.8, 1.0$) were prepared in 100 mM phosphate buffer (pH = 7.4, Aldrich) as stock solutions. Before initiating the reaction, 780 μ l of reagent solution, 80 μ l of sample solution (i.e. 1 mM $Ce_xZr_{1-x}O_2$ nanoparticle suspensions or 1.875 U/ml SOD samples), and 20 μ l of xanthine oxidase stock solution were titrated into a 1 ml cuvette. To initiate the reaction, 100 μ l of hypoxanthine stock solution was titrated into the cuvette in order to generate superoxide radicals. The total concentrations of $Ce_xZr_{1-x}O_2$ nanoparticle suspensions were then diluted to 200 μ M after all. The dye formation was finally detected by UV-Vis at 550 nm. The stock solutions used in this experiment and the experimental procedures are illustrated in Figure 6-18. The absorbance was recorded and shown in Figure 6-19.

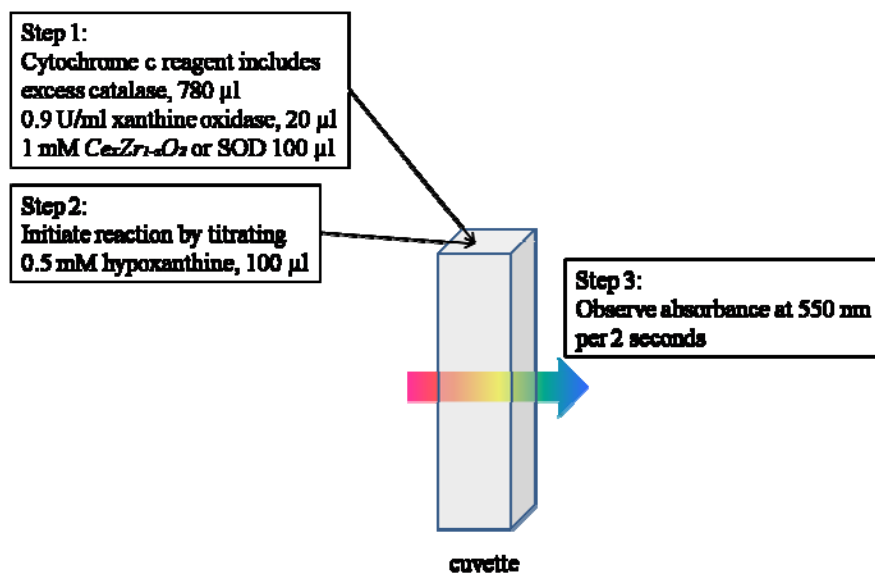


Figure 6-18. Experimental arrangements of stock solution concentrations and experimental procedures to inspect electron conduction on $Ce_xZr_{1-x}O_2$ nanoparticles.

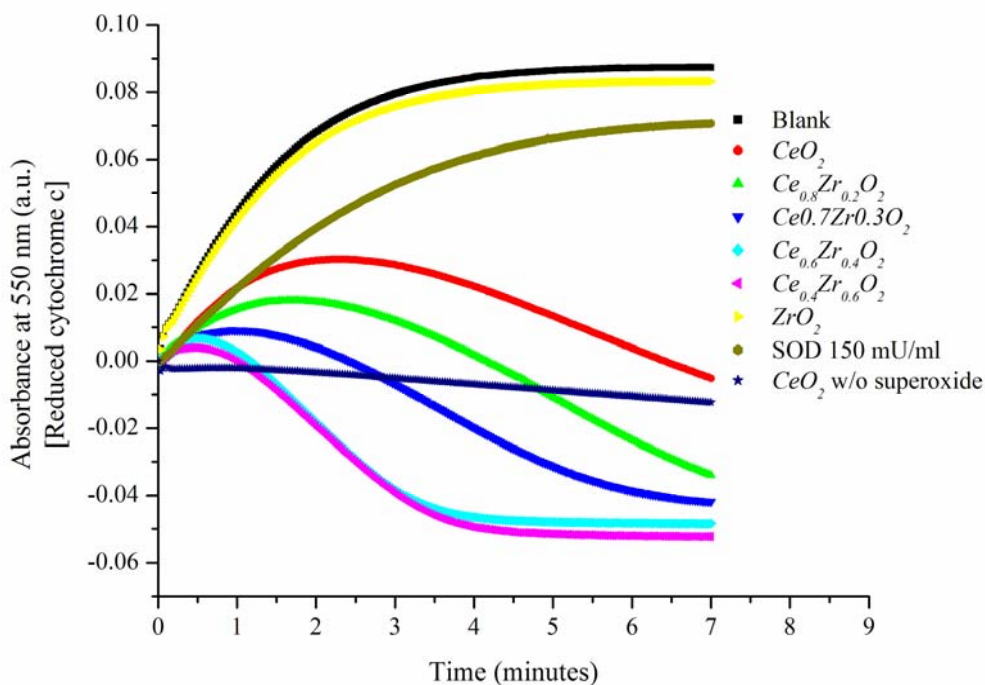


Figure 6-19. Redox states of cytochrome c detected using UV-Vis. The higher the absorbance represents more reduced cytochrome c in the reaction. The declined absorbance suggests that $Ce_xZr_{1-x}O_2$ nanoparticles received electrons from the reduced cytochrome c in catalysis.

6.4.2 Results and Discussion

In Figure 6-19, the vertical axis shows the redox states of cytochrome c. The higher absorbance in the particular diagram represents more reduced cytochrome c (II) in the reaction. In the samples with enzyme SOD protection, the concentration of reduced cytochrome c increases and stays at high level. It is because SOD merely catalyzes superoxide radicals to hydrogen peroxide, and the products hydrogen peroxide was immediately removed by enzyme CAT. On the other hand, the samples with $Ce_xZr_{1-x}O_2$ nanoparticles' protection not only inhibit the formation of reduced cytochrome c, but also reverse the redox state to its initial state. In these samples enzyme CAT was also involved, so the agents to reverse redox states of cytochrome c (from II to III) do not appear to be hydrogen peroxide. It is because the catalysis from superoxide to hydrogen peroxide requires electrons, so $Ce_xZr_{1-x}O_2$ nanoparticles take electrons from the reduced cytochrome c and react with other superoxide radicals to form hydrogen peroxide. The reversed absorbance observed in UV-Vis therefore indicates the capability for $Ce_xZr_{1-x}O_2$ nanoparticles to conduct electrons in catalysis. In Figure 6-19, more zirconium dopants in $Ce_xZr_{1-x}O_2$ solid solutions result in more rapid reversion in redox states. It is the evidence that $Ce_xZr_{1-x}O_2$ nanoparticles with more zirconium dopants exhibit greater capability to precede electron conduction. The results obtained in this experiment correspond to the conclusion in previous section, and these $Ce_xZr_{1-x}O_2$ nanoparticles really are catalyzing free radicals through electron exchange.

6.5 Summary

In this chapter, the free radical scavenging activities of a series of $Ce_xZr_{1-x}O_2$ nanoparticles were discussed. Using biochemistry assays, the residual concentration of hydrogen peroxide at physiological levels was measured over time. In the presence of $Ce_xZr_{1-x}O_2$ nanoparticles, hydrogen peroxide concentrations in each sample decreased over time. Among all the samples,

$Ce_{0.7}Zr_{0.3}O_2$ nanoparticles have the greatest peroxide scavenging activity. In addition, the scavenging activities of $Ce_xZr_{1-x}O_2$ nanoparticles are correlated with the oxygen vacancy concentrations in the materials. It is because the catalysis of hydrogen peroxide is determined by the transition of oxygen ions, so the oxygen vacancy concentrations in $Ce_xZr_{1-x}O_2$ nanoparticles become dominant in the scavenging processes.

Using the methodologies based on biochemistry reactions, superoxide radicals were generated. The scavenging activities of $Ce_xZr_{1-x}O_2$ nanoparticles to superoxide radicals were tested using an irreversible dye, and their activities were compared with the fastest superoxide radical scavenger, superoxide dismutase. The results showed that these $Ce_xZr_{1-x}O_2$ nanoparticles have even greater scavenging activity than enzyme SOD. Furthermore, the results showed that the scavenging activity of $Ce_xZr_{1-x}O_2$ nanoparticles increases with increasing zirconium dopants in $Ce_xZr_{1-x}O_2$ nanoparticles. It is because the zirconium dopants prompt Ce^{3+} contents in $Ce_xZr_{1-x}O_2$ nanoparticles, and resulting in more mobile electronic carriers. These mobile electronic carriers conduct the unpaired electrons in free radicals, so the scavenging activities to superoxide radicals are through electron exchange. It is because the catalysis of superoxide radicals is determined by the exchange of electrons, so the concentration of mobile electronic carriers in $Ce_xZr_{1-x}O_2$ nanoparticles becomes dominant in the reaction. The mobile electronic carriers include oxygen vacancies, cationic defects that are caused by nonstoichiometric defects and extrinsic defects.

The capability for $Ce_xZr_{1-x}O_2$ nanoparticles to conduct electrons in catalysis is inspected using a bivalent, reversible conducting molecule. In the experiment, electrons in the reduced cytochrome c were taken away, resulting in non-colorimetric cytochrome c (III). Thus, the reversed absorbance represents electron conduction from cytochrome c, through $Ce_xZr_{1-x}O_2$

nanoparticles, and finally to form hydrogen peroxide. The electron conduction in $Ce_xZr_{1-x}O_2$ nanoparticles relies on the mobile electronic carriers in $Ce_xZr_{1-x}O_2$ nanoparticles; therefore the materials with most carriers also have the greatest activity to scavenge free radicals. Since the accumulation of oxidative damage relies on electron exchange between molecules, such as proteins, lipids, DNA, and RNA, the optimum free radical scavenger therefore relies on mobile electronic carrier concentration in $Ce_xZr_{1-x}O_2$ nanoparticles. Thus, we conclude that $Ce_{0.4}Zr_{0.6}O_2$ nanoparticles would be the most effective free radical scavengers in biological systems, based on the results in the activity tests.

After this chapter, the remarkable results confirm that the development of $Ce_xZr_{1-x}O_2$ nanoparticles for biomedical applications requires the knowledge in materials science. Incorporated with zirconium dopants, nanoparticles that have up to nine times of free radical scavenging activity compared to undoped CeO_2 nanoparticles were developed. After the knowledge learned in this chapter, we have successfully built up a model that describes hydrogen peroxide scavenging and superoxide radical scavenging. According to the model, the scavenging activities of these nanocatalysts can be further promoted if more mobile electronic carriers are increased.

CHAPTER 7 IMPLICATIONS

7.1 Distinct Antioxidant Defense Pathway

CeO₂ nanoparticles have been found to inhibit the progression of organism dysfunction through regulating its endogenous oxidative stress. It was hypothesized that *CeO₂* nanoparticles scavenge free radicals and therefore improve cell cultures' viability. However, we found that *CeO₂* nanoparticles are eligible to reinstate the redox states of cytochrome c in the presence of superoxide radicals. It suggests that protection provided by *CeO₂* nanoparticles may be contributed by reactivating cytochrome c's redox states as well. The results also explain the finding in the previous study that *CeO₂* nanoparticles restored retinal photoreceptor cells' function even if *CeO₂* nanoparticles were administered after cell cultures were damaged [54].

Cytochrome c is a heme protein found loosely bounded with inner membrane of mitochondria. It is an antioxidant protein with two valences, which can oxidize superoxide radicals and reduce hydrogen peroxide. Cytochrome c is also a very important protein in metabolism. It conducts electrons in electron transport chain of mitochondria. Lacking of cytochrome c, the electrons leak out of the transport chain and forming free radicals in the sequence. In addition, the over reduced cytochrome c would lose its bonding with inner membrane of mitochondria and finally be released to cytoplasm. When cytochrome c is released from mitochondria, they tend to bond with other proteins, forming apoptosome. The apoptosome triggers apoptosis later on. It has been demonstrated that cytochrome c release requires a two-step process [91]. Cytochrome c is present as loosely and tightly bound pools attached to the inner mitochondrial membrane by its association with free radicals, and this interaction must first be disrupted to generate a soluble pool of this protein. Specifically, solubilization of cytochrome c involves a breaching of the electrostatic or hydrophobic affiliations that this protein usually

maintains in mitochondrial membrane. Once cytochrome c is solubilized, the reduced cytochrome c loses its electrostatic bonding with mitochondrial membrane. The lowered electrostatic bonding is sufficient to trigger cytochrome c's release. Since superoxide radicals have long been found to reduce cytochrome c, the concept of scavenge superoxide radicals prior their damage to cytochrome c, or preventing cytochrome c released from mitochondria has been classified in a novel antioxidant defense pathway (shown in Figure 2-1).

CeO_2 nanoparticles were found to exhibit exceptional scavenging activity to superoxide radicals and peroxides. The reaction rate constants of CeO_2 nanoparticles are superior to enzyme superoxide dismutase [29] and close to catalase [92]. However, the half life of free radicals is short, the question remains on how the damaged cells were recovered if nanoceria merely scavenge free radicals in cell cultures? Beyond CeO_2 nanoparticles' free radical scavenging properties, we found that CeO_2 nanoparticles are eligible to regulate the redox states of cytochrome c, especially in the presence of superoxide radicals. Figure 7-1 shows the redox states of cytochrome c in the presence of superoxide radicals, CeO_2 nanoparticles, and SOD. The data are extracted from Figure 6-19. In Figure 7-1, profile A shows the reduction of cytochrome c in the presence of superoxide radicals. Profile B shows the restoration of cytochrome c as CeO_2 nanoparticles scavenge superoxide radicals. In profile C, CeO_2 nanoparticles slightly restore cytochrome c's redox states in the absence of superoxide radicals. In profile D, SOD only against superoxide's attack, but does not regulate cytochrome c's redox states. The redox states of cytochrome c are influential in apoptosis [40,93]. Overwhelmed by the reduced cytochrome c: (1) electrons would leak from mitochondrial electron transportation chain, forming detrimental ROS [94]; (2) cytochrome c would be released from mitochondria due to the lower electrostatic bonding in reduced cytochrome c [95]. The accumulation of ROS

as well as cytochrome c release trigger caspase proteins and finally induce apoptosis. By regulating the redox states of cytochrome c, CeO_2 nanoparticles may provide a distinct antioxidant defense pathway by inhibiting the release of cytochrome c from mitochondrial membrane.

In this chapter, we found that $Ce_xZr_{1-x}O_2$ nanoparticles are capable to regulate the redox states of cytochrome c (shown in Figure 6-19). In reference to Chen et al.'s work, exposing CeO_2 nanoparticles to cultures not only scavenges free radicals in cultures, but also regulates the redox states of cytochrome c and inhibits cytochrome c release. We suggest that $Ce_xZr_{1-x}O_2$ nanoparticles may contribute a distinct antioxidant defense beyond free radical scavenging. In consequence, the proposed mechanism is able to explain the previous discovery by Chen et al. that CeO_2 nanoparticles restored retinal photoreceptor cells' function even CeO_2 nanoparticles were administered after cells were damaged [58].

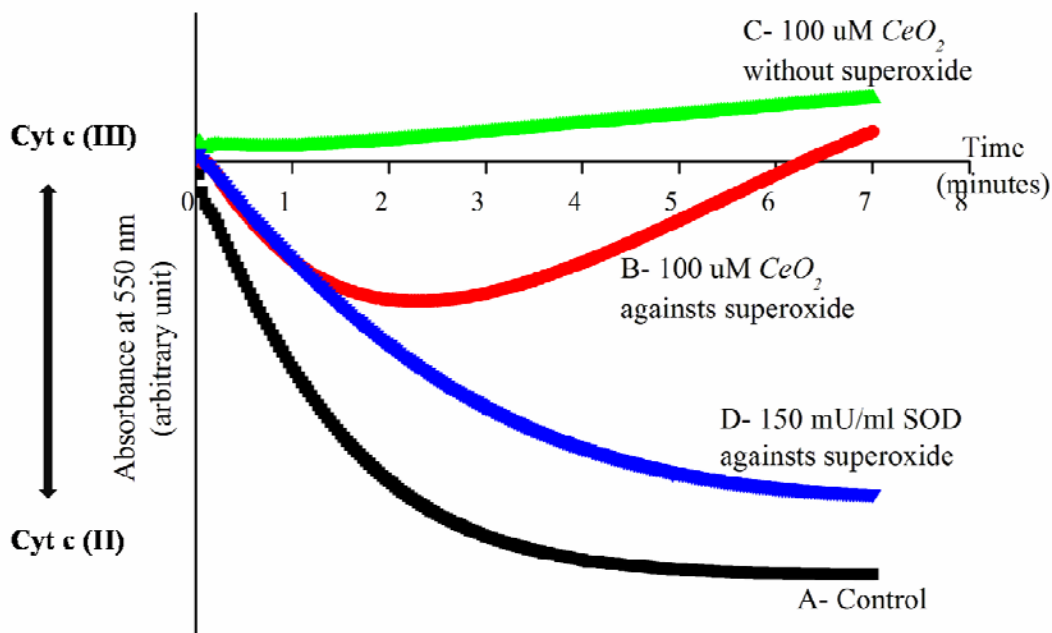


Figure 7-1. Redox states of cytochrome c in the presence or absence of superoxide radicals.

7.2 Implications in Catalysis

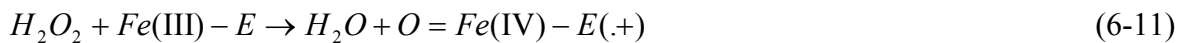
In heterogeneous catalysis, the electrochemical reactions comprise a series of electron exchange, oxygen ion exchange in/between ligands and catalysts. The selection of optimum catalysts relies on inspecting the catalyst's capability to conduct electrons or oxygen ions in catalysis. According to the results in previous experiments, the biochemistry based assays that have been developed in this work are ideal techniques to inspect the interfacial electrochemistry in the process of catalysts.

7.2.1 Alternative Technique to Inspect ionic Conductivity at Room Temperature

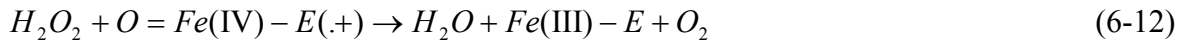
Due to the characteristics of hydrogen peroxide, it is found that the exchange of oxygen ions is involved in the catalysis for hydrogen peroxide. Based on this concept, hydrogen peroxide molecules can be treated as probes to inspect ionic conductivity of CeO_2 -based materials in catalysis.

In biochemistry, enzyme CAT is used to catalyze hydrogen peroxide. The catalysis of hydrogen peroxide. The catalysis proceeds in two steps [96] by

(1) Oxidation of CAT by a peroxide



(2) Oxidation of the substrates.



Overall,



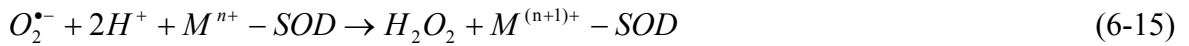
In the catalysis, the oxidized enzyme possesses two oxidative equivalents above the native enzyme and contains highly reactive oxygen bound to the iron. The iron is then promoted to its

quadrivalent states. In the catalysis proceeded by CAT, the catalysis of hydrogen peroxide depends on its characteristics that conducting its oxygen ions with enzyme CAT.

At low hydrogen peroxide concentration, we have demonstrated that the amount of mobile oxygen vacancies dominates the catalysis. As an excellent ionic conductor, $C_xZr_{1-x}O_2$ actually mediates ionic conduction by its mobile oxygen vacancies. It is, the scavenging rates to hydrogen peroxide scavenging not only indicate the oxygen vacancy concentration in catalyst's lattice, but also represent ionic conductivity of $Ce_xZr_{1-x}O_2$.

7.2.2 Alternative Technique to Inspect Localized Electron Conductivity

The catalysis of superoxide radicals are preceded by two steps. Superoxide radicals can donate electrons to a molecule and become oxygen molecule, or they can receive electrons from others to form peroxides. In biochemistry, enzyme SOD is used to catalyze superoxide radicals into hydrogen peroxide and oxygen in free radical scavenging. The catalysis carried out by enzyme SOD is as follow,



Overall,



In the catalysis carried out by enzymes, it is certainly that the exchange of electrons involved in the catalysis. However, the scavenging occurred in $Ce_xZr_{1-x}O_2$ nanoparticles remains uncertain, therefore this section is to discuss the mechanism based on the results obtained in superoxide radical scavenging tests.

The scavenging to superoxide radicals undergoes a different mechanism comparing to the scavenging to hydrogen peroxide. In the catalysis to superoxide radicals, a superoxide radical

either donates an electron to catalysts forming oxygen molecules, or receives an electron forming peroxide. In means that the amount of electrons conducted in catalysts dominates the reaction. Thus, superoxide radicals work as perfect probes to inspect localized mobile electronic carriers in catalysis. Utilizing a bivalent, reversible, colorimetric protein cytochrome c, it becomes possible to “see” the electron conduction in catalysis. The reversed optical density in the reaction represents the electrons taken away by catalysts, where the electrons are taken away to form peroxide with other superoxide radicals.

CHAPTER 8 CONCLUSIONS

The *in vitro* studies in Chapter 3 have shown that CeO_2 nanoparticles could relieve oxidative stress in certain cell cultures. The culture's viability was improved accordingly. In addition to these successful *in vitro* results, several objectives have been achieved in further, including synthesis and characterization of $Ce_xZr_{1-x}O_2$ nanoparticles, evaluation of free radical scavenging activities of these nanoparticles, and a distinct antioxidant defense pathway that may contribute to the protection to cultures. In this dissertation, several innovative techniques have been emerged to evaluate the catalytic properties of $Ce_xZr_{1-x}O_2$ nanoparticles, and the results are remarkable. The conclusions are summarized as follow:

- Reverse micelle method is used to synthesize $Ce_xZr_{1-x}O_2$ nanoparticles of 3-7 nm.
- The synthesized $Ce_xZr_{1-x}O_2$ nanoparticles are crystalline solid solutions, so heat treatments can be exempted in the synthesis.
- The synthesized $Ce_xZr_{1-x}O_2$ nanoparticles are dispersed in sodium citrate buffer. The agglomeration using such preparation can be ignored, since the agglomerate size distributions are smaller than 10 nm.
- CeO_2 nanoparticles can improve cell culture's viability by relieving its endogenous oxidative stress.
- Doping zirconium into CeO_2 nanoparticles promotes their free radical scavenging activities. The enhancement comes from the promoted oxygen vacancies as well as mobile electronic carriers in the lattice.
- For $Ce_xZr_{1-x}O_2$ nanoparticles to scavenge hydrogen peroxide at low concentration, oxygen ions are involved in the reactions, therefore oxygen vacancies in the lattice dominate the scavenging. Among all samples, $Ce_{0.7}Zr_{0.3}O_2$ nanoparticles exhibit the greatest activity. The scavenging activities of $Ce_xZr_{1-x}O_2$ nanoparticles correlate to the oxygen storage capacity reported in the same materials.
- For $Ce_xZr_{1-x}O_2$ nanoparticles to scavenge superoxide radicals, the scavenging activity depends on their capability to conduct electrons in catalysis. Zirconium dopants promote Ce^{3+} contents in CeO_2 lattice, so the mobile electronic carrier concentration increases due to the promoted cationic defects in the lattice. The cationic defects include oxygen vacancies and electron holes in the lattice, which are contributed from nonstoichiometric

defects and extrinsic defects. After activity tests, $Ce_{0.4}Zr_{0.6}O_2$ nanoparticles exhibit the greatest activity of all $Ce_xZr_{1-x}O_2$ nanoparticles.

- $Ce_xZr_{1-x}O_2$ nanoparticles can reactivate cytochrome c's redox states in the presence of superoxide radicals. The reinstatement of redox states may regulate cytochrome c's function in metabolism, and further achieve a distinct antioxidant defense.

APPENDIX A GLOSSARY

Apoptosis	A form of programmed cell death in multi-cellular organisms. It is one of the main types of programmed cell death (PCD) and involves a series of biochemical events leading to a characteristic cell morphology and death
<i>bcl-2</i>	Protein <i>bcl-2</i> is an antioxidant protein. An important one states that this is achieved by activation or inactivation of an inner mitochondrial permeability transition pore, which is involved in the regulation of matrix Ca^{2+} , pH, and voltage. It is also thought that some Bcl-2 family proteins can induce (pro-apoptotic members) or inhibit (anti-apoptotic members) the release of cytochrome c in to the cytosol which, once there, activates caspase-9 and caspase-3, leading to apoptosis.
β TC-tet cells	Pancreatic β TC lines derived from murine insulinomas.
CAT	Enzyme catalase. Catalase is a common enzyme found in nearly all living organisms. Its functions include catalyzing the decomposition of hydrogen peroxide to water and oxygen. Catalase has one of the highest turnover rates of all enzymes; one molecule of catalase can convert millions of molecules of hydrogen peroxide to water and oxygen per second.
Carotenoids	Carotene is a precursor to vitamin A, a pigment essential for good vision, and carotenoids can also act as antioxidants.
CeO_2 :	Cerium oxide, cerium dioxide, or sometimes listed as ceria.
$\text{Ce}_x\text{Zr}_{1-x}\text{O}_2$:	Zirconium-doped CeO_2 . The x in the chemical formula represents the stoichiometry of cerium ions, and $(1-x)$ represents the stoichiometry of zirconium ions sitting on the cationic sites in the cubic fluorite structures.
COX	The enzyme cytochrome c oxidase or Complex IV is a large transmembrane protein complex found in bacteria and the mitochondrion. It is the last enzyme in the respiratory electron transport chain of mitochondria (or bacteria) located in the mitochondrial (or bacterial) membrane. It receives an electron from each of four cytochrome c molecules, and transfers them to one oxygen molecule, converting molecular oxygen to two molecules of water.
Cytochrome c	Cytochrome c is a small heme protein found loosely associated with the inner membrane of the mitochondrion. It is a soluble protein, unlike other cytochromes, and is an essential component of the electron transfer chain, where it carries one electron. It is capable of undergoing oxidation and reduction, but does not bind oxygen. It transfers electrons between Complexes III and IV.

DCF 2',7'-dichlorofluorescein diacetate. A fluorescent dye to detect reactive oxygen species in biological systems.

Electron transport chain

An electron transport chain associates electron carriers and mediating biochemical reactions that produce adenosine triphosphate (ATP), which is a major energy intermediate in living organisms. Only two sources of energy are available to biosynthesize organic molecules and maintain biochemical and kinetic processes in living organisms: redox reactions. The schematic diagram of electron transportation chain is shown in Figure 2-1.

Endoplasmic reticulum stress

Endoplasmic reticulum (ER) stress is caused by the accumulation of unfolded proteins in the ER lumen, and is associated with vascular and neurodegenerative diseases.

Feret's diameter In microscopy, Feret's diameter is the measured distance between parallel lines that are tangent to an object's profile and perpendicular to the ocular scale. Generally, Feret's diameter is the greatest distance possible between any two points along the boundary of a region of interest.

GPx Enzyme glutathione peroxidase. Enzyme glutathione oxidase is an enzyme that catalyzes glutathione and oxygen to form glutathione disulfide and hydrogen peroxide.

GSH Glutathione is a tripeptide. It contains an unusual peptide linkage between the amine group of cysteine and the carboxyl group of the glutamate side chain. Glutathione, an antioxidant, protects cells from toxins such as free radicals.

HO Enzyme heme oxygenase. An enzyme that catalyzes the degradation of heme. This produces biliverdin, iron, and carbon monoxide.

HQ Hydroquinone. Hydroquinone is a compounds used to induce oxidative stress in this dissertation.

Inflammation Inflammation is the complex biological response of vascular tissues to harmful stimuli, such as pathogens, damaged cells, or irritants. It is a protective attempt by the organism to remove the injurious stimuli as well as initiate the healing process for the tissue.

Lipid peroxidation Lipid peroxidation refers to the oxidative degradation of lipids. It is the process whereby free radicals grab electrons from the lipids in cell membranes, resulting in cell damage. This process proceeds by a free radical chain reaction mechanism.

OSC	Oxygen storage capacity. The OSC is determined by measuring oxygen consumed by the catalyst after reduction under isothermal conditions. It is a quantitative basis the capability of metal oxide catalysts to release oxygen under reducing condition, and to uptake oxygen under oxidizing conditions.
Oxidative stress	Oxidative stress is caused by an imbalance between the production of reactive oxygen and a biological system's ability to readily detoxify the reactive intermediates or easily repair the resulting damage.
ROS	Reactive oxygen species. Reactive oxygen species are oxygen species that are generated from metabolism. They are reactive to other molecules, and usually cause damage to cells. In free radicals in biology superoxide radicals, hydroxyl radicals, and hydrogen peroxide are usually appointed as ROS.
Superoxide	Superoxide radicals. Superoxide is the anion O_2^- . It is important as the product of the one-electron reduction of dioxygen, which occurs widely in nature. With one unpaired electron, the superoxide ion is a free radical, and, like dioxygen, it is paramagnetic.
SOD	Enzyme superoxide dismutase. Enzyme SOD is an enzyme found in almost all living systems. It catalyzes the dismutation of superoxide into oxygen and hydrogen peroxide. As such, it is an important antioxidant defense in nearly all cells exposed to oxygen.
Type 1 diabetes	Also called juvenile diabetes. It is a form of diabetes mellitus. Type 1 diabetes is an autoimmune disease that results in the permanent destruction of insulin producing beta cells of the pancreas. Type 1 is lethal unless treatment with exogenous insulin via injections replaces the missing hormone.

LIST OF REFERENCES

- [1] B. Halliwell, and J. Gutteridge, "Free Radicals in Biology and Medicine", Oxford University Press, 4 edition, **2007**.
- [2] D. C. Wallace, "*Mitochondrial diseases in man and mouse*", *Science* **1999**, 283, 1482.
- [3] C. Y. Li, and R. M. Jackson, "*Reactive species mechanisms of cellular hypoxia-reoxygenation injury*", *American Journal of Physiology-Cell Physiology* **2002**, 282, C227.
- [4] A. Shukla, M. Gulumian, T. K. Hei, D. Kamp, Q. Rahman, and B. T. Mossman, "*Multiple roles of oxidants in the pathogenesis of asbestos-induced diseases*", *Free Radical Biology and Medicine* **2003**, 34, 1117.
- [5] W. R. Markesbery, "*Oxidative stress hypothesis in Alzheimer's disease*", *Free Radical Biology and Medicine* **1997**, 23, 134.
- [6] Y. Gilgun-Sherki, E. Melamed, and D. Offen, "*Oxidative stress induced-neurodegenerative diseases: the need for antioxidants that penetrate the blood brain barrier*", *Neuropharmacology* **2001**, 40, 959.
- [7] H. S. Kwak, H. S. Yim, P. B. Chock, and M. B. Yim, "*Endogenous Intracellular Glutathionyl Radicals Are Generated in Neuroblastoma-Cells under Hydrogen-Peroxide Oxidative Stress*", *Proceedings of the National Academy of Sciences of the United States of America* **1995**, 92, 4582.
- [8] M. Hangaishi, H. Nakajima, J. Taguchi, R. Igarashi, J. Hoshino, K. Kurokawa, S. Kimura, R. Nagai, and M. Ohno, "*Lecithinized Cu, Zn-superoxide dismutase limits the infarct size following ischemia-reperfusion injury in rat hearts in vivo*", *Biochemical and Biophysical Research Communications* **2001**, 285, 1220.
- [9] A. V. Kuznetsov, S. Schneeberger, R. Seiler, G. Brandacher, W. Mark, W. Steurer, V. Saks, Y. Usson, R. Margreiter, and E. Gnaiger, "*Mitochondrial defects and heterogeneous cytochrome c release after cardiac cold ischemia and reperfusion*", *American Journal of Physiology-Heart and Circulatory Physiology* **2004**, 286, H1633.
- [10] K. N. Baden, J. Murray, R. A. Capaldi, and K. Guillemin, "*Early developmental pathology due to cytochrome c oxidase deficiency is revealed by a new zebrafish model*", *Journal of Biological Chemistry* **2007**, 282, 34839.
- [11] Y. Cai, G. A. Martens, S. A. Hinke, H. Heimberg, D. Pipeleers, and M. Van de Castele, "*Increased oxygen radical formation and mitochondrial dysfunction mediate beta cell apoptosis under conditions of AMP-activated protein kinase stimulation*", *Free Radical Biology and Medicine* **2007**, 42, 64.
- [12] A. Laurent, C. Nicco, C. Chereau, C. Goulvestre, J. Alexandre, A. Alves, E. Levy, F. Goldwasser, Y. Panis, O. Soubrane, B. Weill, and F. Batteux, "*Controlling tumor growth*

- by modulating endogenous production of reactive oxygen species", *Cancer Research* **2005**, 65, 948.
- [13] Y. Gilgun-Sherki, E. Melamed, and D. Offen, "Oxidative stress induced-neurodegenerative diseases: the need for antioxidants that penetrate the blood brain barrier", *Neuropharmacology* **2001**, 40, 959.
- [14] J. S. Beckman, T. W. Beckman, J. Chen, P. A. Marshall, and B. A. Freeman, "Apparent Hydroxyl Radical Production by Peroxynitrite - Implications for Endothelial Injury from Nitric-Oxide and Superoxide", *Proceedings of the National Academy of Sciences of the United States of America* **1990**, 87, 1620.
- [15] C. C. Yeh, M. F. Hou, S. M. Tsai, S. K. Lin, J. K. Hsiao, J. C. Huang, L. H. Wang, S. H. Wu, L. A. Hou, H. Ma, and L. Y. Tsai, "Superoxide anion radical, lipid peroxides and antioxidant status in the blood of patients with breast cancer", *Clinica Chimica Acta* **2005**, 361, 104.
- [16] S. Dimon-Gadal, P. Gerbaud, G. Keryer, W. Anderson, D. Evain-Brion, and F. Raynaud, "In vitro effects of oxygen-derived free radicals on type I and type II cAMP-dependent protein kinases", *Journal of Biological Chemistry* **1998**, 273, 22833.
- [17] K. S. Zhao, G. M. Zhao, D. L. Wu, Y. Soong, A. V. Birk, P. W. Schiller, and H. H. Szeto, "Cell-permeable peptide antioxidants targeted to inner mitochondrial membrane inhibit mitochondrial swelling, oxidative cell death, and reperfusion injury", *Journal of Biological Chemistry* **2004**, 279, 34682.
- [18] B. J. Day, "Catalytic antioxidants: a radical approach to new therapeutics", *Drug Discovery Today* **2004**, 9, 557.
- [19] M. Salinas, R. Diaz, N. G. Abraham, C. M. R. de Galarreta, and A. Cuadrado, "Nerve growth factor protects against 6-hydroxydopamine-induced oxidative stress by increasing expression of heme oxygenase-1 in a phosphatidylinositol 3-kinase-dependent manner", *Journal of Biological Chemistry* **2003**, 278, 13898.
- [20] P. Storz, "Reactive oxygen species in tumor progression", *Frontiers in Bioscience* **2005**, 10, 1881.
- [21] J. M. Mates, C. Perez-Gomez, and I. N. De Castro, "Antioxidant enzymes and human diseases", *Clinical Biochemistry* **1999**, 32, 595.
- [22] S. Melov, S. R. Doctrow, J. A. Schneider, J. Haberson, M. Patel, P. E. Coskun, K. Huffman, D. C. Wallace, and B. Malfroy, "Lifespan extension and rescue of spongiform encephalopathy in superoxide dismutase 2 nullizygous mice treated with superoxide dismutase-catalase mimetics", *Journal of Neuroscience* **2001**, 21, 8348.
- [23] W. C. Orr, and R. S. Sohal, "Extension of Life-Span by Overexpression of Superoxide-Dismutase and Catalase in *Drosophila-Melanogaster*", *Science* **1994**, 263, 1128.

- [24] S. E. Schriener, N. J. Linford, G. M. Martin, P. Treuting, C. E. Ogburn, M. Emond, P. E. Coskun, W. Ladiges, N. Wolf, H. Van Remmen, D. C. Wallace, and P. S. Rabinovitch, "*Extension of murine life span by overexpression of catalase targeted to mitochondria*", *Science* **2005**, 308, 1909.
- [25] B. A. Rzigalinski, "*Nanoparticles and cell longevity*", *Technology in Cancer Research & Treatment* **2005**, 4, 651.
- [26] B. A. Rzigalinski, K. Meehan, R. M. Davis, Y. Xu, W. C. Miles, and C. A. Cohen, "*Radical nanomedicine*", *Nanomedicine* **2006**, 1, 399.
- [27] Y. Y. Tsai, J. Oca-Cossio, K. Agering, N. E. Simpson, M. A. Atkinson, C. H. Wasserfall, I. Constantinidis, and W. Sigmund, "*Novel synthesis of cerium oxide nanoparticles for free radical scavenging*", *Nanomedicine* **2007**, 2, 325.
- [28] S. Babu, A. Velez, K. Wozniak, J. Szydlowska, and S. Seal, "*Electron paramagnetic study on radical scavenging properties of ceria nanoparticles*", *Chemical Physics Letters* **2007**, 442, 405.
- [29] C. Korsvik, S. Patil, S. Seal, and W. T. Self, "*Superoxide dismutase mimetic properties exhibited by vacancy engineered ceria nanoparticles*", *Chemical Communications* **2007**, 1056.
- [30] Official website of American Diabetes Association, <http://www.diabetes.org/>
- [31] A. M. Davali, L. Scaglia, D. H. Zanger, J. Hollister, S. Bonner-Weir, and G. C. Weir, "*Vulnerability of Islet in the Immediate Posttransplantation Period: Dynamic Changes in Structure and Function*", *Diabetes* **1996**, 45, 1161.
- [32] S. Paraskevas, D. Maysinger, R. Wang, T. P. Duguid, and L. Rosenberg, "*Cell Loss in Isolated Human Islets Occurs by Apoptosis*", *Pancreas* **2000**, 20, 270.
- [33] L. Rosenburg, R. Wang, S. Paraskevas, and D. Maysinger, "*Structural and Functional Changes Resulting from Islet Isolation Lead to Islet Cell Death*", *Surgery* **1999**, 126, 393.
- [34] J. Couzin, "*Islet Transplants Face Test of Time*", *Science* **2004**, 306, 34.
- [35] C. Ricordi, P. E. Lacy, and D. W. Scharp, "*Automated Islet Isolation From Human Pancreas*", *Diabetes* **1989**, 38, 140.
- [36] A. Troverelli, "*Catalysis by Ceria and Related Materials*"; *Catalytic Science Series 2*; World Scientific Publishing Company: London, UK, **2002**.
- [37] D. C. Wu, P. Teismann, K. Tieu, M. Vila, V. Jackson-Lewis, H. Ischiropoulos, and S. Przedborski, "*NADPH oxidase mediates oxidative stress in the 1-methyl-4-phenyl-1,2,3,6-tetrahydropyridine model of Parkinson's disease*", *Proceedings of the National Academy of Sciences of the United States of America* **2003**, 100, 6145.

- [38] W. Droge, "Free radicals in the physiological control of cell function", *Physiological Reviews* **2002**, 82, 47.
- [39] N. J. Linford, S. E. Schriener, and P. S. Rabinovitch, "Oxidative damage and aging: Spotlight on mitochondria", *Cancer Research* **2006**, 66, 2497.
- [40] E. Bossy-Wetzell, D. D. Newmeyer, and D. R. Green, "Mitochondrial cytochrome c release in apoptosis occurs upstream of DEVD-specific caspase activation and independently of mitochondrial transmembrane depolarization", *Embo Journal* **1998**, 17, 37.
- [41] J. Garland, and C. Rudin, "Cytochrome c induces apoptosis in intact cells and is dominant to growth signalling, apoptosis suppression and malignant change." *Blood* **1997**, 90, 2648.
- [42] M. B. Hampton, B. Zhivotovsky, A. F. G. Slater, D. H. Burgess, and S. Orrenius, "Importance of the redox state of cytochrome c during caspase activation in cytosolic extracts", *Biochemical Journal* **1998**, 329, 95.
- [43] J. T. Hancock, R. Desikan, and S. J. Neill, "Does the redox status of cytochrome C act as a fail-safe mechanism in the regulation of programmed cell death?" *Free Radical Biology and Medicine* **2001**, 31, 697.
- [44] R. Bottino, A. N. Balamurugan, S. Bertera, M. Pietropaolo, M. Trucco, and J. D. Piganelli, "Preservation of human islet cell functional mass by anti-oxidative action of a novel SOD mimic compound", *Diabetes* **2002**, 51, 2561.
- [45] A. Pileggi, R. D. Molano, T. Berney, P. Cattani, C. Vizzardelli, R. Oliver, C. Fraker, C. Ricordi, R. L. Pastori, F. H. Bach, and L. Inverardi, "Heme oxygenase-1 induction in islet cells results in protection from apoptosis and improved in vivo function after transplantation", *Diabetes* **2001**, 50, 1983.
- [46] G. Hughes, M. P. Murphy, and E. C. Ledgerwood, "Mitochondrial reactive oxygen species regulate the temporal activation of nuclear factor kappa B to modulate tumour necrosis factor-induced apoptosis: evidence from mitochondria-targeted antioxidants", *Biochemical Journal* **2005**, 389, 83.
- [47] B. Errede, G. P. Haight, and M. D. Kamen, "Oxidation of Ferrocyanide-C by Mitochondrial Cytochrome-C Oxidase", *Proceedings of the National Academy of Sciences of the United States of America* **1976**, 73, 113.
- [48] T. Masui, K. Fujiwara, Y. M. Peng, T. Sakata, K. Machida, H. Mori, and G. Adachi, "Characterization and catalytic properties of CeO₂-ZrO₂ ultrafine particles prepared by the microemulsion method", *Journal of Alloys and Compounds* **1998**, 269, 116.
- [49] S. Bernal, G. Blanco, J. M. Pintado, J. M. Rodriguez-Izquierdo, and M. P. Yeste, "An alternative way of reporting on the redox behaviour of ceria-based catalytic materials:

Temperature-chemical environment-oxidation state diagrams", Catalysis Communications **2005**, 6, 582.

- [50] Y. M. Chiang, E. B. Lavik, I. Kosacki, H. L. Tuller, and J. Y. Ying, "Nonstoichiometry and electrical conductivity of nanocrystalline CeO_{2-x} ", *Journal of Electroceramics* **1997**, 1, 7.
- [51] C. T. Campbell, and C. H. F. Peden, "Chemistry - Oxygen vacancies and catalysis on ceria surfaces", *Science* **2005**, 309, 713.
- [52] E. Finocchio, M. Daturi, C. Binet, J. C. Lavalley, and G. Blanchard, "Thermal evolution of the adsorbed methoxy species on $CexZr1-xO_2$ solid solution samples: a FT-IR study", *Catalysis Today* **1999**, 52, 53.
- [53] S. Bernal, G. Blanco, J. M. Pintado, J. M. Rodriguez-Izquierdo, and M. P. Yeste, "An alternative way of reporting on the redox behaviour of ceria-based catalytic materials: Temperature-chemical environment-oxidation state diagrams", *Catalysis Communications* **2005**, 6, 582.
- [54] M. Das, S. Patil, N. Bhargava, J. F. Kang, L. M. Riedel, S. Seal, and J. J. Hickman, "Auto-catalytic ceria nanoparticles offer neuroprotection to adult rat spinal cord neurons", *Biomaterials* **2007**, 28, 1918.
- [55] D. Schubert, R. Dargusch, J. Raitano, and S. W. Chan, "Cerium and yttrium oxide nanoparticles are neuroprotective", *Biochemical and Biophysical Research Communications* **2006**, 342, 86.
- [56] R. W. Tarnuzzer, J. Colon, S. Patil, and S. Seal, "Vacancy engineered ceria nanostructures for protection from radiation-induced cellular damage", *Nano Letters* **2005**, 5, 2573.
- [57] J. L. Niu, A. Azfer, L. M. Rogers, X. H. Wang, and P. E. Kolattukudy, "Cardioprotective effects of cerium oxide nanoparticles in a transgenic murine model of cardiomyopathy", *Cardiovascular Research* **2007**, 73, 549.
- [58] J. P. Chen, S. Patil, S. Seal, and J. F. McGinnis, "Rare earth nanoparticles prevent retinal degeneration induced by intracellular peroxides", *Nature Nanotechnology* **2006**, 1, 142.
- [59] R. M. Ormerod, "Solid oxide fuel cells", *Chemical Society Reviews* **2003**, 32, 17.
- [60] D. Duprez, C. Descorme, T. Birchem, and E. Rohart, "Oxygen storage and mobility on model three-way catalysts", *Topics in Catalysis* **2001**, 16, 49.
- [61] P. Jasinski, T. Suzuki, and H. U. Anderson, "Nanocrystalline undoped ceria oxygen sensor", *Sensors and Actuators B-Chemical* **2003**, 95, 73.

- [62] C. Descorme, Y. Madier, and D. Duprez, "Infrared study of oxygen adsorption and activation on cerium-zirconium mixed oxides", *Journal of Catalysis* **2000**, 196, 167.
- [63] F. Esch, S. Fabris, L. Zhou, T. Montini, C. Africh, P. Fornasiero, G. Comelli, and R. Rosei, "Electron localization determines defect formation on ceria substrates", *Science* **2005**, 309, 752.
- [64] C. Binet, M. Daturi, and J. C. Lavalley, "IR study of polycrystalline ceria properties in oxidised and reduced states", *Catalysis Today* **1999**, 50, 207.
- [65] Y. Namai, K. I. Fukui, and Y. Iwasawa, "Atom-resolved noncontact atomic force microscopic and scanning tunneling microscopic observations of the structure and dynamic behavior of CeO₂(111) surfaces", *Catalysis Today* **2003**, 85, 79.
- [66] M. J. Li, Z. H. Feng, G. Xiong, P. L. Ying, Q. Xin, and C. Li, "Phase transformation in the surface region of zirconia detected by UV Raman spectroscopy", *Journal of Physical Chemistry B* **2001**, 105, 8107.
- [67] S. H. Overbury, D. R. Mullins, D. R. Huntley, and L. Kundakovic, "Chemisorption and reaction of NO and N₂O on oxidized and reduced ceria surfaces studied by soft X-ray photoemission spectroscopy and desorption spectroscopy", *Journal of Catalysis* **1999**, 186, 296.
- [68] H. Vidal, J. Kaspar, M. Pijolat, G. Colon, S. Bernal, A. Cordon, V. Perrichon, and F. Fally, "Redox behavior of CeO₂-ZrO₂ mixed oxides I. Influence of redox treatments on high surface area catalysts", *Applied Catalysis B-Environmental* **2000**, 27, 49.
- [69] H. Vidal, J. Kaspar, M. Pijolat, G. Colon, S. Bernal, A. Cordon, V. Perrichon, and F. Fally, "Redox behavior of CeO₂-ZrO₂ mixed oxides - II. Influence of redox treatments on low surface area catalysts", *Applied Catalysis B-Environmental* **2001**, 30, 75.
- [70] W. J. Stark, M. Maciejewski, L. Madler, S. E. Pratsinis, and A. Baiker, "Flame-made nanocrystalline ceria/zirconia: structural properties and dynamic oxygen exchange capacity", *Journal of Catalysis* **2003**, 220, 35.
- [71] E. Mamontov, T. Egami, R. Brezny, M. Koranne, and S. Tyagi, "Lattice defects and oxygen storage capacity of nanocrystalline ceria and ceria-zirconia", *Journal of Physical Chemistry B* **2000**, 104, 11110.
- [72] J. Kaspar, P. Fornasiero, and M. Graziani, "Use of CeO₂-based oxides in the three-way catalysis", *Catalysis Today* **1999**, 50, 285.
- [73] M. Yashima, K. Ohtake, H. Arashi, M. Kakihana, and M. Yoshimura, "Determination of Cubic-Tetragonal Phase-Boundary in Zr_{1-x}Y_xO_{2-x/2} Solid-Solutions by Raman-Spectroscopy", *Journal of Applied Physics* **1993**, 74, 7603.

- [74] M. Yashima, H. Arashi, M. Kakihana, and M. Yoshimura, "Raman-Scattering Study of Cubic-Tetragonal Phase-Transition in $Zr_{1-x}Ce_xO_2$ Solid-Solution", *Journal of the American Ceramic Society* **1994**, 77, 1067.
- [75] F. Zhang, C. H. Chen, J. C. Hanson, R. D. Robinson, I. P. Herman, and S. W. Chan, "Phases in ceria-zirconia binary oxide $(1-x)CeO_2-xZrO_2$ nanoparticles: The effect of particle size", *Journal of the American Ceramic Society* **2006**, 89, 1028.
- [76] W. Lin, Y. W. Huang, X. D. Zhao, and Y. Ma, "Toxicity of Cerium Oxide Nanoparticles in Human Lung Cancer Cells", *International Journal of Toxicology* **2006**, 25, 451.
- [77] M. D. Hernandez-Alonso, A. B. Hungria, A. Martinez-Arias, M. Fernandez-Garcia, J. M. Coronado, J. C. Conesa, and J. Soria, "EPR Study of the Photoassisted Formation of Radicals on CeO_2 Nanoparticles Employed for Toluene Photooxidation", *Applied Catalysis B-Environmental* **2004**, 50, 167.
- [78] F. Zhang, Q. Jin, and S. W. Chan, "Ceria nanoparticles: Size, size distribution, and shape", *Journal of Applied Physics* **2004**, 95, 4319.
- [79] A. M. Davali, L. Scaglia, D. H. Zanger, J. Hollister, S. Bonner-Weir, and G. C. Weir, "Vulnerability of Islet in the Immediate Posttransplantation Period: Dynamic Changes in Structure and Function", *Diabetes* **1996**, 45, 1161.
- [80] C. Karagiozov, and D. Montchilova, "Synthesis of nano-sized particles from metal carbonates by the method of reversed micelles", *Chemical Engineering and Processing* **2005**, 44, 115.
- [81] Y. Huang, T. Ma, J. L. Yang, L. M. Zhang, J. T. He, and H. F. Li, "Preparation of spherical ultrafine zirconia powder in microemulsion system and its dispersibility", *Ceramics International* **2004**, 30, 675.
- [82] Z. H. Wu, R. E. Benfield, L. Guo, H. J. Li, Q. L. Yang, D. Grandjean, Q. S. Li, and H. S. Zhu, "Cerium oxide nanoparticles coated by surfactant sodium bis(2-ethylhexyl) sulphosuccinate (AOT): local atomic structures and X-ray absorption spectroscopic studies", *Journal of Physics-Condensed Matter* **2001**, 13, 5269.
- [83] D. Kim, M. Miyamoto, and M. Nakayama, "Photoluminescence properties of CdS and CdMnS quantum dots prepared by a reverse-micelle method", *Journal of electron microscopy* **2005**, 54, 131.
- [84] A. Dasgupta, D. Das, and P. K. Das, "Reactivity of trypsin in reverse micelles: neglected role of aggregate size compared to water-pool components", *Biochimie* **2005**, 87, 12, 1111.
- [85] P. Majumder, R. Sarkar, A. Shaw, "Ultrafast dynamics in a nanocage of enzymes: Solvation and fluorescence resonance energy transfer in reverse micelles", *Journal of Colloid and Interface Science* **2005**, 290, 462.

- [86] Y. Yin, and A. P. Alivisatos, "*Colloidal nanocrystal synthesis and the organic-inorganic interface*", *Nature* **2005**, 437, 664.
- [87] J. P. Hsu, and A. Nacu, "*An experimental study on the rheological properties of aqueous ceria dispersions*", *Journal of Colloid and Interface Science* **2004**, 274, 277.
- [88] S. Biggs, P. J. Scales, Y. K. Leong, and T. W. Healy, "*Effects of Citrate Adsorption on the Interactions between Zirconia Surfaces*", *Journal of the Chemical Society-Faraday Transactions* **1995**, 91, 2921.
- [89] A. V. Peskin, and C. C. Winterbourn, "*A microtiter plate assay for superoxide dismutase using a water-soluble tetrazolium salt (WST-1)*", *Clinica Chimica Acta* **2000**, 293, 157.
- [90] Technical manual "*SOD Assay Kit-WST*", Dojindo website:
<http://www.dojindo.com/newimages/SODKitTechnicalInformation.pdf>
- [91] M. Ott, J. D. Robertson, V. Gogvadze, B. Zhivotovsky, and S. Orrenius, "*Cytochrome c release from mitochondria proceeds by a two-step process*", *Proceedings of the National Academy of Sciences of the United States of America* **2002**, 99, 1259.
- [92] Y. Y. Tsai, J. Oca-Cossio, S. M. Lin, K. Woan, P. C. Yu, W. Sigmund, "*Enhanced Free Radical Scavenging Efficiency in Zirconium doped CeO₂ Nanoparticles*", *Nanomedicine*, under review.
- [93] R. A. Kirkland, and J. L. Franklin, "*Evidence for redox regulation of cytochrome c release during programmed neuronal death: Antioxidant effects of protein synthesis and caspase inhibition*", *Journal of Neuroscience* **2001**, 21, 1949.
- [94] J. D. Cortese, A. L. Voglino, and C. R. Hackenbrock, "*Persistence of Cytochrome-C Binding to Membranes at Physiological Mitochondrial Intermembrane Space Ionic-Strength*", *Biochimica Et Biophysica Acta-Bioenergetics* **1995**, 1228, 216.
- [95] A. V. Kuznetsov, S. Schneeberger, R. Seiler, G. Brandacher, W. Mark, W. Steurer, V. Saks, Y. Usson, R. Margreiter, and E. Gnaiger, "*Mitochondrial defects and heterogeneous cytochrome c release after cardiac cold ischemia and reperfusion*", *American Journal of Physiology-Heart and Circulatory Physiology* **2004**, 286, H1633.
- [96] T. J. Reid, 3rd, M. R. Murthy, A. Sicignano, N. Tanaka, W. D. Musick, and M. G. Rossmann, "*Structure and heme environment of beef liver catalase at 2.5 Å resolution*", *Proc Natl Acad Sci U S A* **1981**, 78, 4767.

BIOGRAPHICAL SKETCH

Yi-Yang Tsai was born in Taiwan in 1976. Before pursuing postgraduate education, he received B.S. in aeronautical engineering from Feng-Chia University, Taiwan in 1998. After two years of military services and two years of working experience as R&D engineer, he went overseas and accepted the graduate education in the United States. He first joined the Materials Engineering Department at University of Dayton in 2002, and received his M.S. in 2004. He joined the Materials Science and Engineering Department at University of Florida in 2004 under supervisory of Dr. Wolfgang M. Sigmund, and received his Ph.D. degree in summer 2008.

In the graduate training at University of Dayton, Yi-Yang was specialized in the characterization techniques, atomic force microscope and an ultrasound integrated atomic force microscope in the University of Dayton Research Institute (UDRI). Due to his excellent works, he was awarded a visiting research fellowship in 2003, and has allowed him to travel to the Fraunhofer Institute for Non-Destructive Testing (IZFP) in Germany for a short term research. In 2004, he was awarded the DAGSI research fellowship (Dayton Area Graduate Student Institute). His master thesis was a study that using ultrasound integrated atomic force microscope to detect nanoscale precipitations and cracks in aluminum alloys. In the two years, he has published two scientific papers and gave two invited presentations in SPIE conference.

In the Ph.D. training in Dr. Sigmund's research group, Yi-Yang has developed many innovative techniques in the interdisciplinary research project "Administering CeO_2 nanoparticles to enhance cell's viability" assigned by his advisor. In the project Yi-Yang and his advisor have made several remarkable breakthroughs. They have published several scientific articles and international patents based on the results. Other than the articles that have been published, he is preparing manuscripts for paper publications from the remarkable results.